# ATMOSPHERIC PARTICLES AND THEIR EFFECTS ON CLIMATE AND HEALTH

A Dissertation

by

JESSICA AILEEN MIRRIELEES

Submitted to the Office of Graduate and Professional Studies of
Texas A&M University
in partial fulfillment of the requirements for the degree of

DOCTOR OF PHILOSOPHY

| | |
|---|---|
| Chair of Committee, | Sarah D. Brooks |
| Co-Chair of Committee, | Daniel C.O. Thornton |
| Committee Members, | Gunnar Schade |
| | Renyi Zhang |
| Head of Department, | Ramalingam Saravanan |

December 2020

Major Subject: Atmospheric Sciences

# ABSTRACT

Aerosol particles have important effects on our world. In the context of the biosphere, aerosols contribute to air pollution and also influence human health. The ongoing COVID-19 pandemic has drawn attention to viral transmission routes, and in turn the dynamics of aerosol particles and the usefulness of filter materials for providing protection against the inhalation of aerosol particles. In order to provide information concerning the efficacy of various materials for the construction of masks for respiratory protection, our lab carried out a study on the penetration of aerosol particles through seventeen materials, which showed that some household or commercially-available materials (an allergen filter and an industrial composite filter) and combinations thereof are better choices than others for the preparation of homemade face masks.

Aerosols also influence weather via aerosol-cloud interactions, and climate via the direct and indirect aerosols effects. One process through which these particles affect weather and climate is through the nucleation process within clouds, which is required for cloud formation. Nucleation can proceed via droplets at warmer temperatures, or ice crystals at colder temperatures. The latter type of nucleation may proceed through several mechanisms which are not well understood and difficult to model. In order to bridge this gap, a series of ice nucleation workshops have taken place over the last few decades. The most recent ice nucleation workshop, the third phase of the Fifth International Ice Nucleation Workshop (FIN-03), brought several groups of researchers together for three weeks at Storm Peak Laboratory in Steamboat Springs, Colorado in

September 2015. The purpose of this workshop was to facilitate the intercomparison of ice nucleation instruments in a field campaign setting.

The effect of aerosol particles phase on ice nucleation is another facet of aerosol science which merits further work. Some studies have shown that glassy or viscous particles may effectively act as ice-nucleating particles, while others show that glassy particles may inhibit ice nucleation. We began a study on the effect of aerosol particle phase on ice nucleation efficiency, which is as yet incomplete. Particle phase was studied via measurements of viscosity and the temperature at which each sample transitioned from the liquid phase to a glassy phase. Ice nucleation measurements will be carried out in the future.

# ACKNOWLEDGEMENTS

I would like to thank my committee chair, Dr. Sarah D. Brooks, my co-chair, Dr. Daniel C.O. Thornton, and my committee members, Dr. Gunnar Schade and Dr. Renyi Zhang, for their time and support throughout the course of this research. I would like to give an additional thank-you to Dr. Brooks for giving me a chance as a high school teacher who e-mailed her out of the blue one day to ask if I could be a student in her lab.

Thanks also go to my labmates, Brianna Hendrickson, Alyssa Alsante, and Bo Chen. These last few weeks of experimental design, data collection, and group discussion have reflected what I wanted from graduate school. Keep thinking, and trying, and remember: we need more data.

A big thank you to Sophie Mayne, for being you (which is to say, the best). And thank you to my mother and stepfather, for supporting me during this big change in my life. And one last thank-you to my mother for talking about climate science and knowing more about it than I do.

CONTRIBUTORS AND FUNDING SOURCES

## Contributors

This work was supervised by a thesis (or) dissertation committee consisting of Dr. Sarah Brooks from the Department of Atmospheric Sciences (advisor), Dr. Daniel C.O. Thornton from the Department of Oceanography (co-advisor), Dr. Gunnar Schade from the Department of Atmospheric Sciences, and Dr. Renyi Zhang with appointments in the Department of Atmospheric Sciences and the Department of Chemistry.

Individual research contributions to the work on this dissertation will be summarized here. Bo Chen (Texas A&M University) assisted with data collection and manuscript revision for the mask materials project. Dr. Sarah Brooks lead the experimental design, assisted with data collection, and lead the manuscript revision process on this project as well. Dr. Michael R. Moreno (Texas A&M University) assisted with experimental design and the manuscript revision process for this project.

Jessica A. Mirrielees and Sarah D. Brooks wrote the FIN-03 manuscript with assistance from all teams and authors contributing information on instrument descriptions and comments on all results and conclusions, with contributions from Jake Zenker on data analysis. Paul J. DeMott, Ezra J.T. Levin, Thea Schiebel, and Kaitlyn Suski (at Colorado State University) provided data and analyses from the CSU-CFDC and CSU-IS instruments. Daniel J. Cziczo, Martin J. Wolfe, Sarvesh Garimella, and Maria Zawadowicz (at the Massachusetts Institute of Technology) provided MIT-SPIN team measurements and analyses. Markus D. Petters (North Carolina State University) provided description of the shared sampling protocol. Sarah S. Petters (now at the

University of North Carolina) provided weather observations and wind rose plots. Markus D. Petters and Sarah S. Petters also provided data and analysis for the NCSU-CS instrument. Heinz G. Bingemer, Jann Schrod, and Daniel Weber (Goethe University Frankfurt) provided data and analyses for the FRIDGE instrument. Anne Perring (Colgate University) provided data and analyses for the WIBS. Karl Froyd (NOAA) provided data and analyses for the LAS and PALMS. Anna Gannet Hallar and Ian McCubbin coordinated with visiting teams at Storm Peak Laboratory.

Dr. Charles Kolb (Aerodyne) facilitated glass transition temperature measurements, and direct mentorship was provided by Dr. Yue Zhang (previously at Aerodyne, recently hired by Texas A&M University). Maria Zamarron (Texas A&M University) assisted with viscometer measurements for this project.

**Funding Sources**

We would like to acknowledge Texas A&M University Geosciences Dean's Disciplinary/Interdisciplinary Initiative for funding the mask materials project.

Partial financial support for FIN-03 was provided by the U.S. National Science Foundation, Grant No. AGS-1339264 and DOE.

My work on the viscosity and glass transition temperature study was supported by a fellowship from the Hagler Institute for Advanced Study at Texas A&M University and a Lechner Scholarship.

TABLE OF CONTENTS

Page

LIST OF FIGURES

Page

LIST OF TABLES

Page

# CHAPTER I

# INTRODUCTION

## Alternative materials used to construct do-it-yourself masks

The COVID-19 pandemic has shown that much of the world, including the United States, is ill-prepared for the material demands of a global pandemic. Over 2.5 million cases of COVID-19 were confirmed in the United States at the end of June 2020, and over 125,000 of these infected individuals have died. COVID-19 is caused by a novel coronavirus, SARS-CoV-2.

In order to limit the spread of this disease, the World Health Organization (WHO) and the United States Center for Disease Control (CDC) have recommended the usage of face masks when in public (National Center for Immunization and Respiratory Diseases, 2020), primarily to avoid spreading the disease when infected and shedding the virus. Unfortunately, the average citizen is hard-pressed to find adequate masks, or to decide which materials will be the most effective in protecting them from the virus. Conflicting statements about the efficacy of cloth face coverings from various organizations and levels of government have led to confusion among the general public about the benefits of wearing these alternative protective items and the relative performance of various materials available for mask construction. Personal Protective Equipment (PPE), such as certified N95 respirators, were not available in quantities necessary for healthcare workers, much less the general public. In response to this

shortage, we have conducted filtration efficiency and pressure-drop testing of a wide range of common materials for constructing do-it-yourself masks.

## Ice nucleation

### Ice nucleation fundamentals

The term *ice nucleation* is used to describe the first development of a bulk ice phase larger than a critical size (G. Vali, DeMott, Mohler, & Whale, 2015). Ice nucleation may occur through several different mechanisms depending on the presence, or lack, of ice nucleating particles (INP). Temperatures below -38 °C are required for ice crystals to form in the absence of INP in a process called *homogeneous ice nucleation* (Pruppacher & Klett, 2010). Additionally, *heterogeneous ice nucleation* may take place at temperatures above -38 °C if INP are present.

Heterogeneous ice nucleation mechanisms are subdivided according to the temperature, relative humidity, and configuration of the system leading to initiation of the bulk ice phase. A brief description of these mechanisms follows. *Immersion ice nucleation* (also called *immersion freezing*) occurs when the freezing of a liquid droplet is initiated by an INP immersion within the droplet, which requires that water vapor is supersaturated with respect to liquid water (RH > 100%). In contrast, *deposition ice nucleation* occurs when water vapor deposits directly onto the surface of an INP as ice. This process requires supersaturation with respect to ice ($RH_{ice}$ > 100%), though supersaturation with respect to liquid water is not necessary (and increases the probability of competing ice nucleation mechanisms). *Condensation freezing* is defined

as an ice nucleation mechanism in which supercooled water vapor condenses onto the surface of an INP, then freezes. This mechanism can be difficult to distinguish from immersion and deposition ice nucleation. The last and final mode of heterogeneous ice nucleation, *contact freezing*, occurs when the contact between an INP and the surface of a liquid droplet initiates the freezing of the droplet (Kanji et al., 2017; G. Vali et al., 2015).

INP are relatively rare in the atmosphere, with typical concentrations (hereon denoted $N_{INP}$) between 0.1 to 100 $L^{-1}$ (DeMott et al., 2010; Murray, O'Sullivan, Atkinson, & Webb, 2012). Despite their low concentrations, INP participate in the formation, and influence the physical and optical properties, of cold and mixed-phase clouds. An increase in INP concentration can result in cloud glaciation, which in turn increases precipitation and decreases cloud lifetime (Lohmann & Feichter, 2005).

## Ice nucleation instruments

It is clear that INP play an important role in weather and climate. What is not yet clear is how to parameterize ice nucleation for use in atmospheric models, including the relevance of each ice nucleation mechanism in predicting cloud formation and properties. Accurate measurements of INP are therefore needed to provide input for these models. Additionally, these measurements will inform the place of each ice nucleation mechanism within atmospheric models.

No single "ground truth" INP measurement instrument, need to compare instruments, particularly in different modes, to determine differences in operation and

ideally to figure out how to make the best instrument possible, or to make sure that any instrument used to measure INP can be optimized so as not to undercount particles by failing to activate them (ex. RH too low, not enough time to activate), or overcount particles (ex. by shattering of large ice crystals, or running at too high RH when trying to measure in a low-RH mode like deposition).

## Aerosol phase and ice nucleation

Secondary organic aerosol (SOA) particles exist in the atmosphere in liquid, semi-solid, and glassy/amorphous solid states (Koop, Bookhold, Shiraiwa, & Pöschl, 2011; Saukko, Kuuluvainen, & Virtanen, 2012; Virtanen et al., 2010). Glassy aerosols are common throughout the troposphere, especially above 850 hPa (Shiraiwa et al., 2017). While both inorganic and organic compounds are capable of transition from the liquid phase to a glassy phase, the temperature at which this transition occurs (called the glass transition temperature) is generally too low for inorganic compounds to be of atmospheric importance, while the glass transition temperature of many organic compounds may be reached within the troposphere (Zobrist, Marcolli, Pedernera, & Koop, 2008).

It has been demonstrated that glassy aerosols can participate in the initiation of heterogeneous ice nucleation (Murray et al., 2010). A study on the INP efficiency suggested that amorphous SOA should be included in cloud and climate models alongside more conventional aerosol types, such as mineral dust, due to their ability to initiate ice nucleation (B. Wang et al., 2012). The efficiency of aerosol particles to

initiate ice nucleation has been shown to vary for each ice nucleation path (homogeneous vs. heterogeneous, immersion vs. deposition) depending on the composition phase state of the aerosol particle (Berkemeier, Shiraiwa, Poschl, & Koop, 2014).

An experiment carried out using the Aerosol Interactions and Dynamics in the Atmosphere (AIDA) chamber at the Karlsruhe Institute of Technology found that organic glass-forming aerosols with varying compositions were able to initiate heterogeneous ice nucleation at temperatures well below the glass transition temperature of each compound, provided that the ambient relative humidity was kept low enough to inhibit the uptake of water and subsequent conversion to the liquid state (Wagner et al., 2012).

# CHAPTER II

# WHAT TO WEAR: THE FILTRATION PERFORMANCE OF ALTERNATIVE MATERIALS USED TO CONSTRUCT DO-IT-YOURSELF MASKS

## Background

Face masks are effective in depositing exhaled droplets, known to carry viruses from the upper respiratory tract of an infectious individual (National Center for Immunization and Respiratory Diseases, 2020). They can also be used to protect against virus exposure through either larger droplets (which normally deposit on the ground and other surfaces shortly after they are produced) or smaller aerosol particles (which may remain airborne for minutes or hours) (Morawska, 2006). The diameter of SARS-CoV-2 has a mean value of approximately 100 nm and a range of 60 to 140 nm (Zhu et al., 2020). While respiratory infections may be transmitted through airborne particles, droplets, and direct contact, airborne particles with diameters below 5000 nm are considered the primary route for the transmission (Wells, 1955). While the relative significance of various routes of its transmission is unknown (Han, Lin, Ni, & You, 2020; J. Wang & Du, 2020), there is evidence that SARS-CoV-2 is transmitted via airborne particles with diameters <5000 nm (Allen & Marr, 2020). Common activities such as talking and breathing have been observed to generate aerosol particles and droplets which can be grouped into four modes by mean diameter (Morawska et al., 2009). The smallest of these modes (800±80 nm) accounted for 69-73% of particles generated by normal speech, 85-95% of particles generated by whispering, 86% of particles generated by breathing at a natural pace, and

84% of particles generated by coughing, while the second mode (1900±300 nm) accounted for 13-21%, 6-11%, 9%, and 14% of these categories, respectively. The third (3500±700 nm) and fourth (5500±100 nm) modes make up the remaining 0-18% of particles generated during each activity. Another study found that a significant fraction of particles generated by coughing have diameters in the 350-1000 nm range (Lindsley et al., 2010). Stadnytskyi et al. (2020) determined that the initial diameter range of droplets generated through loud speech was 12,000 to 21,000 nm, though these droplets quickly dehydrate in the air, resulting in an average dehydrated droplet diameter of approximately 4000 nm. Further, one minute of loud speech from an individual infected with SARS-CoV-2 may generate at least 1000 virus-containing aerosols or droplets, which remain airborne for over eight minutes (Stadnytskyi, Bax, Bax, & Anfinrud, 2020).

A study of two hospitals in Wuhan found that SARS-CoV-2 is present in both submicron (250-1000 nm) and supermicron (>1000 nm) aerosol (Liu et al., 2020). Submicron particles are capable of remaining airborne for some time due to their low settling velocities (J. Wang & Du, 2020). For example, an aerosol particle with a diameter of 100 nm will take over 83 hours to fall 1 m through the air in the absence of other forces, while a 300 nm droplet will require approximately half as much time, 43 hours, to fall the same distance (Wells, 1934). It has been observed that SARS-CoV-2 present in submicron aerosol particles can remain viable, and therefore infectious, for periods longer than three hours (van Doremalen et al., 2020). One study found that the virus remains infective even when aged in aerosol form for over twelve hours, and thus aerosol transmission may be an important pathway for transport of SARS-CoV-2 (Fears et al., 2020). An additional

complication to the problem of respiratory protection is the observation that viral RNA from SARS-CoV-2 may be shed through sputum after an infected individual's symptoms are alleviated. Post-symptomatic and asymptomatic individuals are therefore capable of producing submicron, airborne, virus-laden aerosol particles (Wölfel et al., 2020).

Classical filtration theory describes the manner in which the characteristics of filters, including fiber diameter, packing density, and filter thickness, as well as characteristics of the challenge aerosol such as particle diameter, shape, electrical charge, and the flow rate of the airstream passing through the filter influence filter efficiency (Stevens & Moyer, 1989). The particle diameter for which maximum penetration is observed for a filter material at a specific face velocity is known as the most penetrating particle size, or MPPS. Face velocity is defined as flow rate through a filter divided by the surface area of the filter material (Rengasamy, Eimer, & Shaffer, 2010).

According to classical filtration theory, particles with smaller diameters are more effectively collected through Brownian diffusion, and particles with larger diameters are more effectively collected through impaction and interception (Alderman, Parsons, Hogancamp, & Waggoner, 2008; Raynor, Leith, Lee, & Mukund, 2011). It follows that the estimated MPPS for airborne particles is approximately 100-300 nm (intermediate diameters) for passage through fibrous filters. However, as face velocity increases, the ability of aerosol particles to penetrate through the material increases (Eninger et al., 2008; Stevens & Moyer, 1989) and the MPPS decreases (Eninger et al., 2008; Huang et al., 2013). Face velocities that occur during inhalation and exhalation differ between individuals, and for the same individual during different activities (Anderson, Cassidy,

Janssen, & Dengel, 2006; Yuasa et al., 2015). Velocities consistent with breathing during moderate or strenuous activity may result in the decrease of MPPS to < 100 nm (Eninger et al., 2008).

It is also necessary to assess the "breathability" of the material used for face mask construction, determined by the measured drop in pressure across the filter material. A filter that adequately attenuates particle concentration for a face velocity relevant to inhalation and exhalation is of little use if it provides such a high resistance to flow that the wearer must effectively breathe around the mask, rather than through it. This resistance to flow is quantified through the measurement of the pressure drop across the mask material.

The performance of a filter material can be assessed through a metric, filter quality, which takes both percent penetration and pressure drop into account. Filter quality, $q_f$, is calculated as follows:

$$q_f = \frac{\ln\left(\frac{100}{C}\right)}{\Delta p} \tag{1}$$

where $C$ is the percent of particle concentration that penetrates the filter material and $\Delta p$ is the drop in pressure across the filter material (Brown, 1993). Comparisons of filter quality are considered more informative than comparisons of particle penetration alone since both concentration and pressure drop are taken into account. However, there are caveats in using filter quality to assess mask performance. Filter quality depends, in part, on pressure drop measurements which vary with face velocity. Face velocity will depend on dimensions of an individual mask, which can easily vary as much as 100%

from one mask design to the next. Even when the mask dimensions are known, true face velocity is likely to be highest near the mouth and nose, and lower elsewhere on the mask, and this is not taken into account in filter quality calculations. In addition, filter quality does not account for how well a mask fits on one's face, determining the leakage which can occur around the edges of a mask. The importance of mask fit cannot be overstated as this is the only way to ensure that air inhaled is passing through the filter material versus going around it. In workplaces where masks are required, improper fit is considered an occupational safety hazard. Therefore, the Occupational Safety and Health Administration (OSHA), which establishes requirements for employers to follow to ensure employee safety, has delineated specific testing protocols for employers to ensure employees are wearing masks with an appropriate fit (OSHA, 2004).

According to the U.S. National Institute of Occupational Safety and Health (NIOSH) standard procedure NIOSH 42 CFR 84.180, filter materials which block the penetration of at least 95% of the 300 nm diameter particles in an airstream are designated N95 materials. N95 respirators are considered the universal standard for PPE providing protection against particulate pollution. There is conflicting evidence on the ability of surgical masks to protect against inhalation of aerosol particles and droplets containing SARS-CoV-2. Some studies have found that surgical masks do not provide protection that is consistent with that of respiratory protection devices (Oberg & Brosseau, 2008; van der Sande, Teunis, & Sabel, 2008), while another study found that use of surgical face masks significantly reduced the detection of SARS-CoV-2 RNA in aerosol particles, and

somewhat reduced the detection of SARS-CoV-2 RNA in respiratory droplets (Leung et al., 2020).

A study on the efficacy of various materials in filtering the bacterium *Bacillus atrophaeus* (950-1250 nm diameter) and the virus bacteriophage MS2 (diameter 23 nm) found that surgical masks and vacuum cleaner bags allowed 4-6% penetration of the bacteria and 10-14% by the bacteriophage. The penetration observed for various cloth materials was 17-42% for the bacteria and 28-51% for the bacteriophage (Davies et al., 2013). These results agree with those in another study which showed that cloth masks made from tea towels provided roughly half the protection of surgical masks against the inhalation of particles with diameters 20-1000 nm (van der Sande et al., 2008).

A number of studies have investigated particle penetration through various cloth materials. One study found that masks made from cloth exhibited penetration levels between 40% and 90% when challenged with NaCl aerosol particles with diameters in the 20-1000 nm range, and thus only provided marginal protection against inhaled infectious agents at face velocities of 5.5 cm $s^{-1}$ and 16.5 cm $s^{-1}$ (Rengasamy et al., 2010). These face velocities are somewhat higher than those consistent with light physical activity and the NIOSH N95 respirator certification test, respectively (Rengasamy, Shaffer, Williams, & Smit, 2017). It should also be noted that little change in percent penetration was observed when the face velocity was increased from 5.5 cm $s^{-1}$ to 16.5 cm $s^{-1}$ in this study. A recently published evaluation of cloth face coverings made from household materials reported percent penetrations of ≥70% for various cotton, silk, nylon, and polyester fabrics using a face velocity typical of normal human breathing and aerosol particles with 75±20 nm

count median diameter (Zhao et al., 2020). Another study (Konda et al., 2020), which employed a face velocity of 9.89 cm $s^{-1}$, found that the percent penetration for particles with diameters 10-1000 nm was relatively high (40-95%) for one layer of 80 threads-per-inch cotton, but lower for one layer of 600 threads-per-inch cotton (5-35%), one layer of chiffon (10-45%), and four layers of natural silk (5-20%), and moderate for one layer of natural silk (30-60%) and rather variable for one layer of cotton-polyester flannel (10-75%).

The effect of adding additional layers to a single layer material has not been studied systematically. Konda et al. 2020 found that combinations of 600 threads-per-inch cotton with two layers of natural silk, two layers of chiffon, and one layer of cotton-polyester flannel decreased the percent penetration to 0-5%, 0-10%, and 0-20% respectively. However, the study reports that the N95 respirator allowed up to 30% of the particles to penetrate the filter. This result is in disagreement with the stated performance of N95 material according to the standard testing procedure for N95 certification (NIOSH, 2019). In contrast to the results from Konda et al. 2020, another study found that increasing the number of layers of cotton and gauze handkerchiefs from one to four had negligible effect on percent penetration (consistently > 96% for both materials), though this did increase the pressure drop through the material, which in turns decreases filter quality (Jung et al., 2014). This study also demonstrated that fabric face masks made from woven cotton fabric do not perform as well as surgical masks (with penetration of 77%±27% and 59%±37%, respectively). However, face masks made from nonwoven fabric outperformed surgical masks (penetration 45%±9%). To summarize the results of these studies, the best materials

for mask construction consisted of combinations of materials (four layers of silk, or cotton layered with other fabrics). The poorest choices were single layers of cotton, gauze, t-shirts, and scarves.

An additional consideration in mask performance is the fit of various mask designs to the face. A study that compared three cloth face masks to N95 respirators found that one mask characterized by a conical or tetrahedral shape that included an exhalation valve performed similarly (5-20% penetration) to an N95 respirator (5-15% penetration) in removing 30-2500 nm polystyrene latex aerosol particles. The two other cloth masks, which were rectangular in shape and did not include exhalation valves, did not perform as well (15-85% penetration for 30-2500 nm polystyrene latex aerosol particles) (Shakya, Noyes, Kallin, & Peltier, 2017).

Due to a shortage of suitable personal protective equipment during the pandemic, the CDC recommends making masks from cotton material, which most people will have at home in some form. A recent study has predicted that if as few as 50% of the population wears face masks when in public, and even if those face masks are only 50% effective, the rate at which SARS-CoV-2 spreads could be reduced by over 95% (Howard et al., 2020). Another study agrees that when 50% of the population wear masks, the spread is significantly reduced, and further reports that if 80% of the population wear masks, negligible transmission would occur (Yan, Guha, Hariharan, & Myers, 2019). Therefore, face masks that provide protection against inhalation of submicron aerosols and bare airborne viruses as well as supermicron droplets that may contain the virus are recommended. The goal of this study is to test a wide variety of commonly available

candidate materials in order to determine which filter materials provide adequate protection across a range of particle diameters at representative inhalation flow rates observed for various levels of physical activity.

## Methods

The filter efficiency of candidate materials for use in face masks and respirators was determined based on the percentage of particles sampled which passed through the material. Size-resolved measurements were conducted over the diameter range of 25-500 nm. While the size range of virus-laden aerosols is uncertain, emphasis has been placed on two particle diameters, 100 nm and 300 nm. The 300 nm particle diameter is significant because the standard NIOSH N95 certification specifically requires that 95% of the aerosol particles with a mass mean aerodynamic diameter of 300 nm in air be removed by a filter (NIOSH, 1995). However, 300 nm may not be the most penetrating particle size or the most important size to consider in the case of SARS-CoV-2. For comparison, 100 nm results are included since 100 nm is similar to the mean diameter of the SARS-CoV-2 virus (Zhu et al., 2020). In addition, pressure drop and filter quality are measured in this study. Finally, the biocompatibility of the chosen materials, though beyond the scope of our measurements, is discussed below.

An initial survey of the filtration efficiency of many common materials was conducted using the experimental set-up shown in Fig. 1. The selected materials included items widely available in the home, as well as common medical supplies. In addition, an industrial composite material (NxN Nano, Style NP097) which has been

used in industry and recently made available to the public for use during the coronavirus pandemic was included. This material was specifically engineered for masks. It is a three-layer composite material of polypropylene Spunbond, thermoplastic polyurethane nanofiber and polyethylene terephthalate Spunlace. Finally, for comparison, a N95 respirator (3M, Model 8200/07023) was used as a standard.

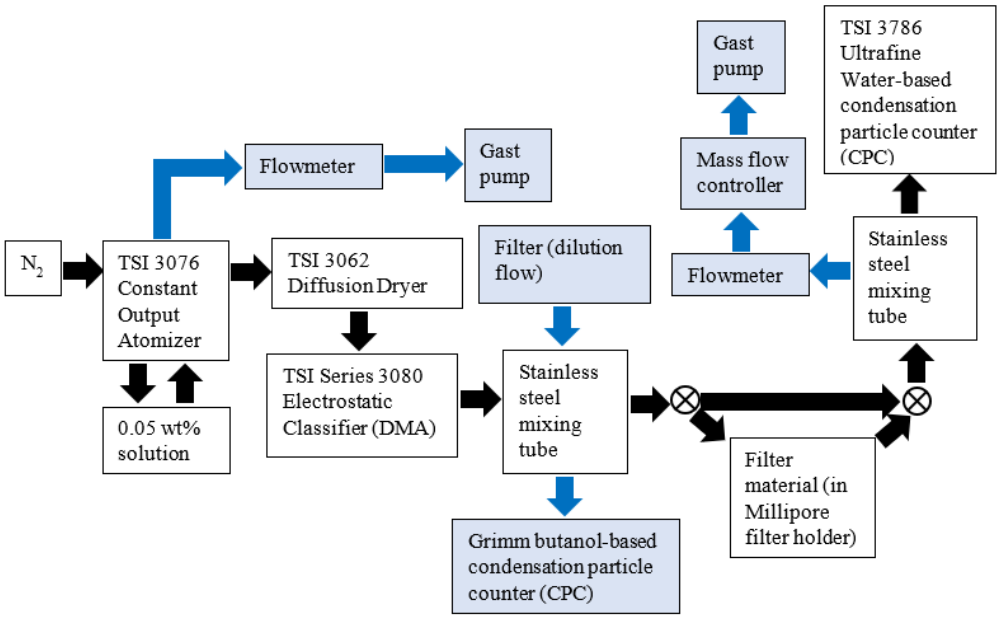


**Figure 1** Experimental setup for studying the effectiveness of filter materials to use for masks. The instrument setup used in the initial survey is color-coded white, while all instruments were used in the current study. The initial survey employed one condensation particle counter (TSI 3786), which was used to alternately measure the concentration of particles without and with the filter material in place. The remaining experiments employed two condensation particle counters in order to simultaneously measure the concentration of aerosol particles with and without the filter material in line.

To determine the percent penetration of particles through a potential mask material, a 5 cm diameter circle of the material was placed in a filter holder with a filtration area of 13.8 $cm^2$ (Millipore In-Line Filter Holder, Catalogue Number

XX4304700) and secured in place by an o-ring. Next, the filter holder was wrapped with parafilm in order to prevent leakage. In some cases, multiple layers of material were used (as reported in Table 1), to represent the way in which the given material would be worn or implemented in a DIY mask or respirator. For example, two layers of cotton bandana were tested, because a bandana is typically folded in half and tied at the back of an individual's head. The concentration of aerosol particles over a range of mean diameters (10, 25, 50, 100, 200, 300, 400, and 500 nm) was determined in the absence and presence of each filter sample material using the experimental setup shown in Fig. 1.

To test the percent penetration of aerosols of a specific mobility diameter through the filter material, aerosol samples were generated from a 0.05 wt% salt solution using an atomizer (TSI Model 3076 Constant Output Atomizer) supplied with gaseous $N_2$ (Eninger et al., 2008). In the initial survey ammonium sulfate, $(NH_4)_2SO_4$, was used due to availability. The subsequent measurements were conducted with sodium chloride, NaCl, to match the particle composition employed by NIOSH for certification tests for N95 respirators (NIOSH, 2019). It has been previously demonstrated that inert aerosols, such as these two salts, are appropriate analogues for viruses in the testing of filter materials when it is not possible or advisable to atomize viruses (Eninger et al., 2008). Additionally, data was collected for the N95 respirators using NaCl and $(NH_4)_2SO_4$ in order to compare penetration by each salt. It was found that the percent penetration of each through the N95 respirator agreed within 5% across the particle diameter range 25-500 nm. Therefore, the use of the two salts for atomizing solutions does not introduce uncertainties into the experimental results.

The aerosol sample flow leaving the atomizer was maintained at a flow rate of 1.0 ± 0.1 LPM by drawing off excess flow using a flowmeter (Omega, FL-2000 Series) and pump (Gast, Model DOA-V722-AA). The sample was directed through a diffusion dryer (TSI Model 3062 Diffusion Dryer) containing dried silica gel desiccant and to a differential mobility analyzer (DMA, TSI Series 3030 Electrostatic Classifier) to produce a near monodisperse flow of aerosol of the chosen mobility diameter. The mobility diameter was controlled by selecting the voltage on the DMA charge column to determine which size aerosol exited the DMA. Throughout the experiment, the DMA sample and sheath flow rates were maintained at constant flows of 1.0 ± 0.1 LPM and 5.0 LPM, respectively.

Next, the aerosol flow was sent through conductive tubing to a condensation particle counter (CPC, TSI Model 3786 Ultrafine Water-based Condensation Particle Counter) to determine the total concentration of aerosols in the selected size. Data was collected until the particle concentration was stable for several minutes. After the size-specific concentration was measured, flow leaving the DMA was redirected to pass through the sample holder containing the mask material of interest and to the CPC, to determine the concentration of aerosols passing through the filter. Once again, the CPC concentration was allowed to stabilize, and the concentration of aerosols penetrating the filter was determined. The condensation particle counter operated at a constant flow rate of 0.6 LPM, which was maintained throughout all experiments, resulting in a face velocity of 0.70 cm $s^{-1}$ through the filter material. The last sixty seconds of each data collection period were averaged in order to determine the mean particle concentration

with and without the filter sample material in place for each particle diameter. Then, the percent penetration $C$ was determined for each filter material, as shown in Eq. (2), where $N_{P1}^{filter}$ is the concentration of aerosol particles measured by the TSI water CPC with the filter material in place, and $N_{P1}^{no\ filter}$ is the concentration of aerosol particles measured by the TSI water CPC without the filter material in place.

$$C = \frac{N_{P1}^{filter}}{N_{P1}^{no\ filter}} \times 100\% \quad (2)$$

While the conditions in the initial survey were different from those used in the NIOSH 95 test, notably at a lower face velocity of 0.70 cm $s^{-1}$ compared to 9.3 cm $s^{-1}$, this low flow testing provided a rapid method for evaluating whether or not the mask materials removed 95% as a benchmark for identifying promising candidates for additional testing.

The results of the survey for 100 and 300 nm aerosol particles are summarized in Table 1. Except where noted in the table, all aerosol samples were generated from an ammonium sulfate solution. Two air filter materials (3M Filtrete 1900 and 3M Filtrete Premium Allergen and Ultrafine Particles) performed similarly to the N95 masks (Suzhou Sanical Protective and 3M Particulate respirator) with percent penetration ≤1% for both 100 and 300 nm aerosol particles. Additionally, the vacuum bag performed very well, with 1% penetration for 100 nm aerosol particles and 6% penetration for 300 nm aerosol particles.

**Table 1** Percent penetration of aerosol particles at face velocity = 0.70 cm $s^{-1}$.

| Filter Material | Manufacturer and Other Details | 100 nm Percent Penetration | 300 nm Percent Penetration |
|---|---|---|---|
| **3M particle respirator (N95)*** | 3M Model 8200/07023 | 0±0 | 0±0 |
| **Allergen filter*** | 3M Filtrete Premium Allergen and Ultrafine Particles, D Filter Size, True HEPA, Model #1150099, 1 layer | 0±0 | 0±0 |
| **Vacuum bag*** | Vacuum bag, Great Value "Eureka" style RR bag, 1 layer | 0±0 | 0±0 |
| **Surgical mask*** | Unigard FluidBloq surgical mask | 2±0 | 23±1 |
| **Bandana, 2 layers*** | Levi's Men's printed cotton bandana, red, 2 layers | 55±5 | 84±3 |
| **Heavy-duty tool wipe*** | Sellars ToolBox Z700, 1 layer | 29±1 | 53±5 |
| **Industrial composite filter*** | NxN Nano, Style NP097 (MERV16) | 0±0 | 4±2 |
| **Suzhou particle respirator (N95)** | Suzhou Sanical Protective N95 P/N: MS 8265 | <1 | <1 |
| **HVAC filter** | 3M Filtrete 1900, MERV 13, HVAC Filter, 4 layers | <1 | <1 |
| **Engine filter** | FRAM EXTRA GUARD, 2x Engine protection, CA 9895, 1 layer | 13 | 18 |
| **Bra cup** | Bra cup, Wire-free Ultra Soft Blissful Benefits by Warner's, Style RM1691W, color TW/white, 1 layer | 6 | 17 |
| **Weed barrier** | Sta-Green Ultimate WeedBarrier Level 3 Landscaping Fabric, 1 layer | 5 | 45 |
| **Shower curtain** | Shower curtain, water-repellant, embossed, 100% polyester, 1 layer | 8 | 45 |
| **Cotton pillowcase** | California Design Den, 100% Extra Long Staple Cotton, 600 thread count sateen weave pillowcase, 2 layers | 11 | 44 |
| **Microfiber pillowcase** | 1800 thread count ultra microfiber pillowcase, Estate Blue, 2 layers | 21 | 61 |
| **Coffee filter** | Walmart Great Value white coffee filter basket, 1 layer | 39 | 75 |
| **Surgical drape** | 1 layer | 2 | 36 |
| | 2 layers | 1 | 17 |

*Test aerosol was composed of NaCl

In contrast, surgical masks exhibited higher percent penetration (4% for 100 nm aerosol particles, 28% for 300 nm aerosol particles), and the percent penetration for coffee filters was even higher (39% for 100 nm aerosol particles, 75% for 300 nm aerosol particles). Out of the fabrics included in this survey, the weed barrier provided the best protection against 100 nm aerosol particles (5% penetration), followed by the bra cup (6% penetration), though neither of these materials provided adequate protection against 300 nm aerosol particles (45% and 17% penetration, respectively). The double-layered bandana, a common material for homemade or improvised face masks, allowed for the penetration of 28% of 100 nm aerosol particles and 72% of 300 nm aerosol particles. The microfiber pillowcase, with 1800 threads per inch, slightly outperformed the bandana (21% for 100 nm aerosol particles, 61% for 300 nm aerosol particles) but underperformed compared to the cotton pillowcase, with 600 threads per inch (11% for 100 nm aerosol particles, 44% for 300 nm aerosol particles).

At the initial low face velocity, eight of the seventeen samples failed to limit the percent penetration of 100 nm particles to 5% or less. When the particle diameter was increased to 300 nm, twelve of the eighteen samples failed.

Following the initial low face velocity survey, we made minor changes to our experimental setup to conduct measurements at higher (and therefore more relevant) face velocities. Changes are indicated in blue in Fig. 1. Higher flow rates were achieved by adding a dilution flow line using filtered room air upstream of the mixing chamber and a Gast pump controlled by a flow meter and mass flow controller downstream of the

sample material. Subsequent measurements were performed at face velocities of 0.70 cm $s^{-1}$, 4.30 cm $s^{-1}$, and 13.0 cm $s^{-1}$.

The middle and highest face velocities were chosen to correspond with average breathing flow rates during light physical work (30.3±6.2 L $min^{-1}$) and heavy physical work (72.3±22.9 L $min^{-1}$), respectively (Anderson et al., 2006). Mask surface areas observed in other studies range from 150 $cm^2$ to 250 $cm^2$ (Ramirez & O'Shaughnessy, 2017; Schilling et al., 2020). Simulated results show that the face velocity varies across the surface of filters such that only part of the surface area of the filter experiences a nonzero face velocity (Sachinidou, Bahk, & Wang, 2017). Therefore, the area of the face mask that the wearer breathes through was assumed to be 100 $cm^2$ for the purpose of conversion from breathing flow rate to test velocity. This area results in face velocities of 5.1±1.0 cm $s^{-1}$ for breathing during light physical work and 12.1±3.8 cm $s^{-1}$ for breathing during heavy physical work. Face mask filtration area will likely vary between individuals due to differences in facial geometry, just as breathing flow rates will vary due to differences in physiology such as gender (Janssen, Anderson, Cassidy, Weber, & Nelson, 2005). It should be noted that breathing face velocity may be higher or lower than estimated for various levels of physical work in this manuscript based on interpersonal differences and levels of activity.

The two CPCs used in this study do not report identical particle concentration when sampling from room air, polydisperse single-component aerosol, or monodisperse single-component aerosol, due to differences in internal working fluid (water and butanol) and other instrument parameters. Additionally, the two CPCs were placed at

different points in the experimental setup, which could lead to differences in the concentrations measured by the two instruments even if they were identical models. To account for any variations in the concentrations measured by the TSI water-based CPC and the GRIMM butanol CPC due to differences in instrument performance or particle losses through the respective sample lines, the instruments were cross-calibrated. Three blank runs in which the filter holder was in place, but empty, were performed for each face velocity. A correction factor $CF$ was determined according to Eq. (3).

$$CF = \frac{N_{P1,blank}}{N_{P2,blank}} \tag{3}$$

Where $N_{P1,blank}$ is the concentration of aerosol particles measured by the TSI water-based CPC during the blank runs, $N_{P2,blank}$ is the concentration of aerosol particles measured by the Grimm butanol CPC during the blank runs. The correction factors calculated for each face velocity were generally less than unity for aerosol particle diameters > 100 nm, and greater than unity for aerosol particle diameters < 100 nm at the highest face velocity. This may be due to the undercounting of small particles by the water-based CPC.

The correction factor $CF$ was subsequently used to determine the percent penetration for the sample runs:

$$C = \frac{N_{P1}}{CF\ N_{P2}} * 100\% \tag{4}$$

Where $N_{P1}$ is the concentration of aerosol particles measured by the TSI water-based CPC and $N_{P2}$ is the corresponding concentration of aerosol particles measured by the Grimm butanol-based CPC during sample runs.

The experiments conducted at the three face velocities utilized a smaller number of tested filter materials than the initial survey, including only those which performed relatively well in the initial survey, plus bandanas and surgical masks due to widespread usage (Table 2).

**Table 2** Percent penetration of aerosol particles at face velocity = 13.0 cm $s^{-1}$.

| Filter Material | Manufacturer and Other Details | 100 nm Percent Penetration | 300 nm Percent Penetration |
|---|---|---|---|
| **3M particle respirator (N95)** | 3M Model 8200/07023 | 1±1 | 3±3 |
| **Allergen filter** | 3M Filtrete Premium Allergen and Ultrafine Particles, D Filter Size, True HEPA, Model #1150099, 1 layer | 2±3 | 5±3 |
| **Vacuum bag** | Vacuum bag, Great Value "Eureka" style RR bag, 1 layer | 34±12 | 31±5 |
| **Surgical mask** | Unigard FluidBloq surgical mask | 55±3 | 39±1 |
| **Bandana, 2 layers** | Levi's Men's printed cotton bandana (red), 2 layers | 85±1 | 51±1 |
| **Heavy-duty tool wipe** | Sellars ToolBox Z700, 1 layer | 50±1 | 26±1 |
| **Industrial composite filter** | Chapter III NxN Nano, Style NP097 (MERV16) | 20±5 | 11±1 |

## Results and Discussion

The variation of percent penetration with face velocity is shown for 100 nm particles in Fig. 2(a) and 300 nm particles in Fig. 2(b). The percent penetration of 100 nm particles increased with face velocity for most of the materials, whereas the percentage of 300 nm particles penetrating the material decreased with face velocity or followed no trend, depending on the material. According to classic filtration theory, the dominant filtration process for 100 nm particles is through diffusion by Brownian motion. Increased velocities reduce the time available for diffusion, which in turn decreases the fraction of particles which can penetrate the filter through diffusion. For 300 nm aerosol particles, diffusion remains significant, but deposition due to impaction and interception (which increase with velocity) are greater. Fig. 2 illustrates the need to conduct penetration test at multiple particle sizes.

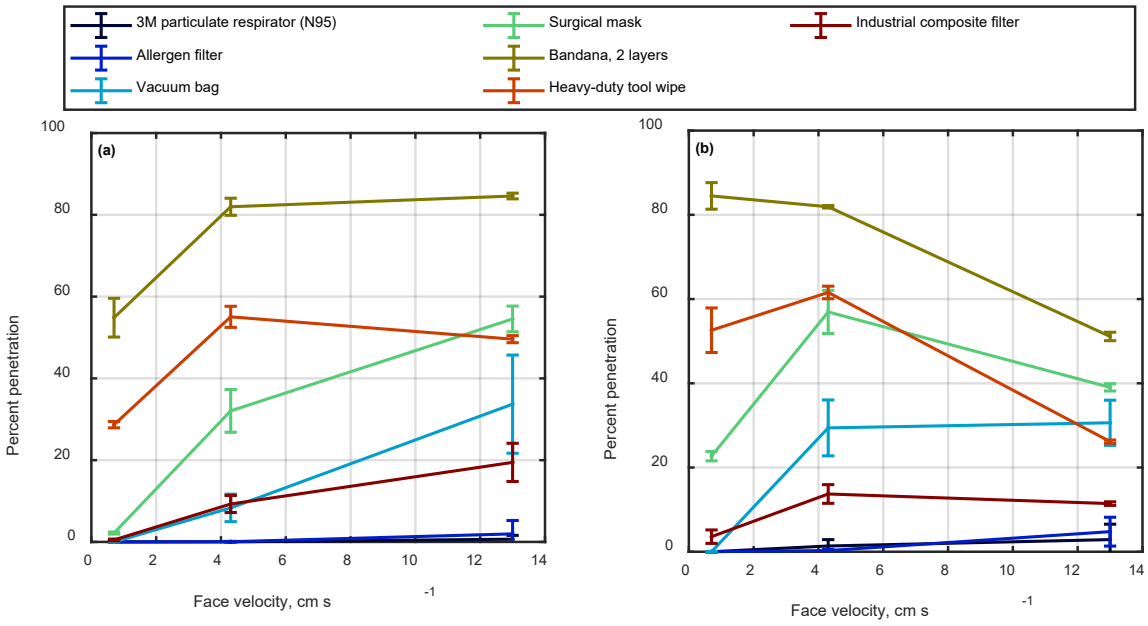


**Figure 2** Percent penetration as a function of face velocity for (a) 100 nm and (b) 300 nm NaCl aerosol particles.

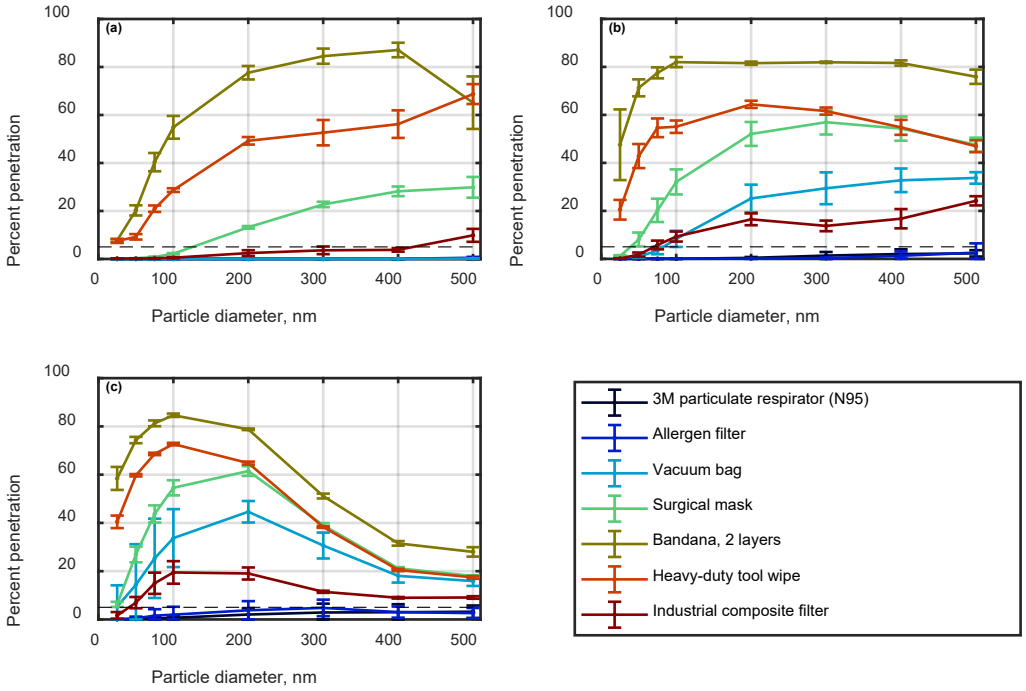


**Figure 3** Percent penetration as a function of particle size at a face velocities of 0.70 cm $s^{-1}$, 4.30 cm $s^{-1}$, and 13.0 cm $s^{-1}$ are shown in (a), (b) and (c), respectively. The dashed lines indicate 5% penetration.

Percent penetration as a function of particle diameter over the range 25-500 nm are reported in Fig. 3, as the means (and standard deviations) of the three replicates for each filter material and face velocity. For reference, the 100 nm and 300 nm data at the highest face velocity (13.0 cm $s^{-1}$) are also summarized in Table 2. Unfortunately, the only filter materials for which 25-500 nm particle penetration did not exceed 5% at the highest face velocity were the N95 respirator and the allergen filter. Considering 300 nm particles at the highest face velocity, the N95 material allows passage of 3% of particles. The next best material was the allergen filter which allowed 5% penetration, followed by the industrial composite filter which allowed 11% penetration. The surgical mask failed to

meet the ≤ 5% threshold at 4.30 cm $s^{-1}$ for particles greater than 75 nm, and failed for all diameters at 13.0 cm $s^{-1}$. This is in agreement with another study which found that surgical masks do not provide adequate protection from the inhalation of submicron aerosol particles (MacIntyre & Chughtai, 2015). The weakest performance was observed for the bandana, which allowed 51% penetration of 300 nm and 85% penetration of the 100 nm at the highest face velocity.

According to a study on cough-generated aerosol particles, 4000-8000 particles with diameters 350-500 nm may be generated from a single cough from an individual infected with influenza (Lindsley et al., 2010). This study indicates that it is important to limit the inhalation of the two largest diameters in our study. Interestingly, the percent of 400 and 500 nm particles that penetrated all but two of the filter sampler materials (N95 respirator, allergen filter) is higher at the face velocity representative of light or moderate work (4.3 cm $s^{-1}$) than at the higher face velocity used here to represent a higher degree of physical exertion (13.0 cm $s^{-1}$). This suggests that the "alternative" materials provide better protection against 400-500 nm aerosol particles if one's activity level is increased.

Pressure drop across the filter is also a factor must also be measured in order to determine the quality of the filter material $q_f$, as shown in Eq. (1). The pressure drop $\Delta pres$ was determined by measuring the pressures in the line upstream ($p_{up}$) and downstream ($p_{down}$) from the filter holder and calculating the difference between the two in mm $H_2O$.

$$\Delta p = p_{up} - p_{down} \tag{5}$$

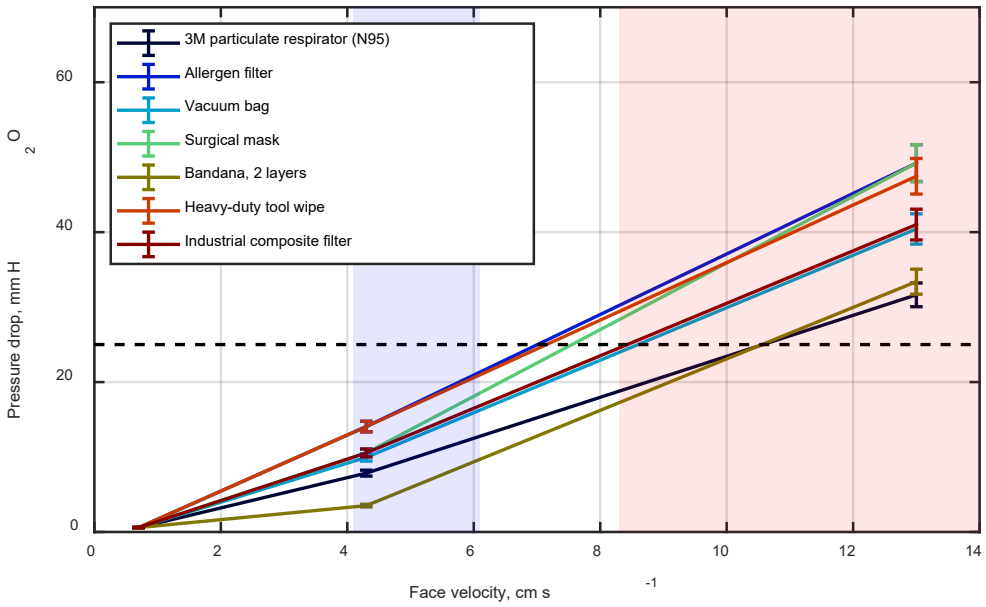


**Figure 4** Pressure drop across each filter material is shown. The dashed line indicates the maximum pressure drop allowed in NIOSH testing, 25 mm $H_2O$, based on human breath during exhalation. The blue shaded region indicates the face velocities observed during light physical work and the red shaded region indicates the face velocities observed during heavy physical work, according to the breathing flow rates given in Anderson et al, 2006 and assuming a filtration area of 100 $cm^2$.

The pressure drops across each filter material (in mm $H_2O$) for each face velocity are shown in Fig. 4. For all materials tested, pressure drop increases with face velocity, and the relationship between the two is approximately linear, as shown in Fig. 4. Additionally, pressure drop varies greatly with material. It should be noted that NIOSH certification testing 42 CFR 84.180 requires pressure drops across candidate materials to not exceed 35 mm $H_2O$ via inhalation or 25 mm $H_2O$ via exhalation at a face velocity of 9.3 cm $s^{-1}$ (NIOSH, 1995; Rengasamy et al., 2017). The pressure drops measured for each material at 4.30 cm $s^{-1}$ (the face velocity that corresponds with breathing during light

physical work) fell in the range 0-14 mm $H_2O$. Unfortunately, all of the candidate materials exceed these limits at the highest face velocity (13.0 cm $s^{-1}$), which corresponds with breathing during heavy physical work. Therefore, a person who is resting or performing light physical work will be wearing an adequate mask. Unfortunately for a person engaging in heavier physical work, the pressure drop exceeds the NIOSH limit for all materials tested.

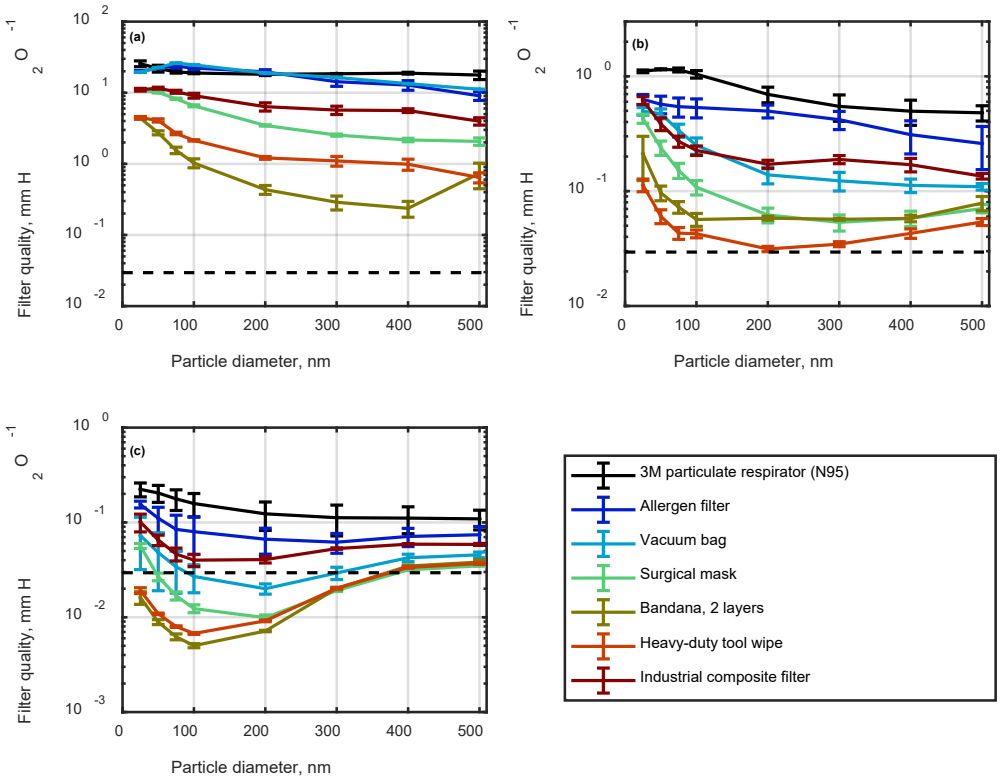


**Figure 5** Filter quality of each sample for a face velocity of 0.70 cm $s^{-1}$, 4.30 cm $s^{-1}$, and 13.0 cm $s^{-1}$ are shown in (a), (b), and (c), respectively. The dashed line represents the minimum filter quality recommended by an interim guidance published by the WHO on June 5, 2020 (reference number WHO/2019-nCov/IPC_Masks/2020.4).

The filter quality values of each filter material (in mm $H_2O^{-1}$) for each face velocity are shown in Fig. 5. According to an interim guidance released by the WHO on June 5, 2020, the minimum recommended filter quality for a face mask is approximately 0.03 mm $H_2O$ $mm^{-1}$ (WHO, 2020). This threshold is met or exceeded by all candidate materials and particle diameters at 4.3 cm s-1, and by the N95 respirator, the allergen filter, and the industrial composite filter for all particle diameters at 13.0 cm $s^{-1}$. The vacuum bag only falls short for 200 nm aerosol particles, while the surgical mask fails to meet this threshold for 75-300 nm aerosol particles. The heavy-duty tool wipe and the bandana only meet or exceed the minimum filter quality for aerosol particles with diameters greater than or equal to 400 nm.

If the filter materials in this study are ranked by filter quality, then at the highest face velocity the most effective material is the N95 respirator, followed by the allergen filter, the industrial composite filter, the vacuum bag, the surgical mask, and the heavy-duty tool wipe in descending order. The bandana is the least effective option, even though two layers of the fabric were used in each sample. Interestingly, the ranking of materials for mask construction varies if the materials are ranked according to percent penetration or filter quality. For example, the bandana is ranked seventh in percent penetration at 4.3 cm $s^{-1}$, but it is ranked sixth according to filter quality because its pressure drop is lower than the heavy-duty tool wipe. At 13.0 cm $s^{-1}$, however, the bandana is ranked seventh in both percent penetration and filter quality.

Filter quality also varies with particle diameter for each filter material and face velocity. At the highest face velocity in this study, 13.0 cm $s^{-1}$, the filter quality of the N95

respirator and allergen filter decreases with particle diameter, while the filter quality of the remaining samples is lowest at 100-200 nm, and increases for particle diameters > 200 nm.

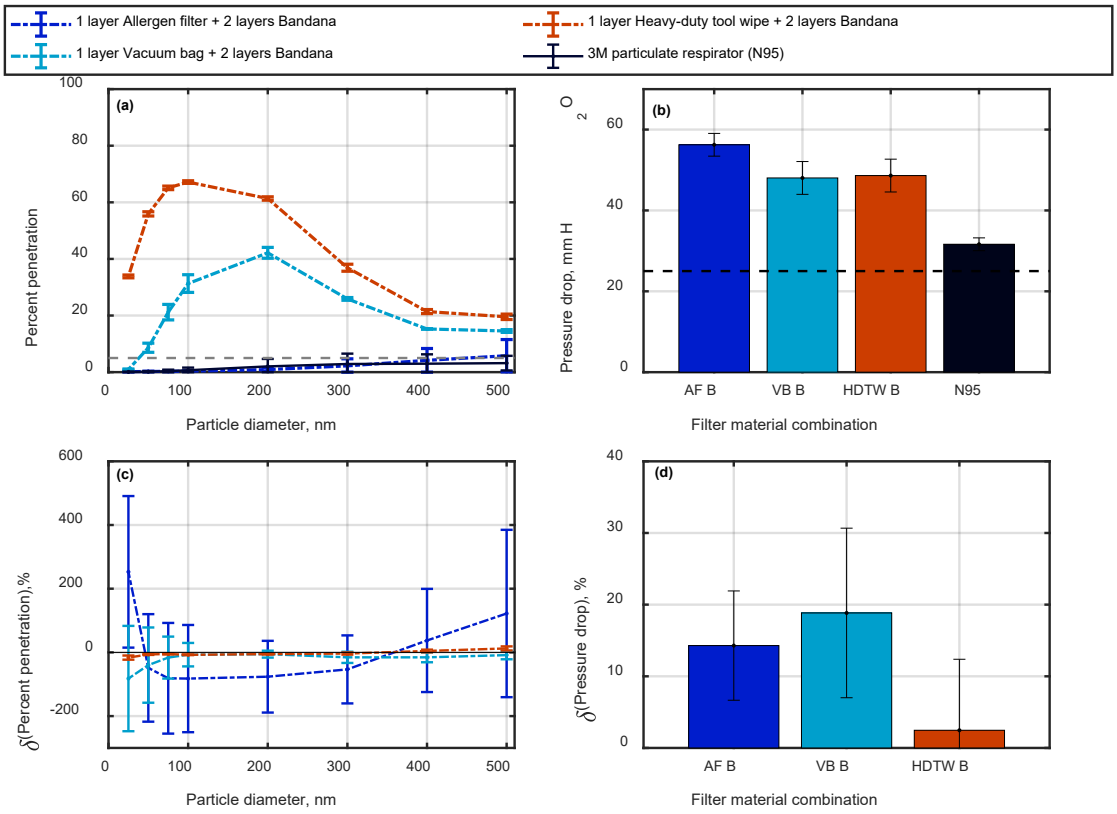


**Figure 6** (a) The percent of particles that penetrated each filter/bandana combination at face velocity 13.0 cm $s^{-1}$ are shown. The percent penetration for the N95 particulate respirator from Figure 3c is shown as a reference. The gray dashed line indicates the 5% penetration cutoff for N95 certification. (b) The pressure drops across each filter/bandana combination are shown (AF B = one layer of allergen filter and two layers of bandana, VB B = one layer of vacuum bag and two layers of bandana, and HDTW B = one layer of heavy-duty tool wipe and two layers of bandana). The black dashed indicates the maximum pressure drop allowed in NIOSH testing, 25 mm $H_2O$, based on human breath during exhalation. (c) The percent change in penetration percent, relative to the filter material without the two layers of bandana, was calculated for each filter/bandana combination. (d) The percent change in pressure drop, relative to the filter material without the two layers of bandana, was calculated for each filter/bandana combination.

In practice, many of the test materials would be used independently, but rather would be installed as a layer within a face mask. To represent two layers of cotton which would be used to make a simple mask, two layers of cotton bandana were added to one layer of the allergen filter, the vacuum bag, and the heavy-duty tool wipe. The percent penetration for each of these combinations at 13.0 cm $s^{-1}$ is shown in Fig. 6(a), and the N95 particulate respirator results from above are included as a reference. The percent of particles that penetrated through each combination varied from 0%±1% to 6%±6% for the bandana and allergen filter, 1%±1% to 42%±2% for the bandana and vacuum filter, and 20%±1% to 67%±1% for the bandana and heavy-duty tool wipe across the aerosol particle diameters studied. The percent penetration through the combination of the bandana and allergen filter is similar to that observed for combinations of fabrics in Konda et al. 2020, though the percent penetration for the other two combinations in our study are much higher.

The other two combinations, in which the vacuum bag and the heavy-duty tool wipe were combined with two layers of bandana, allowed greater particle penetration than observed for the layered materials in Konda 2020.

The pressure drop across each combination was also measured as shown in Fig. 6(b). Each combination was then compared with the performance of the allergen filter, vacuum bag, or heavy-duty tool wipe on its own in terms of percent penetration and pressure drop (Fig. 6(c) and Fig. 6(d) respectively). Percent penetration through the allergen filter decreased for 50-300 nm particles (by -49%±169% to -82%±168%). The large uncertainty in the decrease in percent penetration through the allergen filter is due

to the low percent penetration, and therefore high ratio of uncertainty to the measured value, before and after the addition of the cotton bandana material. Percent penetration through the heavy-duty tool wipe decreased for 25-300 nm particles (by -4%±3% to -16%±7%). Within the uncertainty in the measurements, the penetration of 25, 400, and 500 nm particles through the allergen filter, 25-500 nm particles through the vacuum bag, and 400 and 500 nm particles through the heavy-duty tool wipe, were unchanged.

The observed pressure drop for the allergen filter and the vacuum bag also increased when combined with two layers of cotton, 7.0 and 7.6 mm $H_2O$, respectively. The resulting pressure drops across each filter/bandana combination are higher than the maximum allowed filter drop for N95 certification, 25 mm $H_2O$. In summary, in some cases the combination of filter materials with two layers of cotton fabric improved their ability to filter particles, though this improvement was offset by the increases in pressure drop for some of the samples. The filter quality of the allergen filter somewhat increased for particle diameters 75-300 nm (9%±40% to 26% ±35%), and somewhat decreased for particle diameters 25 nm (-27%±10%), 50 nm (-2%±31%), 400 nm (-20%±34%), and 500 nm (-32%±34%), though the uncertainty in these measurements is high enough to show that these changes were not significant. The addition of the two layers of cotton bandana to the vacuum bag resulted in filter quality changes of -12%±7% to 34%±56%. Filter quality generally increased for the heavy-duty tool wipe, with increases of 10%±3% to 22%±3% for 25-200 nm particles and negligible change or small decreases for 300-500 nm particles. In summary, the addition of the bandana to each of these three

types of filter material resulted in an increase in filter quality for the heavy-duty tool wipe and negligible change for the allergen filter and the vacuum bag.

**Table 3** Construction, pressure drop, and biocompatibility of filter materials.

| Filter Material | Number of Layers | Pressure drop (mm $H_2O$) for 4.30 and 13.0 cm $s^{-1}$ | Biocompatibility |
|---|---|---|---|
| **3M particle respirator (N95)** | 1 | 3*, 7* | Confirmed biocompatible |
| **Allergen filter** | 1 | 14*, 49 | Potentially biocompatible |
| **Vacuum bag** | 1 | 14*, 42 | Potentially biocompatible |
| **Surgical mask** | 1 | 7*, 49 | Some confirmed biocompatible, some confirmed incompatible |
| **Bandana, 2 layers** | 2 | 7*, 35 | Potentially biocompatible |
| **Heavy duty tool wipe** | 1 | 7*, 42 | Potentially biocompatible |
| **Industrial composite filter** | 1 | 4*, 40 | Confirmed biocompatible |

*Materials for which the pressure drop did not exceed the maximum allowed during exhalation for N95 certification (25 mm $H_2O$) (NIOSH, 2015).

The biocompatibility of filter material candidates is also a consideration in DIY mask design. A mask material is considered biocompatible if its use does not result in additional health risks due to cytotoxicity, carcinogenicity, reproductive toxicity, or skin irritation (CEN, 2009). Such health risks arise due to direct contact with the wearer's face and the inhalation of gases, fibers, or other particles from the material(s) in the face mask. The U.S. FDA follows the International Standard ISO 10993 for determining

biocompatibility of medical devices, including respirators and medical masks (FDA, 2016). Table 3 summarizes the biocompatibility rating of the materials assessed in this study. The only filter materials for which biocompatibility have been confirmed is the N95 particulate respirator and the industrial composite filter. Surprisingly, it has been demonstrated that surgical masks do not always meet the criteria for biocompatibility (Sipahl, Bayram, Palabiyik, Bayram, & Aydin, 2018).

## Summary and conclusions

The filtration performance of a range of filter materials was assessed at three face velocities for the purpose of finding strong candidates for DIY face mask construction. Each material studied reduced the percentage of aerosol particles with diameters 25-500 nm. However, only the allergen filter and the N95 respirator met the threshold criteria of allowing ≤5% of particles to penetrate at each of the three face velocities employed. The next best results were obtained for the vacuum bag and the industrial composite filter, with percent penetrations of ≤34% and ≤24% under conditions of light work, and ≤45% and ≤19% under conditions of heavy work for 25-500 nm aerosol particles. Notably, the vacuum bag and the industrial composite filter each outperformed the surgical mask, with penetrations of ≤57% under light work and ≤61% under heavy work for 25-500 nm aerosol particles. The double-layered bandana was the least effective filtration material.

We also report filter qualities in this study, which take the pressure drop across each filter material into account. All materials met the minimum filter quality of 0.03 mm $H_2O^{-1}$ recommended by the WHO as of June 2020 at the face velocity that

corresponds with light physical work, 4.3 cm $s^{-1}$. The materials with the highest filter qualities at the highest face velocity were the N95 respirator and the allergen filter, followed by the industrial composite filter for 25-500 nm aerosol particles, all of which exceed the minimum recommended filter quality. Lower filter qualities were observed for the vacuum bag, which failed to meet the recommended minimum filter quality for 300 nm aerosol particles, and the surgical mask, which only met the minimum recommended filter quality for the smallest and largest particle diameters. The lowest filter quality values at this face velocity were observed for the two-layered bandana and the heavy-duty tool wipe, and neither of these materials met the recommended minimum filter quality for aerosol particles with diameters less than or equal to 300 nm.

The effect of layering filter material between two layers of a standard cotton bandana was also determined. Decreases in the percent penetration of 100 nm particles were observed when the allergen filter and vacuum bag were combined with the cotton bandana (-82%±168% and -7%±37% respectively), but these decreases were not significant in comparison with their uncertainties. The addition of the two layers of cotton bandana to one layer of the heavy-duty tool wipe did result in a significant decrease in percent penetration of 100 nm aerosol particles of -8%±1%. These results indicate that layering may decrease the percent penetration of aerosol particles through materials which perform poorly when used alone, but may not significantly enhance the protection provided by more effective filter materials.

Additional testing on the possible advantages and/or disadvantages of multilayered mask materials is a topic for future work. Unfortunately, improvements

observed in percent penetration may be offset by increases in pressure drop due to the added layers.

The materials that showed the most promise for DIY mask construction were two household materials (an allergen filter and a vacuum bag) and an industrial composite filter (which is available in bulk quantities) based on percent penetration, pressure drop, and filter quality. In addition, the industrial composite filter has previously been tested for biocompatibility, and is suitable for face mask materials, whereas the biocompatibility of the allergen filter and vacuum bag are unknown. Though not tested in this study, a final important consideration in mask design is the fit of the mask to the user's face. which will vary with mask design and the size and shape of the individual user's face.

# CHAPTER IV

# THE FIFTH INTERNATIONAL WORKSHOP ON ICE NUCLEATION PHASE 3 (FIN-03): FIELD INTERCOMPARISON OF ICE NUCLEATION MEASUREMENTS

## Background

A brief history of ice nucleation and INP measurement instrument comparisons will be summarized here. The first international workshop on condensation and ice nuclei was held in Lannemzam, France in 1967. This was soon followed by the second international workshop on condensation and ice nuclei in Fort Collins, Colorado, USA in 1970, and a third workshop focused on ice nucleation measurements in Laramie, Wyoming, USA in 1975. Following these three workshops, over thirty years elapsed before the Fourth International Workshop on Ice Nuclei (formally the 2007 International Workshop on Comparing Ice Nucleation Measuring Systems, or ICS-2007) which was held at the Aerosol Interaction and Dynamics in the Atmosphere (AIDA) facility at the Karlsruhe Institute of Technology in Eggenstein-Leopoldshafen, Germany. Participants from ICS-2007 then organized the Fifth International workshop on Ice Nucleation, which would consist of three phases. The first and second phases, called the Fifth International Workshop on Ice Nucleation Phase 1 (FIN-01) and Phase 2 (FIN-02) were held at the AIDA facility in late 2014 and March 2015, respectively. The third phase (FIN-03) was carried out at Storm Peak Laboratory in Steamboat Springs, Colorado, in September 2015, and is the subject of this paper.

The results from FIN-02 (DeMott et al., 2018) will be briefly summarized here in order to provide context for the results from FIN-03. During FIN-02, a total of 21 ice nucleation instruments with unique configurations were used to measure the concentration of immersion $N_{INP}$ in generated aerosol populations. The aerosol types included minerals, dust, soil, and one bacterial sample, Snomax. Across the range of participating instruments, an order-of-magnitude agreement immersion $N_{INP}$ was observed for most of the samples (with a notable exception in illite NX) over the temperature range employed in the study (-40 °C to -5 °C). This level of convergence observed between such diverse measurement systems in a laboratory setting indicated that these systems were ready for the additional challenges inherent in a comparison carried out in a field setting, which would take place in FIN-03.

The goals and objectives of FIN-03 were to

1) Compare ice nucleation measurement systems under the conditions of a field campaign, in which low aerosol particle concentration and variable aerosol composition, size distribution, and total concentration present unique challenges to the instruments being studied;
2) Compare the performance of measurement systems which employ vastly different techniques (direct vs. post-processing) for the determination of INP concentration
3) Gain insights into the ability of the ice nucleation measurement systems to effectively produce the conditions required for the initiation of ice nucleation in the immersion mode and in the deposition mode.

The intention of paper is to present the results from FIN-03 from the perspective of a referee unassociated with any of the ice nucleation instruments represented during the study. This paper is not intended as a detailed analysis of the operation of each instrument, but as an evaluation of the relative performance of the instruments in measuring INP in the immersion and deposition modes.

## Methods

A combination of direct-processing (online) and post-processing (offline) ice nucleation instruments were employed during the FIN-03 field campaign. Amongst the on-line measurements, was the well-established Colorado State University CFDC. The CSU-CFDC is arguably the most well-established technique for counting total number of particles which act as INP. Online instruments have the significant advantage that the aerosol being evaluated as INPs remain airborne, and never touch a substrate nor endure shipment to a laboratory. In the CSU-CFDC, in-situ particles travel directly into the inner chamber and are exposed to set temperature and supersaturation conditions. Those which grow to be ice crystals are detected by size-discrimination at the base of the chamber. A second online instrument, the SPectrometer for Ice Nuclei (SPIN; Droplet Measurement Technologies, Boulder, CO) is a parallel plate continuous flow diffusion chamber style instrument also sampled during FIN-03 (Garimella et al., 2016; Garimella, Rothenberg, Wolf, David, Kanji, Wang, Rösch, et al., 2017). For many years, online techniques have been considered the superior technique due to the advantage of free-floating unaltered aerosol. However, online techniques, i.e. those in which samples are

collected in the field and sent to a laboratory for subsequent nucleation experiments, have undergone many improvements in recent years and some have have been successful in other recent intercomparisons as well (DeMott, 2018; Hiranuma et al., 2015; Wex et al., 2015).

**Table 4** Descriptions of INP instruments.

| | Instrument | Type | Institute | References |
|---|---|---|---|---|
| **Online/ direct** | Continuous flow diffusion chamber (CSU-CFDC) | Continuous flow diffusion chamber (cylindrical) | Colorado State University | (Eidhammer et al., 2010; Rogers, 1988; Rogers, DeMott, Kreidenweis, & Chen, 2001) |
| | Spectrometer for ice nuclei (MIT-SPIN) | Continuous flow diffusion chamber (parallel) | Massachusetts Institute of Technology | (Garimella et al., 2016; Garimella, Rothenberg, Wolf, David, Kanji, Wang, Rosch, et al., 2017; Kulkarni & Kok, 2012) |
| **Offline/ post-processing** | Frankfurt Ice Nuclei Deposition Freezing Experiment (FRIDGE) | Cold stage droplet freezing array (on wafers) | Goethe University Frankfurt | (Schrod et al., 2016) |
| | Ice spectrometer (CSU-IS) | Aliquot freezing array | Colorado State University | (Hill et al., 2016; Hiranuma et al., 2015) |
| | Cold stage (NCSU-CS) | Cold stage droplet freezing array | North Carolina State University | (Hader, Wright, & Petters, 2014; Hiranuma et al., 2015; Wright & Petters, 2013) |

One example of the offline techniques is the FRankfurt Ice Nuclei Deposition FreezinG Experiment (FRIDGE). The FRIDGE is a unique offline technique in which

ambient aerosols are collected onto a substrate in the field, and then, in the laboratory subjected to either immersion or deposition freezing experiments. Also, included in the FIN-03 project were data collected with impingers and filter samplers and analyzed on the NCSC Cold Stage, an and the CSU Ice Spectrometer.

A summary of instrument information is provided in Table 4, and the operating principles and experimental methods for each instrument are provided in the Appendix.

**Immersion and deposition measurements and sample collection**

During FIN-03, the activation of atmospheric particles as INP was studied under two sets of conditions corresponding to two different ice nucleation modes, immersion and deposition. While immersion nucleation is believed to the most common heterogeneous ice nucleation mechanism, it is not the only pathway to frozen INP at temperatures above -38 °C (Kanji et al., 2017).

The online CSU-CFDC and MIT-SPIN instruments "immersion data" including in the intercomparison was collected at operating conditions of 104-106% RH (relative humidity with respect to water), to ensure droplet stability in the internal chamber and thus to represent the immersion freezing process.

Conversely, all "deposition" mode data was collected under conditions of 94-100% RH to avoid the presence of droplets and to represent freezing by deposition of water molecules from the gas phase. Only one offline instrument, the FRIDGE measured both immersion and deposition nucleation. Instead of relying on conditions to define nucleation mode, the offline FRIDGE instrument has two entirely different mechanism-

specific procedures to directly measure immersion (initiated with droplets on the sample) and deposition processes (initiated with exposure to gas phase water only, and no droplets).

**Weather and properties of aerosol particles**

Variations in weather conditions and the availability of aerosols to act as INP were characterized using auxiliary measurements as discussed in this section. Weather data was obtained for Storm Peak Laboratory (STORM) through MesoWest. Air temperature, relative humidity, and barometric pressure time series are shown in Fig. (a), 7(b), and 7(c) respectively.

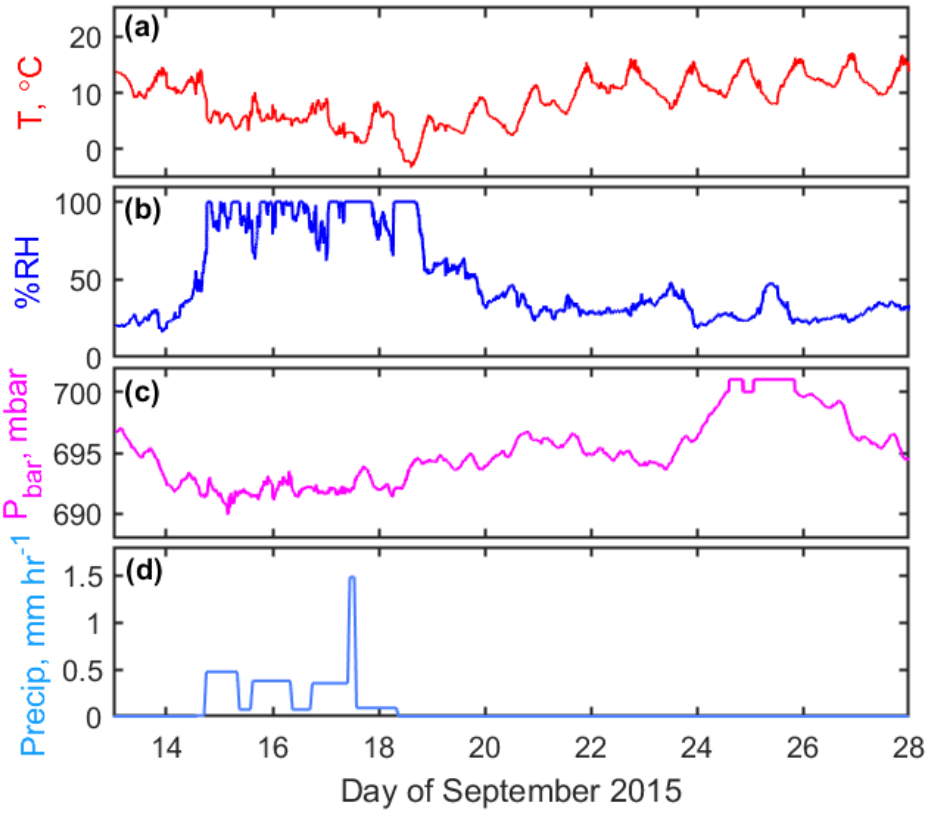


**Figure 7** Weather conditions over the course of FIN-03, including (a) air temperature, (b) relative humidity, (c) barometric pressure, and (d) precipitation rate.

The MesoWest archive did not contain data from September 14 or September 15. Therefore, the weather data for these variables was supplemented with measurement from Storm Peak Lab (SPL) through the Western Regional Climate Center (WRCC) for these two days. Precipitation was measured via rain gauge at Storm Peak Laboratory. Precipitation rate was calculated from the quotient of precipitation (in mm) and time collected (in hours), as shown in Fig. 7(d).

Relatively warm, dry conditions were observed initially at the Storm Peak Laboratory. Clear skies on September 11 and 12, 2015 gave way to clouds and haze on September 13. Cooler temperatures, lower barometric pressure, and higher relative humidity (generally above > 70%) accompanied rainfall on September 14. This was followed by continued rain on September 15, intermittent rain and short periods of hail on September 16, a mixture of rain, snow, and sleet on September 17, and snow on September 18. The next and longest period in the study, September 19 to 28, was marked by an increase in temperature, an increase in barometric pressure, lower relative humidity, and a lack of precipitation. More detailed weather records can be found in the Appendix.

A Laser Aerosol Spectrometer (LAS, model 3340, TSI Inc., St. Paul, Minnesota, USA) was used to measure the aerosol size distribution over the diameter range 0.089-10 μm. The sample flow rate was fixed at 0.1 L $min^{-1}$. Size calibrations were performed using polystyrene latex spheres (PSL, Duke Scientific). PSL diameters were converted to ammonium sulfate equivalent diameters using Mie theory (Froyd et al., 2019). Particle concentrations are reported as a function of ammonium sulfate diameter. Volume and

surface area distributions are derived assuming spherical particles. The PALMS instrument was used for ambient sampling nearly continuous during FIN-03 from Sept 17 onward. The maximum and minimum total LAS concentrations were 518 $cm^{-3}$ and 626 $cm^{-3}$ respectively, and the mean and standard deviation of the total LAS concentration throughout FIN-03 were 571 $cm^{-3}$ and 19 $cm^{-3}$ respectively. The time series of aerosol size distribution measured by the LAS (in three hour means) is shown in Fig. 8. The y-axis in this figure has been truncated at 3 μm because few particles with diameter > 0.5 μm, and essentially zero particles with diameter < 3 μm, were present over the course of the FIN-03 field campaign. The highest total aerosol concentration recorded during FIN-03 (604 $cm^{-3}$) occurred just before midday on September 17. Elevated aerosol concentration (at least one standard deviation above the mean) was also observed midday on September 18, late on September 19, and early on September 21.

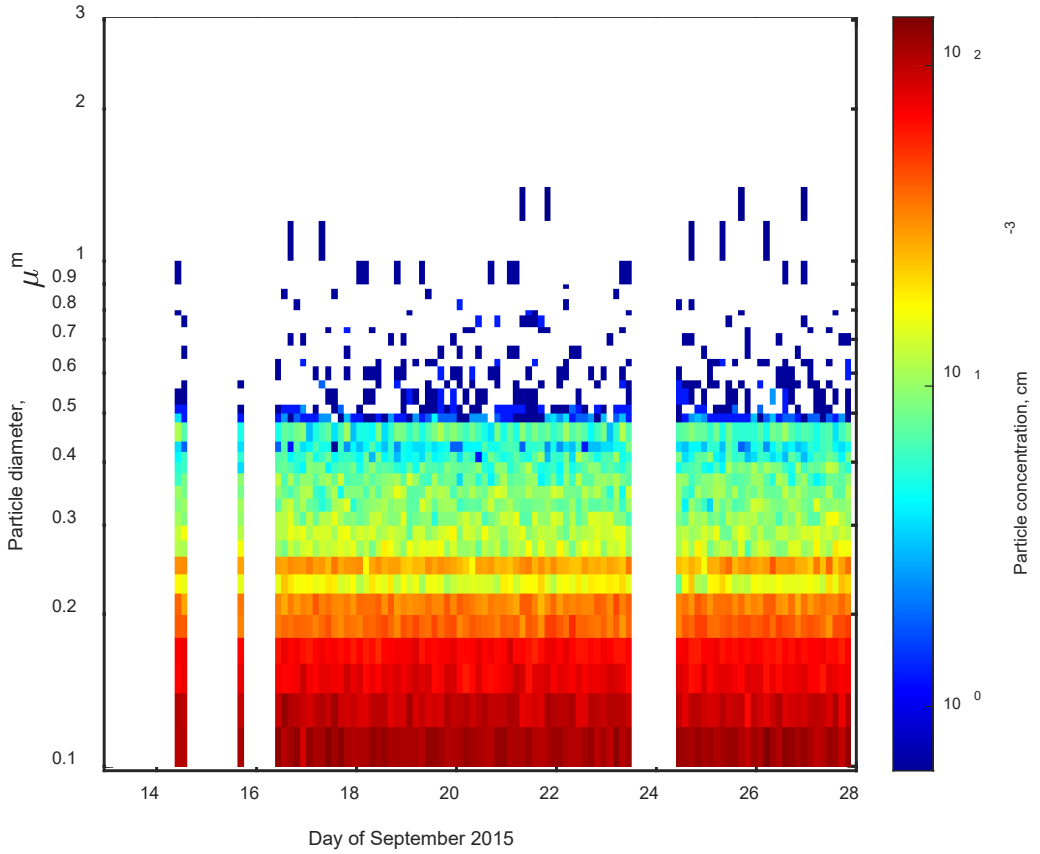


**Figure 8** Time series of particle distribution measured by the laser aerosol spectrometer (LAS). The concentrations are shown as three-hour means.

Composition strongly influences the ability of aerosol particles to activate as INP (Kanji et al., 2017; Murray, O'Sullivan, Atkinson, & Webb, 2012). Measurements of the composition of 0.2 to 3.0 µm aerosol particles were conducted using the particle analysis by laser mass spectrometry (PALMS) instrument designed and operated at the National Oceanic and Atmospheric Administration (NOAA) as described (Thomson, Schein, & Murphy, 2000). In brief, aerosol particles are sampled, focused and accelerated via an aerodynamic lens inlet (Schreiner et al., 2002). Next, particles enter a vacuum chamber where they successively pass through two continuous-wave detection laser beams (532

nm Nd:YAG) and scatter light. Based on the transit time, their vacuum aerodynamic diameters ($d_{va}$) are determined. The detection signal triggers an ArF excimer laser that emits 193 nm pulse to ablate and ionize single particle in one step. The resulting ions are analyzed with a unipolar time-of-flight mass spectrometer, which allows polarity switching during the flight and thereby producing positive or negative mass spectra for individual particles.

The mass concentration of aerosol particles with characteristic spectra belonging to eight categories (sulfate/organic/nitrate, biomass burning, elemental carbon, sea salt, mineral dust, meteoric, alkali salt, and fuel oil combustion), and the mass concentration of unclassified aerosol particles by the PALMS, is shown in Fig. 9(a). The daily averaged mass fractions of each category, which were calculated as the fraction of the total aerosol mass measured by the PALMS in each of the nine categories, is shown in Fig. 9(b). The dominant categories throughout the FIN-03 campaign were biomass burning, sulfate/organic/nitrate, and mineral dust. Mineral dust and biogenic organic compounds are often internally mixed in aerosol particles (Zawadowicz et al., 2019), and it is therefore possible that many of the same particles which contained organic compounds and products of biomass burning also contained mineral dust. Negligible contributions from elemental carbon, meteoric particles from the stratosphere, or fuel oil combustion were measured during the campaign. Increased contributions from sea salt (4%) and alkali salt (3%) were observed on September 16, and an even larger contribution from sea salt (16%) was observed on September 18. The higher prevalence of salt-rich aerosol particles on these days may represent hygroscopic cloud

condensation nuclei transported from aloft via rainfall. The highest total mass concentration measured by the PALMS (6.5 μ $m^{-3}$) occurred on September 14 (of which 4.0 μ $m^{-3}$ consisted of biomass burning), and the second highest total mass concentration (5.3 μ $m^{-3}$) occurred on September 26 (of which 1.6 μ $m^{-3}$ was classified as sulfate/organic/nitrate, 1.7 μ $m^{-3}$ was classified as mineral dust, and 1.0 μ $m^{-3}$ was classified as biomass burning).

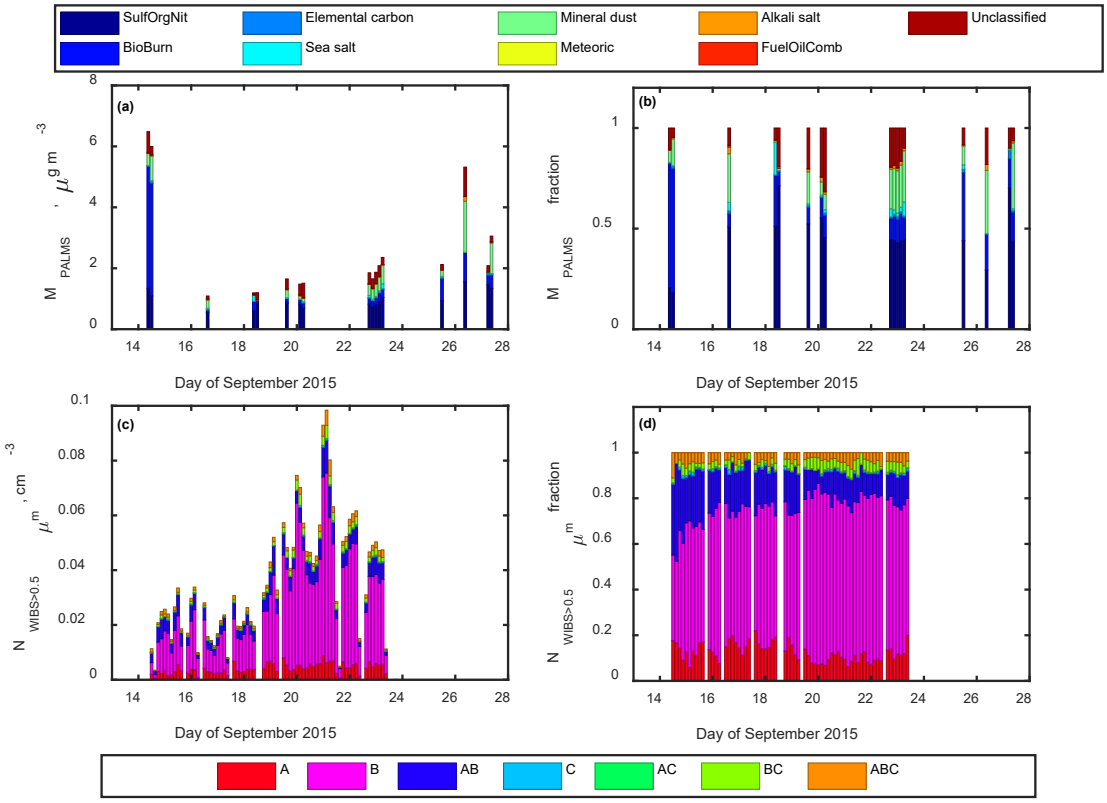


**Figure 9** Subplots (a) and (b) show the mass concentration and relative fractions (by mass) of each of the nine PALMS categories for the three-hour periods during which the PALMS was used to sample ambient air. Subplots (c) and (d) show the aerosol particle number concentration and relative fractions (by count) of particles with diameter > 0.5 μm in each of the seven WIBS channels over the course of the FIN-03 field campaign.

Additionally, fluorescent properties of individual aerosol particles were detected using the NOAA Wideband Integrated Bioaerosol Sensor, model 4A (WIBS-4A; Droplet Measurement Technologies, Longmont, CO). The WIBS-4A is described in detail elsewhere (Gabey et al., 2010; Kaye et al., 2005; Perring et al., 2015) and is only briefly summarized here. As described in Zawadowicz et al., 2019, the gain for the WIBS used at Storm Peak was set so as to detect and classify particles between 0.4 and 10 μm. First, the optical diameter of particles entering the detection cavity is determined by light scattered during transit of a 635nm laser beam. This signal triggers the sequential firing of two xenon flash lamps filtered to produce narrow excitation wavebands centered at 280 and 370 nm. The resulting fluorescence is detected by two wideband photomultiplier detectors observing 310-400 nm (the FL1 detector) and 420-650 nm (the FL2 detector).

Fluorescing particles were categorized according to the intensity of the signal in each of three channels (channel A excitation 280 nm/emission 310-400 nm, channel B excitation 280 nm/emission 420-650 nm, channel C excitation 370 nm/emission 420-650 nm). Particles for which the measured emission intensity in only one channel met the threshold (such that the signal intensity exceeded the value equal to three standard deviations above the mean) were assigned Type A, B, or C, and particles for which the measured emission intensity in two or more channels met the threshold were assigned Type AB, BC, BC, or ABC (Perring et al., 2015). The daily average number concentration of fluorescing aerosol particles corresponding with each of the seven WIBS types with diameter > 0.5 μm is shown in Fig. 9(c), and the daily average number fraction of each WIBS type is shown in Fig. 9(d). The dominant components of

fluorescent aerosol particles throughout the FIN-03 field campaign were types B, AB, and A, which accounted for 63.2%±8.7%, 16.0%±6.3%, and 12.5%±3.9% of the particles detected by the WIBS respectively. In contrast with the daily average mass fraction in each PALMS category, the relative contributions of each of the seven WIBS particle types did not vary much over the course of the study, with perhaps the exception that Type AB decreased slightly in prevalence from September 14 (42.9%) to September 21 (10.1%). The highest total fluorescing particle concentration (for particles with diameter > 0.5 μm) was measured by the WIBS on September 21 (0.1 $cm^{-3}$), and the lowest concentration was on September 17 (0.02 $cm^{-3}$). WIBS data was not collected on September 13-16 or on September 27. Time-resolved size distributions for each WIBS channel, as well as the total particle concentration measured across these seven channels, are shown in Fig. A1.

## Results and Discussion

### Immersion observations

A summary of the number concentrations of immersion mode INP ($N_{INP}$) immersion measurements over the course of the field campaign is shown in Figure 10. Measurements were conducted over a wide range of temperatures, -7 to -34 °C in the heterogeneous ice nucleation regime. The concentration of INP detected over this range varied by over five orders of magnitude (0.01 to 160 $L^{-1}$). Sampling such a broad data set allows consideration of instrument performance in response to the presence of highly active INP (i.e. those facilitating freezing at temperatures ≥ -10 °C) as well as more modestly effective INP (-10 °C ≥ T ≥ -30 °C). In addition, the range of INP concentrations includes lower concentrations which challenge instrumental signal to noise limits.

Broadly speaking, a general trend of increasing $N_{INP}$ with decreasing temperature was observed by the for the FRIDGE, CSU-IS, NCSU-CS, and CSU-CFDC. The single available MIT-SPIN data point also fall well within the concentration range reported for the other instruments. The concentrations reported by all instruments at each temperature vary by more than two orders of magnitude, inevitably due to variations in the weather conditions and the nature and concentrations of available aerosol described above. Generally higher $N_{INP}$ measurements were obtained with the FRIDGE and the CSU-IS than the CSU-CFDC and NCSU-CS analysis of both filter and impactor samples.

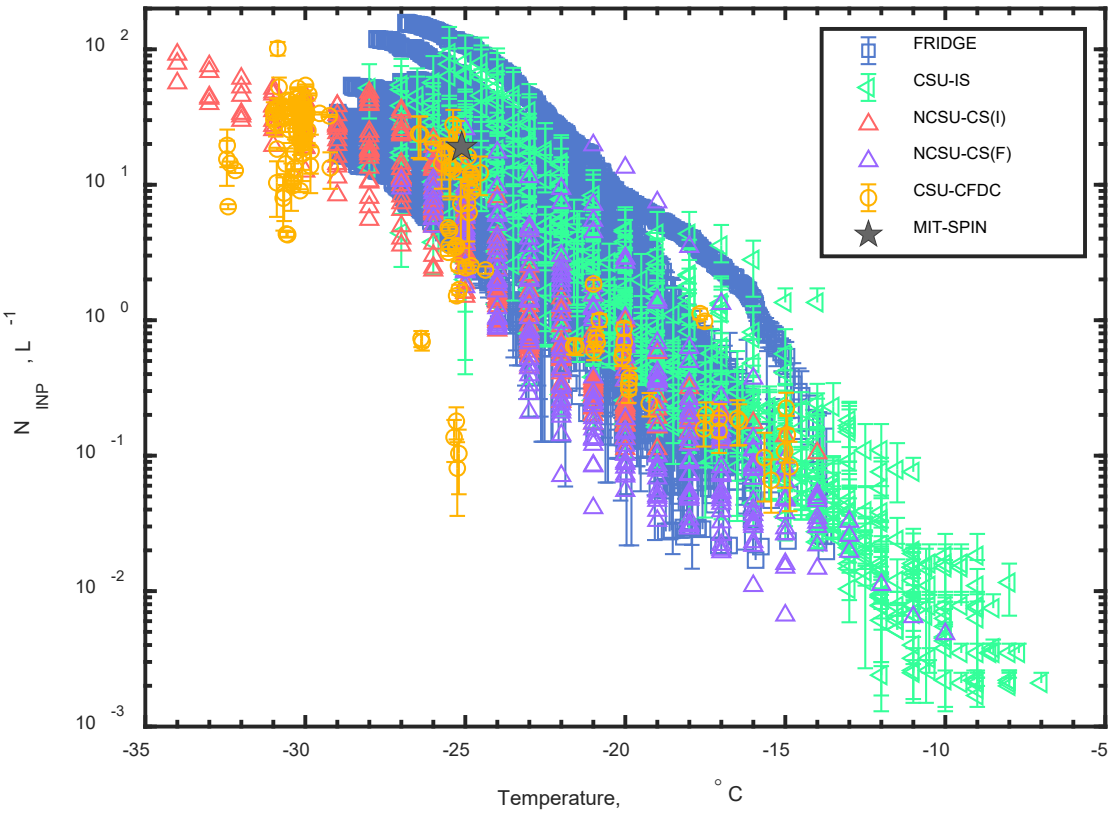


**Figure 10** A summary of the instruments participating and the setpoint temperatures that were used for measuring immersion INP. The time period over which the INP concentration has been averaged for each instrument is explained in the text. Note that NCSU-CS(I) and NCSU-CS(F) denote measurements made by the cold stage from samples collected using the impinger and the filter, respectively.

While such general statements can be made from the data as presented in Fig. 10, it is difficult to compare the operation of these instruments without considering changes over time. Therefore, the mean and standard deviation of immersion $N_{INP}$ were calculated over three-hour periods for each instrument (except for the MIT-SPIN) at 1 °C intervals (± 0.5 °C) and plotted as a time series, as shown in Fig. 11. For the online measurements included in Fig. 11, the relative humidity within each instrument was set

to the range 104-106% RH. The offline methods determination of immersion freezing temperatures is not specific to a set supersaturation.

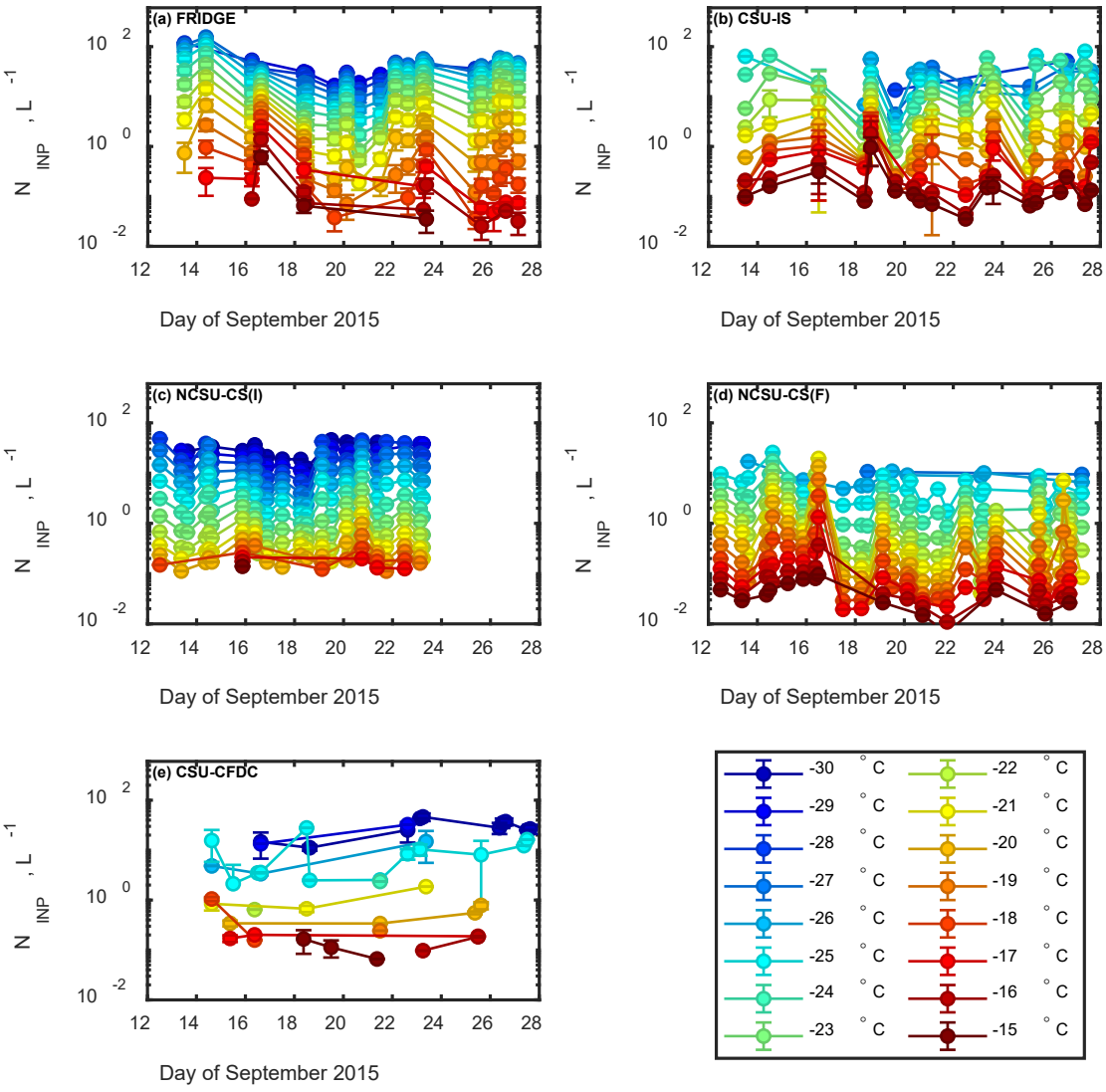


**Figure 11** Time series of immersion-mode INP concentrations measured by (a) the FRIDGE from Goethe University Frankfurt, (b) the CSU ice spectrometer, (c) the NCSU cold state (collected using an impinger), (d) the NCSU cold stage (collected using the filter), and (e) the CSU continuous flow diffusion chamber. INP concentrations shown in this figure are averaged over three-hour periods.

It is interesting to note that temporal changes in immersion $N_{INP}$ are more apparent for some instruments and collection methods than others. For example, on September 16 distinct increases in INP concentrations were measured by the FRIDGE and the NCSU-CS (collected by filter). The CSU-IS and the NCSU-CS (collected by impinger) observed noticeably smaller increases. This difference may be due to the ability of each instrument or collection method to collect particles of specific size ranges. Specifically, the filter is more effective in collecting 0.2-1.0 μm particles than the impinger, which may explain the discrepancies between immersion $N_{INP}$ measured by the NCSU-CS collected by these methods.

No significant ($0 < 0.05$) correlation was found between changes in composition (from the PALMS categories and WIBS channels) and immersion $N_{INP}$ across the range of setpoint temperatures employed during FIN-03. Based on the sharp increase in mineral dust measured by the PALMS on September 26 did not appear to correspond with an increase in immersion $N_{INP}$ on the same day. An increase in overall fluorescing aerosol concentration measured by the WIBS over the period September 22-25 similarly did not result in an increase in immersion $N_{INP}$ during this period.

Further analysis was performed to compare individual instruments on a one-to-one basis. The ratios of time-matched three-hour immersion $N_{INP}$ means were calculated for each pair of instruments, as shown in Fig. A2 in the Appendix. The mean $N_{INP}$ reported by each instrument nearly always agree within an order of magnitude, and always agree within two orders of magnitude, aside from a few discrepancies discussed below. This level of agreement compares well with the findings from FIN-02 that the

immersion $N_{INP}$ measured by several online and offline instruments agreed within an order of magnitude. This is encouraging given that FIN-02 was a laboratory intercomparison on single composition aerosol samples whereas FIN-03 is a field campaign in which constant changes in the concentration, size distribution, and composition of the ambient aerosol population at Storm Peak Laboratory were all factors. This shows that field data can be collected with nearly same level of accuracy as laboratory experiments. The participants' efforts to demonstrate convergence between the diverse set of ice nucleation instruments have also been successful.

The best agreement throughout the study was observed between the FRIDGE and the CSU-IS, in which only one out of seventy-two 3-hour $N_{INP}$ means (1.4%) did not agree within an order of magnitude. The CSU-CFDC generally agrees with the other measurements within an order of magnitude, and its measurements also tend to be lower than those from the FRIDGE and CSU-IS (for the same day/temperature) and higher than those from the NCSU-CS collected by impinger and filter (once again, for the same day/temperature). The worst agreement overall was observed for the FRIDGE and the NCSU-CS (collected by the impinger), a combination for which 12 out of 36 (33%) immersion $N_{INP}$ means did not agree within an order of magnitude. Agreement between the CSU-IS and the NCSU-CS (collected by the impinger) was only slightly better, as 6 out of 20 (30%) time-matched $N_{INP}$ means did not agree within an order of magnitude. Imperfect agreement was observed between the two collection methods which were analyzed by the in which only 10 out of 144 (7%) points means collected by the NCSU-CS impinger and filter and analyzed in the identical off-line apparatus differed by more

than an order of magnitude. A possible explanation is that INP are highly sensitive to the size range of collected aerosol.

Close examination of the discrepancies between time-matched immersion $N_{INP}$ means measured by the instruments leads to a few interesting observations. The first is that all discrepancies which exceed one order of magnitude are found in the temperature range -25 °C to -18 °C, and that the discrepancies tend to have maximum values in the range -24 °C to -21 °C for each pair of matched instruments, with lower discrepancies at temperatures outside of this range. One explanation for the observations of maximum measurement discrepancy in this range is a lack of uniformity in instrument parameters, specifically the calibration of the setpoint temperature and relative humidity. The difference between the instruments will be maximized within a few degrees of the true onset temperatures of the immersed INP and many aerosol types. Several aerosol types which have been observed to initiate ice nucleation the range -25 to -15 include dust (Ardon-Dryer & Levin, 2014; Boose et al., 2016; Creamean et al., 2013), biomass burning (McCluskey et al., 2014), and marine and continental biological aerosols (Huffman et al., 2013; Mason et al., 2015). Such an issue could be resolved by improving the characterization and control of setpoint temperature and relative humidity within the instruments. It should also be noted that this behavior may be composition-dependent, since the onset ice nucleation temperature of a particle is influenced by its composition. During the previous campaign, FIN-02, the FRIDGE, the CSU-IS, and the NCSU-CS were used to measure the concentrations of immersion INP from aerosol populations consisting of Tunisian soil dust, Argentinian soil dust, and K-feldspar across

the temperature range -35 °C to -5 °C. As in the current study, the NCSU-CS measured lower $N_{INP}$ than the FRIDGE or the CSU-IS across the temperature range -25 °C to -15 °C (and this discrepancy was at a maximum at approximately -19 °C) when the sampled aerosol was generated from Tunisian soil dust. This behavior was not replicated when Argentinian soil dust or K-feldspar were sampled, however, which may indicate that small changes in composition greatly influence the ability of these three instruments to measure immersion INP concentrations.

Interestingly, there are a few time periods on which discrepancies greater than one order of magnitude are observed for several instrument pairs. On September 14, discrepancies in immersion $N_{INP}$ greater than an order of magnitude are observed between the FRIDGE and the NCSU-CS (collected by impinger), the FRIDGE and the NCSU-CS (collected by filter), the CSU-IS and the NCSU-CS (collected by impinger), and the NCSU-CS (collected by impinger) the NCSU-CS (collected by filter), all within the approximate temperature range -25 °C to -20 °C. These discrepancies are found in 75%, 60%, 29%, and 33% of the temperatures for which time-matched data points were obtained for each set of paired instruments, respectively. These discrepancies were observed in measurements from early on September 14, a few hours before rainfall began, when wind blew in from the southeast and relative humidity consistently measured > 70%. This was also the time period associated with the highest aerosol mass concentration measured by the PALMS (6.5 $\mu g\ m^{-3}$ compared to the FIN-03 campaign mean 2.5±1.7 $\mu g\ m^{-3}$), and this aerosol population predominantly consisted of particles classified as BioBurn (3.9 $\mu g\ m^{-3}$, accounting for 62% of the PALMS total), followed by

SulfOrgNit (1.2 μg $m^{-3}$, accounting for 19% of the PALMS total) and mineral dust (0.6 μg $m^{-3}$, accounting for 10% of the PALMS total). In comparison, the average percentages (of the total PALMS measurement) throughout the FIN-03 campaign, BioBurn, SulfOrgNit, and mineral dust were 19%±17%, 45%±14%, and 15%±10% respectively. The aerosol particles samples on September 14$^{th}$ were therefore richer in compounds from biomass burning, poorer in sulfates, organics, and nitrates, and slightly poorer in mineral dust than average. In contrast, the total concentration of > 0.5 μm particles measured by the WIBS during this time period was relatively low (0.01 $cm^{-3}$ compared to the campaign mean 0.04±0.02 $cm^{-3}$)

Another period in which the immersion $N_{INP}$ measured by more than one pair of instruments did not agree occurred on September 23, when discrepancies greater than an order of magnitude are observed between the FRIDGE and the NCSU-CS (collected by impinger) over the temperature range -25 °C to -21 °C and between the FRIDGE and the NCSU-CS (collected by filter) over the temperature range -24 °C to -19 °C (71% and 55% of the temperatures for which time-matched data points were obtained for each set of paired instruments, respectively). This period was characterized by lower relative humidity (consistently < 50%), slightly high concentration of fluorescent aerosol particles with diameter > 0.5 (0.05 $cm^{-3}$ compared to the campaign mean 0.04±0.02 $cm^{-3}$), and low PALMS concentration (2.1 μg $m^{-3}$ compared to the FIN-03 campaign mean 2.5±1.7 μg $m^{-3}$). It should be noted, however, that the mineral dust measured by the PALMS was slightly elevated during this period (0.48 μg $m^{-3}$ compared to the campaign mean 0.41±0.43 μg $m^{-3}$).

Lastly, 63% of the immersion $N_{INP}$ measured by the FRIDGE and 29% of the immersion $N_{INP}$ measured by the CSU-IS exceeded those measured by the NCSU-CS (collected by filter) on September 26 by more than an order of magnitude. This period was characterized by the highest mass concentration in mineral dust measured by the PALMS over the duration of the FIN-03 field campaign (1.7 μg $m^{-3}$ compared to the campaign mean 0.41±0.43 μg $m^{-3}$) as well as high PALMS concentration (5.3 μg $m^{-3}$ compared to the FIN-03 campaign mean 2.5±1.7 μg $m^{-3}$). The WIBS was not used to measure the concentration of fluorescent aerosol particles on September 26.

The total particle concentrations measured by the LAS during these periods of discrepancy on September 14, September 23, and September 26 were 573±6 $cm^{-3}$, 579±29 $cm^{-3}$, and 569±7 $cm^{-3}$, compared to the campaign average of 570±20 $cm^{-3}$. Throughout the campaign, a positive trend between total particle concentration and $N_{INP}$ was observed for FRIDGE and CSU-IS measurements (though the former trend was weak), while no clear trend was observed between total particle concentration and $N_{INP}$ was observed for NCSU-CS or CSU-CFDC measurements. Additionally, no clear trend was observed between the concentration of particles with diameter > 0.5 microns and $N_{INP}$ for any of the instruments in this study.

Positive trends between the mass concentration of sulfates/organics/nitrates, compounds from biomass burning, and mineral dust, and $N_{INP}$, were observed for FRIDGE and CSU-IS measurements (for setpoint temperatures < -20 °C). However, trends between mass concentrations in these three categories and NCSU-CS measurements (whether sampling was performed using the filter or the impinger) were

very weak or absent. Positive trends between the mass concentration of sulfates/organics/nitrates and compounds from biomass burning, and $N_{INP}$, were observed for CSU-CFDC measurements (for setpoint temperatures < -25 °C), but no trend was observed between mineral dust concentration and CSU-CFDC $N_{INP}$. It should be noted that aerosols containing biological components are often internally mixed with mineral dust (Zawadowicz et al., 2019), which may explain why similar trends were observed between INP concentrations and the three previously listed PALMS categories for most of the participating instruments. In other words, it is possible that the positive response observed for the FRIDGE and CSU-IS may be due to either mineral dust or organic compounds present in the sulfates/organics/nitrates category (but not both), and the observed response to the other PALMS particle types may simply be correlation (rather than causation). Interestingly, the assessment of bioaerosol and mineral dust coincidence in Zawadowicz 2019 excludes particles produced through biomass burning from their analysis, and it is therefore uncertain whether the positive trends in $N_{INP}$ due to biomass burning concentrations can be extricated from the trends in $N_{INP}$ due to mineral dust concentrations.

To summarize, the concentrations of immersion INP increased more rapidly with increases in particle concentration, specifically total particle concentration, and the mass concentration of the three dominant PALMS categories (sulfates/organics/nitrate, biomass burning, mineral dust) for the FRIDGE and the CSU-IS than for the NCSU-CS. This may explain why the discrepancies between the FRIDGE and CSU-IS, and the NCSU-CS, were the largest when the concentrations of sulfates/organics/nitrates,

compounds from biomass burning, and mineral dust were elevated. The concentration of larger (> 0.5 μm) did not influence the level of agreement between the ice nucleation instruments.

### Immersion observations vs. predictions based on parameterizations

Because there is a tremendous need for accurate parameterizations of ice nucleation in regional and global climate models (Andreae & Rosenfeld, 2008; Morris et al., 2011; Seifert et al., 2011), several previously-developed ice nucleation parameterization were tested to evaluate how well they could predict the collective mean INP concentrations measured by all the participating instruments (P. J. DeMott et al., 2010; P. J. DeMott et al., 2015; Niemand et al., 2012; Tobo et al., 2013). Each parameterization was used to predict $N_{INP}$ at -30 °C, -25 °C, -20 °C, and -15 °C using the equations and inputs described in Table 5 and summarized below.

1) DeMott 2010 is a parameterization based on observed INP concentrations collected by the CSU-CFDC during multiple campaigns at locations globally (DeMott et al, 2010.) Concentrations of aerosols with diameters > 0.5 μm as measured by the LAS were used as the input for this parameterization.
2) DeMott 2015 is based on CSU-CFDC laboratory measurements of ice nucleation on dust samples collected under supersaturated conditions (105% RH) (DeMott, 2015). Here concentration of aerosols with diameters > 0.5 μm as measured by the LAS was used, employing the assumption that all particles in this size range were composed of mineral dust or particles that were similarly efficient as INP.

A correction factor of 3 was applied (as indicated in Table 5) according to the results in DeMott 2015 which showed that this correction factor resulted in the best fit between predicted and observed INP concentrations.

3) A variation on DeMott 2010 focused on biological INP in a Ponderosa pine forest in Colorado (Tobo 2013) was employed in 2 ways here. First, the concentration of aerosol particles with diameters > 0.5 μm measured by WIBS channels including Type C (C+AC+BC+ABC) was used in a parameterization based on the work in Tobo et al, 2013. It should be noted that this parameterization was developed based on fluorescing particle concentrations measured with a UV-APS an (excitation wavelength 355 nm, emission wavelength 420-575 nm), which corresponds most closely with the Type C particle detected by the WIBS. The Tobo parameterization was used once more, but the input was a "corrected" version of the WIBS channel C+AC+BC+ABC number concentration. The intention of this correction, based on the work of Healy et al 2014, was to determine the concentrations of fluorescing particles which would have been measured by a UV-APS, which is the most useful input for the parameterization from Tobo et al, 2013.
4) A second laboratory-based parameterization, Niemand 2012, based on measurements of dust as INP collected in the Aerosol Interaction and Dynamics in the Atmosphere (AIDA) cloud simulation chamber at the Karlsruhe Institute of Technology was also employed (Niemand et al., 2012). Unlike DeMott 2015, this parameterization incorporates measurements of mineral dust concentration and

surface area collected during FIN-03. The mass concentration of mineral dust measured by the PALMS was used in conjunction with size distributions from the LAS to determine the particle size distribution of mineral dust particles throughout the FIN-03 campaign, following a recently-developed method from (Froyd et al., 2019). The resulting mineral dust number concentrations and particle surface areas were then used as inputs in this parameterization.

**Table 5** Summary of parameterizations.

| Parameterization | Equation |
|---|---|
| **All particle types: (P. J. DeMott et al., 2010)** | $n_{INP}(T_k) = a(273.16 - T_k)^b\left(n_{a>0.5\mu m}\right)^{(c(273.16-T_k)+d)}$<br><br>$n_{INP}(T_k)$ = INP per standard liter<br>$n_{a>0.5\mu m}$= particles cm$^{-3}$ |
| **Mineral dust: Eq. (2) from (P. J. DeMott et al., 2015)** | $n_{INP}(T_k) = (cf)\left(n_{a>0.5\mu m}\right)^{(\alpha(273.16-T_k)+\beta)} \exp(\gamma(273.16 - T_k) + \delta)$<br><br>$n_{INP}(T_k)$ = INP per standard liter<br>$n_{a>0.5\mu m}$= particles cm$^{-3}$ |
| **Fluorescing biological aerosol particles (Tobo et al., 2013)** | $N_{IN} = \left(N_{FBAP>0.5\mu m}\right)^{(\alpha'(273.16-T)+\beta')} \exp(\gamma'(273.16 - T) + \delta')$<br><br>$N_{IN}$ = INP per standard liter<br>$N_{FBAP}$ = particles cm$^{-3}$ |
| **Niemand 2012 dust (using PALMS mineral data from Karl Froyd)** | $\sum_{j=1}^{n} N_{i,j} \approx \sum_{j=1}^{n} N_{tot,j} S_{ae,j} n_s(T) = n_s(T) \sum_{j=1}^{n} N_{tot,j} S_{ae,j}$ |

In order to compare these parameterized values with observations, an overall mean observed immersion $N_{INP}$ was calculated for each three-hour period based on all the available data from all the instruments. Immersion $N_{INP}$ was predicted using each

parameterization using mean WIBS, LAS, and PALMS data collected in the coincident 3-hour periods of time as the INP data. The observed and predicted immersion $N_{INP}$ are plotted again each other in Fig. 12.

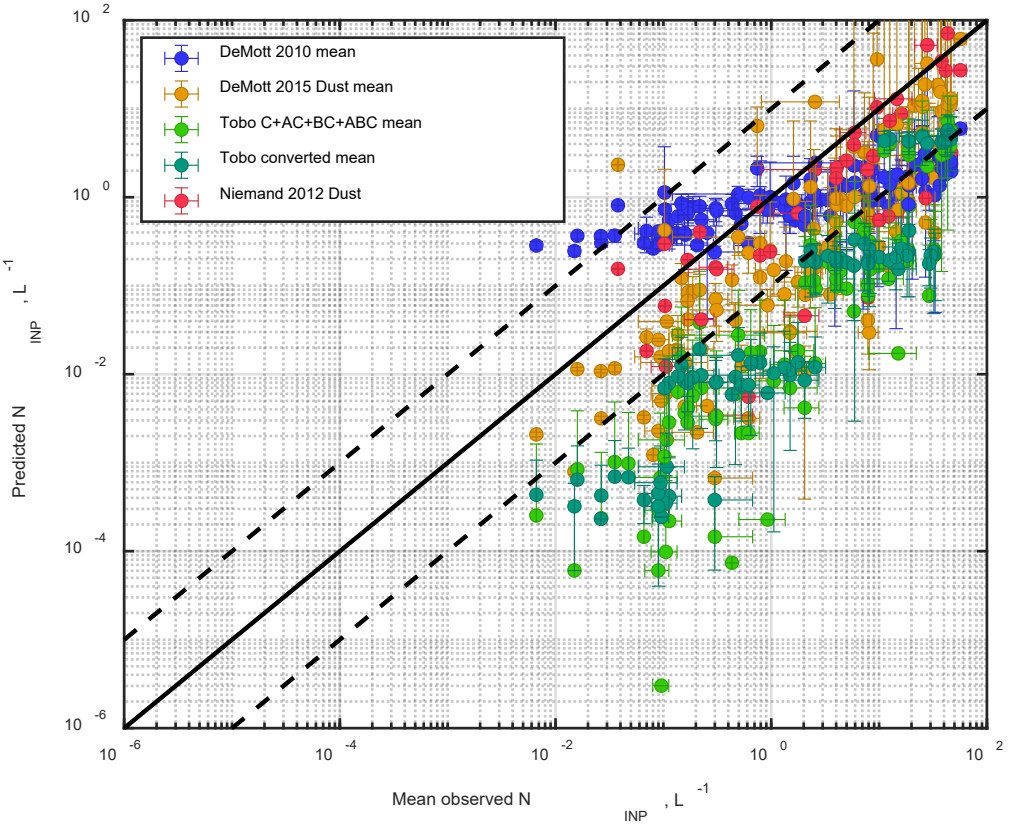


**Figure 12** Comparison of mean observed $N_{INP}$ and predicted $N_{INP}$ calculated from several parameterization schemes at the temperatures -30 °C, -25 °C, -20 °C, and -15 °C. Mean observed INP concentrations shown in this figure are averaged over three-hour periods. The dashed lines indicate differences of one order of magnitude between the mean observed $N_{INP}$ and predicted $N_{INP}$. Time series of the observation means and predicted $N_{INP}$ are shown in Fig. A3. Analysis of the agreement between the observations means and the predicted $N_{INP}$ is shown in Fig. A4.

Three of the four parameterizations replicate variation in observed INP well. The outlier is DeMott 2010, which appears to predict a relatively constant INP concentration despite substantial variations in the observed value. DeMott 2010 accurately predicts the

concentration of observed immersion INP (~1 $L^{-1}$) at -20 °C, but overpredicts observed $N_{INP}$ (~$10^{-1}$ $L^{-1}$) by approximately an order of magnitude at -15 °C, as shown in Fig.A3. This parameterization subsequently underpredicts the concentration of observed immersion INP at -25 °C and -30 °C by approximately one and two orders of magnitude, respectively. This suggests that the underlying assumption that all aerosols with diameter > 0.5 μm are capable of activating as INP is insufficient to represent the aerosols present during the campaign, and that an aerosol-aware parameterization is needed.

DeMott 2015, which is based on the assumed INP activity of mineral dust, more accurately predicts $N_{INP}$. However, actual mineral dust content in aerosols varied over the course of the project as observed by the PALMs instrument. The ratio of the size-binned mineral dust concentration (estimated from the PALMS mineral dust measurements and size distributions measured by the LAS) to the total size-binned aerosol particle concentration measured by the LAS is shown in Fig. A4. The percentage of mineral dust in the total size-binned aerosol concentration was elevated on several days, accounting for 9-29% of aerosol particles in the diameter range 0.4-0.9 μm on September 14, 5-10% of aerosol particles in the diameter range 0.5-0.8 μm on September 23, and 3-9% of aerosol particles in the diameter range 0.40-0.70 μm on September 26.

Unlike DeMott 2015, the Niemand 2012 parameterization incorporates measurements of mineral dust concentration and surface area collected during FIN-03. Niemand 2012 provided the most accurate predictions of INP concentration during FIN-03. A caveat is that using this strategy will only be possible where specialized

measurements of dust concentration are available. For FIN-03, both applications of the Tobo parameterizations consistently underpredicted $N_{INP}$, though both versions perform more adequately at -30 °C than at the three warmer temperatures used. Neither version of this parameterization was effective in predicting the observation means (0% match within a factor of two). These results are consistent with the fact that biological components of aerosols were not major contributors of INP during FIN-03.

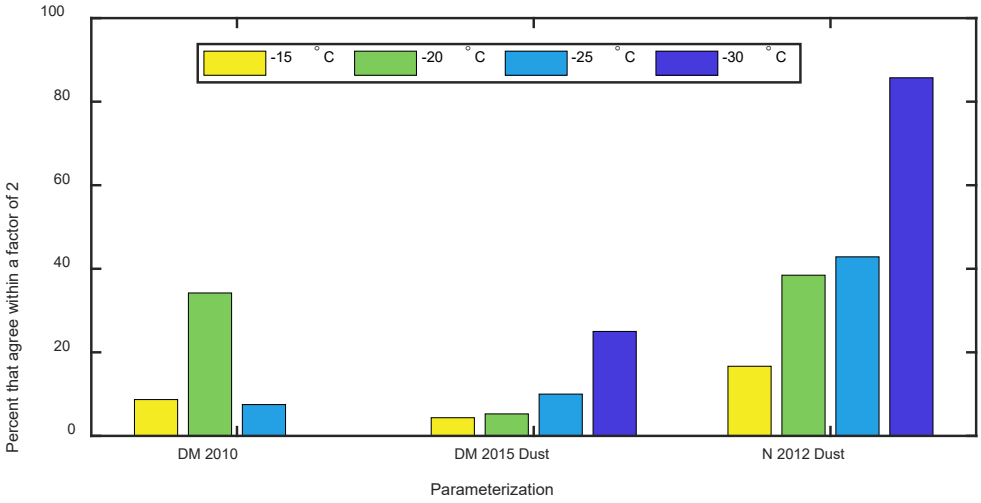


**Figure 13** Percent of time-matched observation mean and predicted immersion-mode $N_{INP}$ that agree within a factor of 2.

Next we consider the temperature dependence of agreement between observed and predicted $N_{INP}$. The percent of time in which observations and predictions show reasonably good agree (within a factor of 2 or better) were calculated for the three best-performing parameterizations at each of the four temperatures, as shown in Fig. 13. The Tobo parameterizations are not included due to the poor fit discussed above. DeMott 2010 performed the best at -20 °C, where 34% of the time-matched data points between

the observation mean and the predicted immersion $N_{INP}$ differed by a factor of two or less. $N_{INP}$ was overpredicted by the DeMott 2010 parameterization at -15 °C (resulting in 9% agreement within a factor of two) but underpredicted at -30 °C and -25 °C (resulting in 7.5% and 0% agreement within a factor of two, respectively). While this parameterization performed well at -20 °C, it failed to replicate the temperature dependence of the observation mean. The predicted $N_{INP}$ based on the DeMott 2015 performed slightly better at -25 °C (10% agreement within a factor of two) and noticeable better at -30 °C (25% agreement within a factor of two), but poorly at -20 °C and -15 °C (5% and 4% agreement within a factor of two, respectively). The predicted immersion $N_{INP}$ based on the Niemand 2012 dust parameterization outperformed the other parameterizations, with 17%, 38%, 43%, and 86% agreement within a factor of two at -30 °C, -25 °C, -20 °C, and -15 °C, respectively. Interestingly, the performance of the two dust parameterizations (DeMott 2015 and Niemand 2012) improved as temperature decreased.

## Deposition observations

While need for INP concentration measurements in water-subsaturated conditions was identified during FIN-02, a deposition mode intercomparison was not conducted during that campaign (DeMott et al., 2018). Deposition $N_{INP}$ measurements were carried out by three instruments during FIN-03, and these results are summarized in Fig. 14. The primary objective of the FIN-03 campaign was to intercompare immersion nucleation. During the sampling campaign, less emphasis was placed on deposition measurements, and consequently fewer data points are available for intercomparison. The sensitivity of deposition ice nucleation relative humidity is clear, as differences in deposition-mode $N_{INP}$ of nearly an order of magnitude are present at -30 °C, -25 °C, and -20 °C, and the difference between deposition $N_{INP}$ collected at 95% and 99% RH exceed one order of magnitude at -15 °C. Only a few data points are available for deposition $N_{INP}$ collected by the MIT-SPIN and the CSU-CFDC. Agreement between the MIT-SPIN and 99% RH FRIDGE deposition-mode $N_{INP}$ is observed at -30 °C, but the MIT-SPIN deposition $N_{INP}$ exceeds that measured by the FRIDGE (at 95% and 99% RH) and the CSU-CFDC (94.3-94.6% RH) at -25 °C and -20 °C. While the set relative humidity for deposition-mode MIT-SPIN $N_{INP}$ was approximately 96%, the relative humidity throughout the instrument may reach or exceed 100% for these same measurements, which may explain why one of the three data points agrees mostly closely with a FRIDGE measurement at 99% RH and the other two data points do not agree with any FRIDGE or CSU-CFDC data. The CSU-CFDC deposition-mode $N_{INP}$

were only collected at approximately -25 °C, and these three data points agree well with the mean FRIDGE deposition-mode $N_{INP}$ at -25 °C.

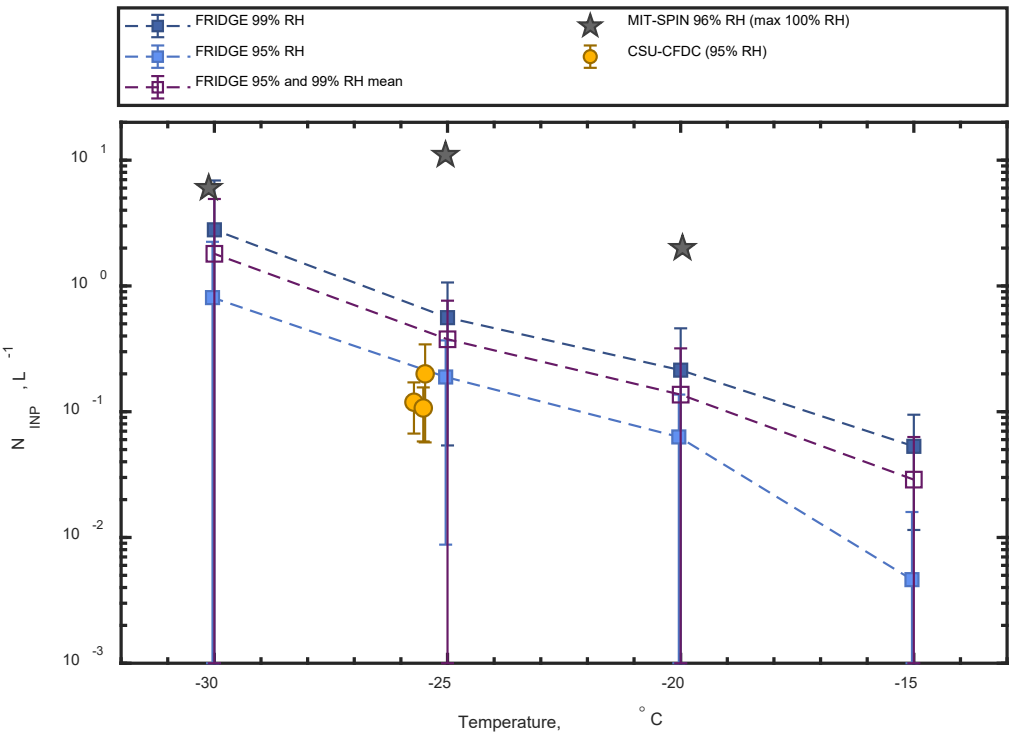


**Figure 14** Summary of deposition-mode $N_{INP}$ as a function of temperature, with RH values for each measurement given. FRIDGE data has been averaged for each temperature.

A time series of the deposition $N_{INP}$ measurements collected by the FRIDGE at -25 °C, -20 °C, and -15 °C during FIN-03 is shown in Fig. 15(a), 15(b), and 15(c), respectively. Deposition-mode $N_{INP}$ has been averaged over three-hour periods. Additionally, the FRIDGE immersion data has been included in this figure to allow for the comparison of immersion and deposition measurements. A few observations immediately stand out from this figure. As expected, immersion $N_{INP}$ nearly always

exceeds deposition-mode $N_{INP}$ when both measurements are collected by the FRIDGE within the same time period (or during adjacent time periods). It is also apparent that while $N_{INP}$ in both ice nucleation modes increases as temperature decreases, this effect is more pronounced in the immersion mode than in the deposition mode.

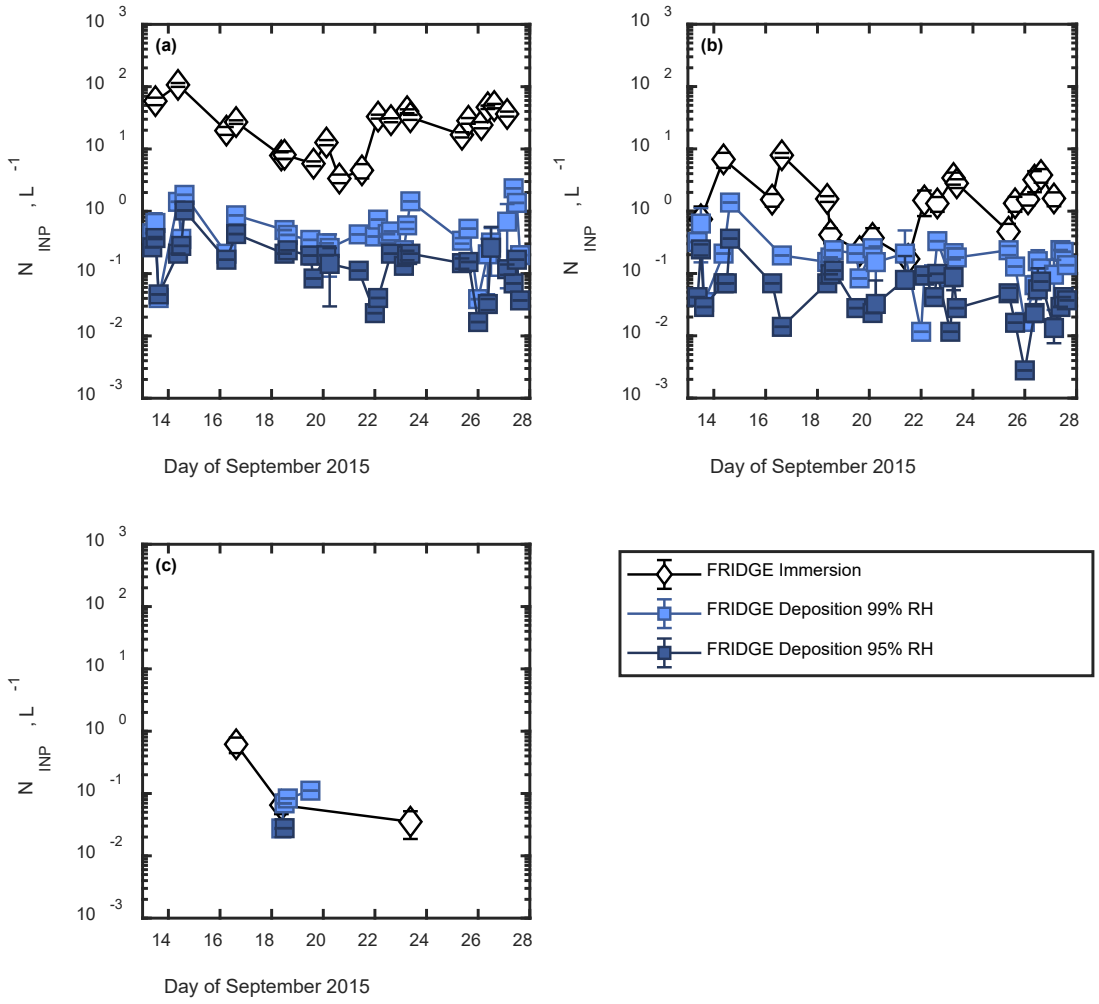


**Figure 15** Time series of immersion-mode and deposition-mode $N_{INP}$ measured by the FRIDGE at (a) -25 °C, (b) -20 °C, and (c) -15 °C.

FRIDGE $N_{INP}$ measured in the two modes differ by 0-2 orders of magnitude for most of the time-matched data points at -20 °C and by 1-3 orders of magnitude for most of the data points (which were collected during the same three-hour periods) at -25 °C. The difference between immersion and deposition-mode FRIDGE $N_{INP}$ also decreases to a factor of two to three during the period September 18-20 at -20 °C, though this short-lived closing of the gap is not observed at -25 °C. Overlap was observed for the few immersion and deposition INP concentrations measured by the FRIDGE at -15 °C.

The results from this study show that deposition-mode ice nucleation does contribute to the pool of INP in the atmosphere, and that it should not be neglected in atmospheric models. The ability of online ice nucleation instruments to measure $N_{INP}$ in the deposition mode has also been demonstrated. More work should be carried out on measurements of ice nucleating particles in the deposition mode.

## Summary and conclusions

FIN-03 was the first ice nucleation instrument intercomparison conducted in a field setting. For immersion nucleation, good agreement (usually within 1 order of magnitude) between the participating instruments was comparable to that encountered in the preceding FIN-02 laboratory intercomparison. Given the constant changes in the concentration, size distribution and composition of the ambient aerosol population inevitable with any field campaign, we consider this level of agreement to be a success. Environmental challenges included aerosols in a concentration range of 571±19 $cm^{-3}$ and

varying particle composition (with dominant fractions of sulfates/organics/nitrates, products of biomass burning, and mineral dust).

The immersion INP concentrations measured in FIN-03 spanned a little over five orders of magnitude ($10^{-3}$ to ~$10^{2}$ $L^{-1}$) over the temperature range -35 °C to -5 °C. Agreement within one order of magnitude in immersion $N_{INP}$ was generally observed between all ice nucleation instruments measuring immersion INP concentrations provided that measurement and sampling times were matched to within 3 hours. All larger deviations occurred in the temperature range -25 °C to -18 °C, with better agreement at warmer and colder temperatures.

Larger deviations between measurements were most often observed between the FRIDGE and CSU IS, and the NCSU-CS (and were somewhat worse when the comparison made with NCSU-CS data analyzed from samples collected with the impinger, rather than the filter). This may be due to the greater response in INP concentration due to changes in the mass concentration of several particle types (sulfates/organics/nitrates, products of biomass burning, and mineral dust) observed in measurements carried out by the FRIDGE and CSU-IS, than in measurements carried out by the NCSU-CS (collected by the impinger or the filter). The CSU-CFDC agreed within one order of magnitude with the FRIDGE, CSU-IS, and NCSU-CS for the majority of the time periods when data was collected for each pair of instruments. The best agreement within the study was observed between FRIDGE and CSU-IS measurements.

Two online systems (CSU-CFDC, MIT-SPIN) and three offline systems (FRIDGE, CSU-IS, NCSU-CS) were represented in FIN-03. Interesting, there does not appear to be a clear divide between the ability of online and offline systems to measure INP concentrations from the data collected in this study. In principle both types of instruments show excellent promise for future field studies.

Unfortunately, only one of the three instruments used for measuring deposition-mode $N_{INP}$, the FRIDGE, was successful in obtaining more than a few data points throughout the study. A clear increase in FRIDGE deposition INP concentrations with decreasing temperature was observed during FIN-03, as well as good separation between the immersion and deposition modes. The FRIDGE is operated differently when measuring immersion and deposition $N_{INP}$, which may account for its success in separating these two modes.

For the limited deposition INP measurements submitted from the CSU-CFDC data, there is good agreement with FRIDGE deposition $N_{INP}$ when comparing data points collected with the same temperature (-25 °C) and relative humidity (95% RH). Only one of the three deposition data points from the MIT-SPIN approaches the mean FRIDGE deposition $N_{INP}$ collected at the same temperature (-30 °C) and similar relative humidity (96% RH for the MIT-SPIN, and 99% RH for the FRIDGE). The difficulty in obtaining deposition INP measurements from the CSU-CFDC and the MIT-SPIN during FIN-03 may have facilitated improvements in the operation of these instruments. CSU-CFDC and the MIT-SPIN deposition data, which was initially collected in the deposition mode, was removed from the study due to difficulty establishing the proper relative humidity

range or problems related to particle counting. If deposition-mode $N_{INP}$ is shown to be atmospherically important, then it will be useful to solve these issues and enable future measurements.

For the immersion data, the ability of several parameterizations to predict the combined observations were conducted to see if there exists a parameterize which well presents the INP data collected at the mountaintop observatory. The widely used DeMott 2010 did not predict INP concentrations, remaining a flat function across the range of observed $N_{INP}$ values.

DeMott 2015 and Niemand 2012 correctly predicted 25% and 86% (respectively) of the observed INP concentrations at -30 °C within a factor of 2. These two parameterizations did not perform as well at warmer temperatures, however, accurately predicting 4-10% and 17-50% (respectively) of the observed INP concentrations over the temperature range -25 °C to -15 °C within a factor of 2.

While Niemand 2012 predicted the most values most aligned with observations, it relies of onsite mineral dust measurements which are not available in all studies. In the air masses sampled during FIN-03, mineral dust content was an apparent driver of the ice nucleating properties of available aerosol. In general, INP parameterizations which incorporate aerosol composition into the direct analysis or underlying assumptions will be more accurate.

Future work suggested by the results of FIN-03 includes a continuation field intercomparisons, ideally carried out in diverse environmental settings. Additional deposition-mode ice nucleation measurements are also needed in order to determine the

best manner of operation for separating the immersion and deposition modes, and to work towards convergence of deposition-mode $N_{INP}$ measured by ice nucleation instruments with different configurations. Continued measurements in both the immersion and deposition modes will also enable researchers to determine differences in operation between online and offline instruments in each mode, if consistent differences do in fact occur. A growing body of INP measurement research will also facilitate our understanding of the fundamental nature of ice nucleation and the characteristics of ice nucleating particles, which are necessary for the development of accurate atmospheric models.

# CHAPTER V

# GLASSY AND VISCOUS ORGANICS AS ICE-NUCLEATING PARTICLES

## Background

The phase of an aerosol particle can be characterized by its viscosity and glass transition temperature. Viscosity is a measurement of resistance to deformation. The phase of a substance can be classified according to its viscosity, $\eta$: liquids typically have $\eta < 10^3\ poise$, semi-solids have viscosity $10^3\ poise < \eta < 10^{13}\ poise$, and a common definition sets the viscosity for amorphous solids for (such as glass) sets $\eta > 10^{13}\ poise$ (Debenedetti & Stillinger, 2001; Shiraiwa, Ammann, Koop, & Poschl, 2011). Viscosity increases as temperature decreases, which may have important consequences for particle phase in the upper troposphere and subsequently, heterogeneous ice nucleation (Collier & Brooks, 2016).

The glass transition temperature $T_g$, defined simply as the temperature at which, upon cooling, a liquid undergoes a transition to a glass (also known as vitrification), can be used to determine how similar a substance is to a glass given its current temperature. There are several operational definitions for the glass transition temperature which may lead to disagreements between results for a single substance. The first definition, as previously mentioned, is the temperature at which the viscosity of a liquid (through supercooling) reaches $10^{13}\ poise$; however, this definition is flawed in that it is possible for the viscosity at the glass transition to be orders of magnitude lower than this value (Bair, 2019). The second definition is concerned with the change in behavior of a liquid

as it is cooled below a certain temperature. If a liquid is cooled below its freezing point quickly enough that crystallization may be avoided, a plot showing the volume (or enthalpy) of the liquid as a function of temperature will consist of two lines that intersect. These lines correspond with the liquid state, which exhibits super-Arrhenius relaxation, and the vitreous or glassy state, which exhibits Arrhenius relaxation. The temperature at which these two curves intersect is the liquid's glass transition temperature (Chandler & Garrahan, 2010; Hudson & Mandadapu, 2018; Keys, Garrahan, & Chandler, 2013). This temperature is approximately equal to two-thirds the temperature at which the frozen sample would melt (if it had frozen, rather than vitrified). The third definition for glass transition temperature is the temperature at which the characteristic molecular relaxation time for the supercooled liquid increases to $\geq$ 100 s. It has been proposed that some liquid aerosol particles may vitrify at temperatures characteristic of the upper troposphere (Cappa & Wilson, 2011; Vaden, Song, Zaveri, Imre, & Zelenyuk, 2010; Virtanen et al., 2010).

Measures of particle phase, particularly viscosity and proximity to the vitreous state, may have implications for contact mode ice nucleation, which follows the approach of an aerosol that acts as an INP to the air-droplet interface. Contact mode ice nucleation is particularly interesting because it has been observed to occur at higher temperatures than immersion mode ice nucleation for the same particle (Diehl, Matthias-Maser, Jaenicke, & Mitra, 2002; Fornea, Brooks, Dooley, & Saha, 2009; Z. Levin & Yankofsky, 1983; Pitter & Pruppacher, 2007; Pruppacher & Klett, 2010; Shaw, Durant, & Mi, 2005; Vali, 1996) with differences between the onset temperature of the two

mechanisms of approximately 4-5 °C (Durant & Shaw, 2005; Shaw et al., 2005). Potential explanations for the higher onset temperatures observed for contact nucleation than immersion nucleation include decreases in the free energy barrier between water and ice (Fukuta, 1975), as well as at the three-phase contact line (Djikaev & Ruckenstein, 2008).

The relationship between contact mode ice nucleation, viscosity, and vitrificaiton arises because of the interesting site on which contact mode ice nucleation occurs: the surface of the droplet, at the air-water interface. Enhanced nucleation has been observed at droplet surfaces (Djikaev, Tabazadeh, Hamill, & Reiss, 2002; Tabazadeh, Djikaev, & Reiss, 2002), possibly due to the greater freedom of motion of liquid molecules at the surface in contrast with the bulk (Chushak & Bartell, 1999) and a decrease in the free energy barrier (Shaw et al., 2005). Viscous or glassy aerosol particles may provide flexible surfaces which promote contact mode ice nucleation.

Highly viscous aerosol particles have been shown to limit the rate of ice nucleation and the inhibit the growth of ice crystals by decreasing the rate of diffusion (Murray, 2008). If an ordered, crystalline surface is required for ice nucleation, it follows that liquid or glassy aerosol particles would be unlikely to initate the freezing of water droplets with which they are in contact or the deposition of water vapor into the ice (Zobrist et al., 2008), though it has been shown that a small fraction of glassy aerosol particles may act as INP, possibly due to the inclusion of solutes or other impurities on their surface that function as active sites (Murray et al., 2010). Additionally, the ability

of liquid or semi-solid particles to activate as contact mode INP has been observed (Niehaus & Cantrell, 2015).

It is possible that the composition of glassy aerosol particles play as large as role as viscosity or proximity to the glass phase in determining ability to activate as INP. Several studies have shown that glassy aerosols composed of simple sugars and acids are efficient INP (Baustian et al., 2013; Murray et al., 2010). In contrast, (Jensen et al., 2018) suggests that glassy organic aerosol particles in the tropospheric tropopause are poor INP. These glassy particles likely consist of compounds with the approximate composition of secondary organic aerosols (SOA). Additionally, the glass transition temperatures of organic compounds can change via chemical reactions in the atmosphere.. Oxidation and oligomerization reactions increase the ratio of oxygen to carbon in aerosol particles, which results in an increase in glass transition temperature, and therefore a transition to a glassy state through a greater portion of the troposphere (Koop et al., 2011).

The intention of this portion of my dissertation is to serve as a record for the work completed so far in this study, as well as plans for its continuation following my departure from Texas A&M University.

## Methods

### Viscosity measurements

A series of viscosity measurements over a range of temperatures (approximately 233-298 K), for several binary aqueous solutions of varying concentration and three eutonic aqueous solutions, were carried out by myself and an undergraduate research assistant, Maria Zamarron. The experimental method for this set of measurements utilizes three Ubbelohde viscometers (Canon 3B 9721-N83, 4C 9721-N89, 5 9721-N95) to cover a range of viscosities. Ubbelodhe viscometers are used to determine the time required for the meniscus of a solution to fall from one mark on the viscometer to another mark a few centimeters below; the "fall time" is multiplied by the viscometer constant and the solution density in order to calculate its viscosity. For each measurement, the viscometer was charged with the appropriate amount of solution (depending on the viscometer size), and a set of ten replicate measurements were taken at room temperature (approximately 298 K). Then, the solution was cooled using a Neslab cooling bath filled with Syltherm to 283 K, 273 K, 263 K, 253 K, 243 K, and 233 K, until the freezing temperature of the solution was determined (which prohibited further measurements). No measurements below 233 K were achieved due to this limit.

Binary aqueous solutions of citric acid, sucrose, and maltose were prepared, in mass concentrations of 40%, 50%, and 65%, by dissolving the appropriate masses of solute in water. Glyoxal and methylglyoxal, sold by the manufacturer with mass concentration 40%, were reduced at 310 K in order to increase the concentration to 50% and 65%. Eutonic aqueous solutions were prepared by first preparing saturated solutions

of citric acid, sucrose, and glyoxal, then adding ammonium sulfate to the saturation point, and adding additional organic solute to maintain the saturation of the organic component.

## Glass transition temperature measurements

Glass transition temperature was determined using interdigitated electrodes with broadband dielectric spectroscopy (IDE-BDS), as carried out in a recent study (Y. Zhang et al., 2018) and shown in Fig. 16(a). A more detailed view of an IDE is shown in Fig. 16(b).

Briefly, the surface of an interdigitated electrode (IDE, NIB003744, MS-01/60 and MS-05/60, NETZSCH Instrument North America) is covered with a thin layer of sample and placed into a cooling/heating chamber (Netzsch DEA Furnace). The chamber is flushed with nitrogen gas prior to sampling in order to control the relative humidity during sampling. The ends of the electrode are connected to the broadband dielectric spectroscopy instrument (NETZSCH Inc., DEA 288 model). The BDS instrument applies the IDE electrodes with a periodic signal, with a signal frequency that varies over the range $10^{-3} - 10^{6}\ Hz$. The cooling/ heating chamber uses liquid nitrogen to decrease the temperature of the sample at a rate of 5 K $min^{-1}$.

As the sample is cooled over the approximate range 300 K to 125 K, its impedance is measured every twelve seconds as a function of the applied frequency. This impedance measurement is used to determine the capacitance of the sample.

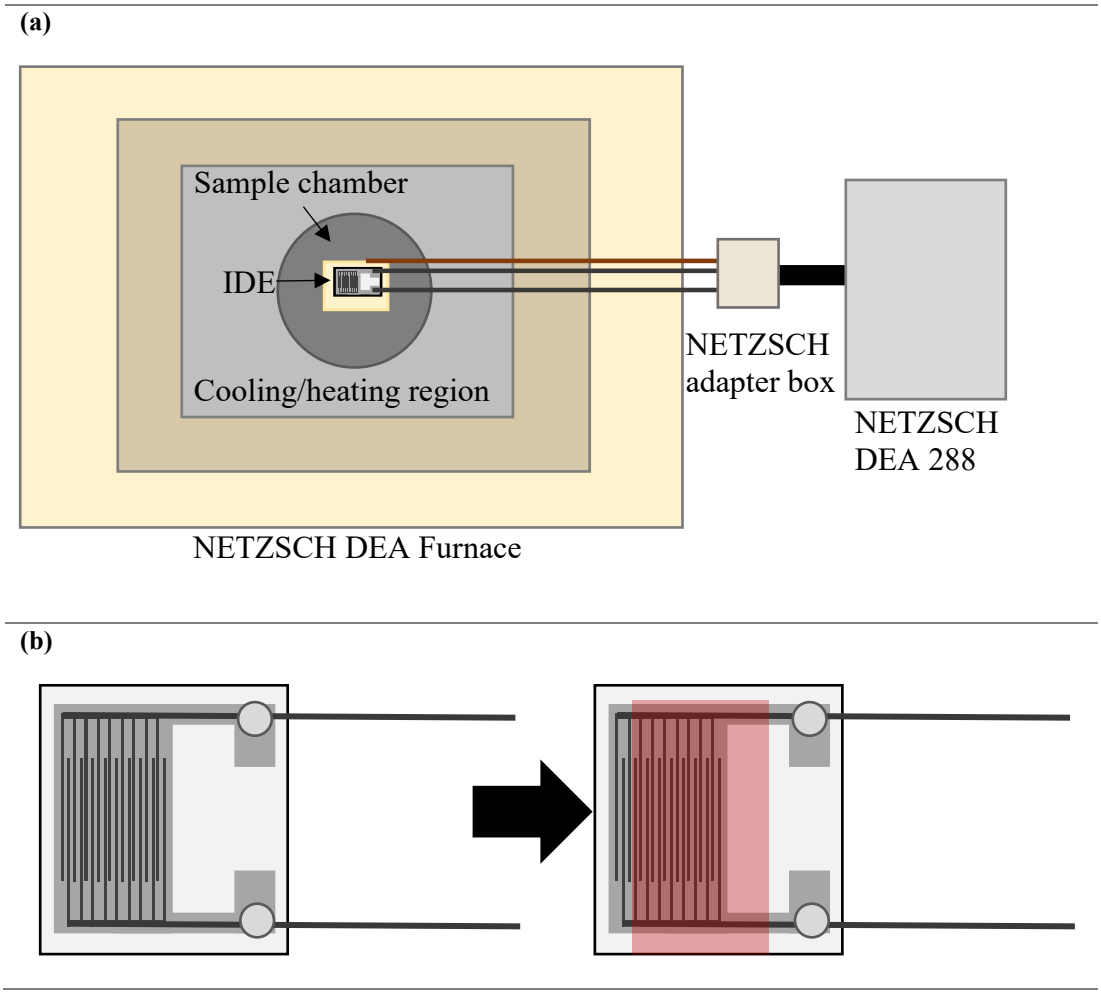


**Figure 16** (a) Experimental setup for the IDE-BDS measurements. (b) The sample is loaded onto the IDE by spreading a thin layer across the interdigitated region of the electrode, as shown in red.

The permittivity $\varepsilon(\omega)$ of a sufficiently thick sample (Chen, Sepulveda, Ediger, & Richert, 2012) is a function of the capacitance of an IDE loaded with sample $C_{loaded}$, the capacitance of an empty IDE $C_{empty}$, and the geometric capacitance of the IDE in the absence of the subtrate $C_{geometric}$, as shown in Eq. 6.

$$\varepsilon(\omega) = 1 + \frac{C_{loaded} - C_{empty}}{C_{geometric}} \quad \text{Eq. 6}$$

The sample permittivity is a complex function that can be broken down into its real and imaginary parts, $\varepsilon'(\omega)$ and $\varepsilon''(\omega)$ respectively, as shown in Eq. 7. The latter is also referred to as the loss factor of the sample.

$$\varepsilon(\omega) = \varepsilon'(\omega) - i\varepsilon''(\omega) \quad \text{Eq. 7}$$

The real ($\varepsilon'(\omega)$) and imaginary ($\varepsilon''(\omega)$) parts of the sample's permittivity are described using the Havriliak–Negami equation (Chen et al., 2012), as shown in Eq. 8(a) and 8(b)).

$$\varepsilon'(\omega) = \varepsilon_\infty + \Delta\varepsilon \left(1 + 2(\omega\tau)^\alpha \cos\left(\frac{\pi\alpha}{2}\right) + 2(\omega\tau)^{2\alpha}\right)^{-\beta/2} \cos(\beta\varphi) \quad \text{Eq. 8(a)}$$

$$\varepsilon''(\omega) = \Delta\varepsilon \left(1 + 2(\omega\tau)^\alpha \cos\left(\frac{\pi\alpha}{2}\right) + 2(\omega\tau)^{2\alpha}\right)^{-\beta/2} \sin(\beta\varphi) \quad \text{Eq. 8(b)}$$

Where $\varepsilon_\infty$ is the permittivity of the high frequency limit, $\alpha$ and $\beta$ are fitting parameters, $\varphi$ is a parameter common to both equations $\left(\varphi = \tan^{-1}\left(\frac{(\omega\tau)^\alpha \sin\left(\frac{\pi\alpha}{2}\right)}{1+(\omega\tau)^\alpha \cos\left(\frac{\pi\alpha}{2}\right)}\right)\right)$, and $\tau$ is the characteristic relaxation time of the sample (at a given temperature) found by fitting the experimental data and adusting the fitting parameters. The characteristic relaxation time $\tau$ (at each tempearature) is determined by plotting the loss factor $\varepsilon''(\omega)$

as a function of frequency $\omega$ and adjusting the fitting parameters $\alpha$ and $\beta$, then solving for $\tau$ using the Levenberg-Marquardt theorem algorithm for finding the nonlinear least squares fit to the data (Gavin, 2019). An example of this procedure is shown for IEPOX in Fig. 17(a), where loss factor $\varepsilon''(\omega)$ is shown for seven temperatures over which data was collected. Once $\tau$ has been determined over a wide temperature range, plotting $\log_{10}(\tau)$ as a function of $1000/T$ results in a roughly-linear function, as shown in Fig. 17(b).

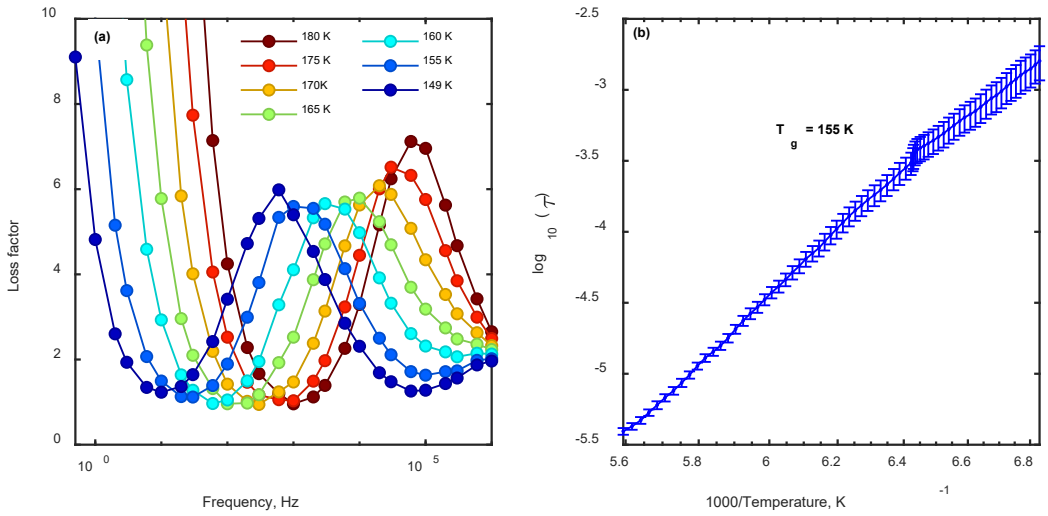


**Figure 17** Exemplar data for the determination of $\boldsymbol{T_g}$ for IEPOX. (a) The sample's loss factor $\boldsymbol{\varepsilon''(\omega)}$ was plotted as a function of frequency (shown here for only seven temperatures for visual clarity). A non-linear least squares fit was applied to the loss factor across a wide temperature range in order to determine the characteristic relaxation time of the sample at each temperature. (b) The logarithm of the characteristic relaxation time of the sample was plotted against $\boldsymbol{1000/T}$ in order to determine the glass transition temperature.

As the temperature decreases and the sample's phase transitions from liquid to a glass, it exhibitis super-Arrhenius relaxation. The temperature at which this transition occurs is visually apparent as the temperature at which the slope of the $\log_{10}(\tau)$ vs. $1000/T$ abruptly decreases. Thus, the glass transition temperature $T_g$ of the sample is determined.

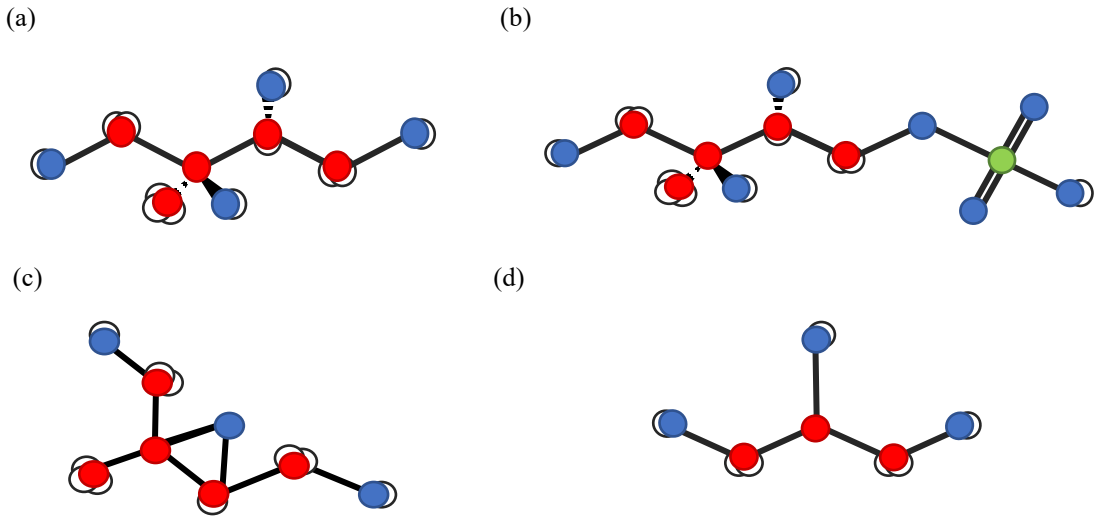


**Figure 18** The chemical structures of (a) 2-methyl tetrol, (b) 2-methyl tetrol sulfate, (c) IEPOX, and (d) glycerol are shown. The colors of carbon, oxygen, hydrogen, and sulfur atoms are red, blue, white, and green, respectively.

This procedure was carried out in triplicate for several pure samples of SOA compounds, IEPOX (isoprene-derived epoxydiols), 2-methyltetrol, 2-methyltetrol sulfate, as well as a series of mixtures (in mass ratios of 3:1, 1:1, and 1:3) of IEPOX and 2-methyl tetrol sulfate. All SOA samples were provided by Jason Surrat at the University of North Carolina. The glass transition temperature of glycerol was also determined to compare the results of this study with those of previous studies, using a

standard compound. The chemical structures of each of these compounds is shown in Fig. 18.

Additional measurements were attempted for methacrolein, methylglyoxal, maltose monohydrate, levoglucosan, squalane, squalene, oxalic acid, adipic acid, and sebacic acid. However, the dipole moment for each of these samples was insufficient for data collection through IDE-BDS.

## Contact ice nucleation measurements

The experimental setup for ice nucleation measurements is shown in Fig. 19. Measurements of ice nucleation in the contact mode will be carried out in the future. The experimental method will be briefly summarized here.

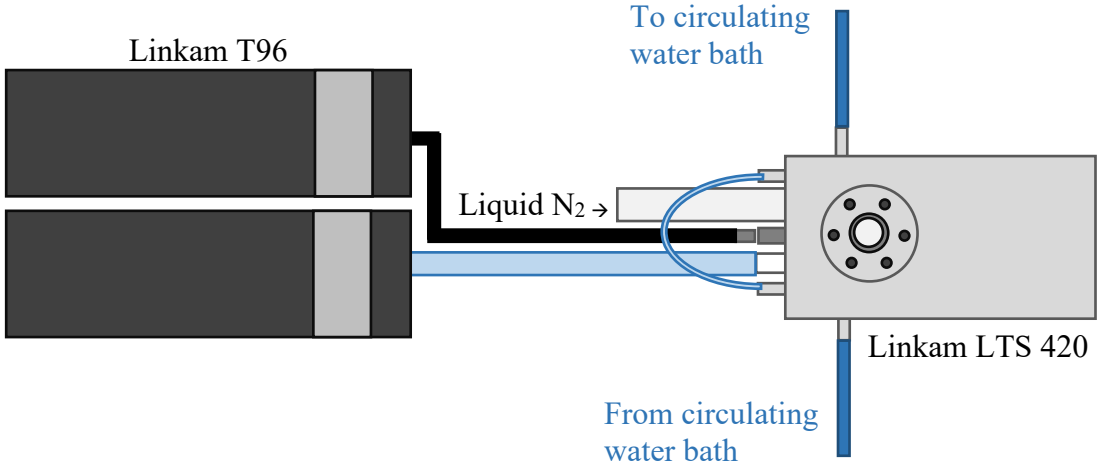


**Figure 19** Experimental setup for ice nucleation measurements.

A micropipette will be used to place a 2.5 µL droplet of HPLC water on a pre-silanized slide. A 1 µL droplet of the sample will be placed in contact with the surface

of the droplet from the side, and care will be taken to not distort the shape of the water droplet. The slide will then be placed in the stage's slide holder. The stage will be sealed with the sample inside. Droplet freezing is achieved using liquid nitrogen through an LTS 420 cooling stage with circulating water, and T96 System Controller operated via LINK software (all from Linkam Scientific Instruments). A temperature profile is set to cool the stage from 298 K to approximately 130 K at a rate of 1 K min-1, followed by warming to 298 K. This process is repeated several times over the course of 18-24 hours. A Canon EOS 5D Mark IV camera equipped with a Canon Macro Lens EF 100mm f/2.8L is to take photos through the viewing window on the cooling stage every six seconds, resulting in a new image for every 0.1 K temperature decrease.

The images collected during the freezing experiments will be analyzed in order to determine the temperature of ice nucleation onset. The onset of ice nucleation (freezing) is characterized by a wave of motion through the water droplet, following by a sudden change in the brightness and opacity of the water droplet.

## Results and discussion

### Viscosity measurements

The results of the viscosity measurements are shown in Fig. 20. Although the viscosities of our solutions cover a wide range, all but one fall within the "liquid regime", with $\eta < 10^3\ poise$, for all temperatures. The 65 wt% glyoxal solution reaches the "semi-solid regime" for $T \leq 253\ K$. Interestingly, the rate at which solution viscosity increases as temperature decrease is different for each solute. This may be due to the fact that two of the five solutions, glyoxal and methylglyoxal, form dimers in solution (Krizner, De Haan, & Kua, 2009; Whipple, 1970), a behavior that differentiates these two from the other samples included in the viscosity study.

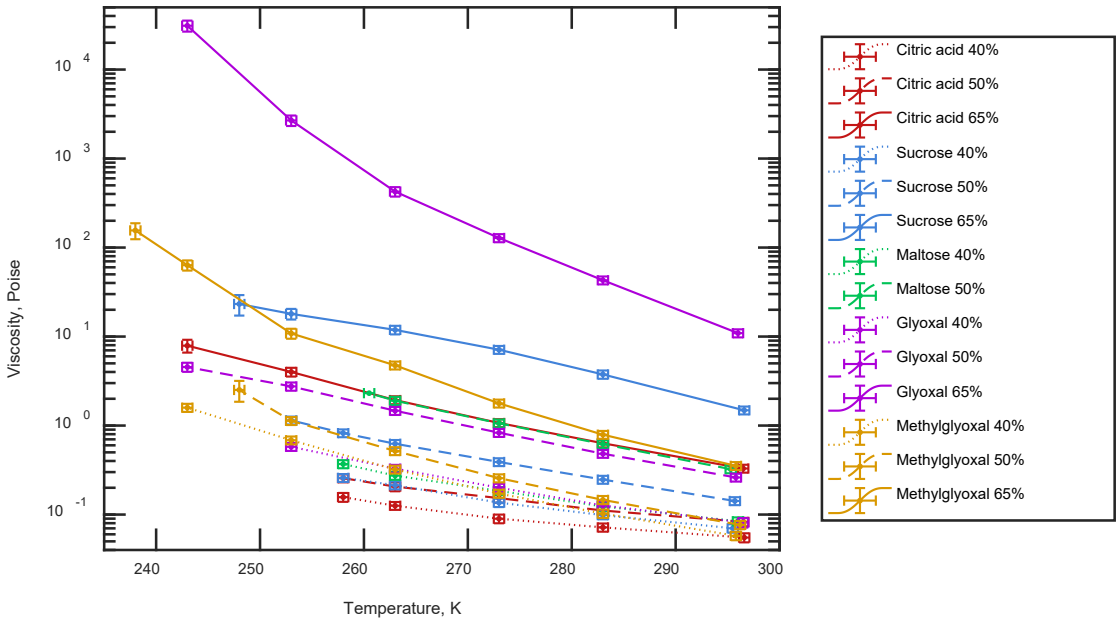


**Figure 20** Viscosity measurements were carried out for aqueous solutions of organic compounds with varying concentration (weight percent).

Viscosity measurements for aqueous solutions containing ammonium sulfate and sucrose, citric acid, and glyoxal are shown in Fig. 21(a), 21(b), and 21(c) respectively. The viscosity of the eutonic solutions exceeded that of the saturated solutions due to the greater amount of dissolved solute. This may in turn lead to an improvement in the efficiency of ice nucleation, though this data had not been collected at this time.

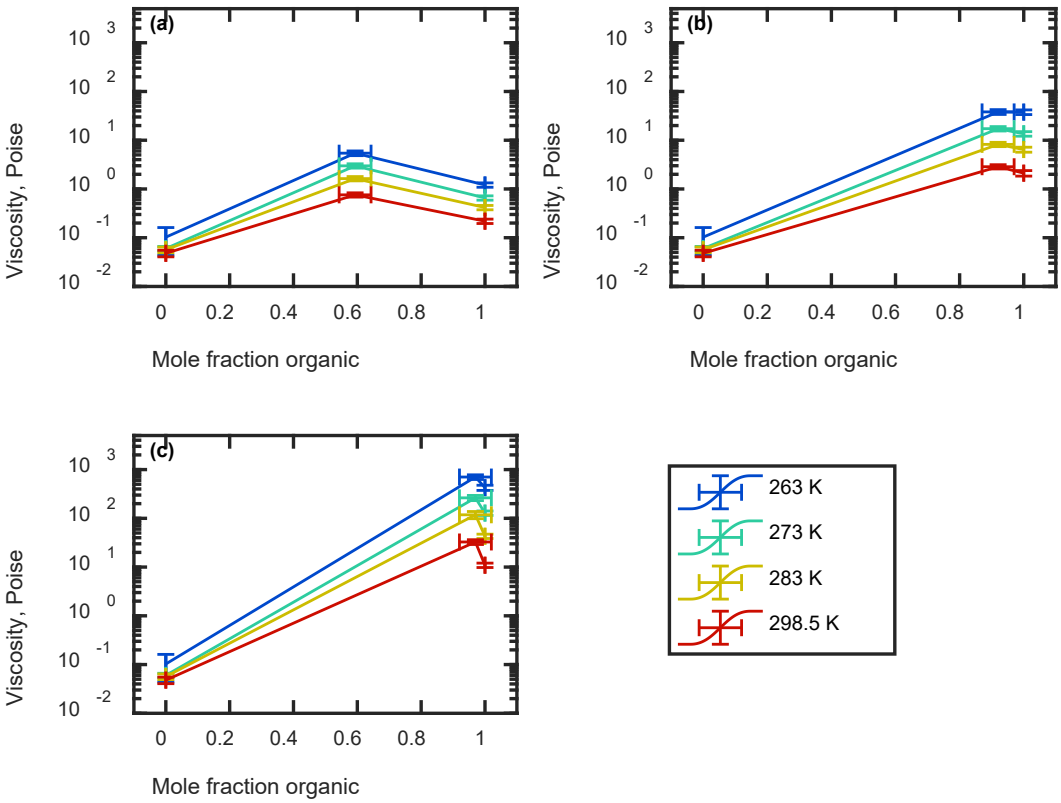


**Figure 21** The viscosity of saturated and eutonic solutions are shown for (a) ammonium sulfate and sucrose, (b) ammonium sulfate and citric acid, and (c) ammonium sulfate and glyoxal.

Glass transition temperature measurements

The glass transition temperature was determined for each of the four organic compounds (glycerol, 2-methyl tetrol, 2-metyl tetrol sulfate, and IEPOX) in triplicate. The results from this procedure are shown in Fig. 22.

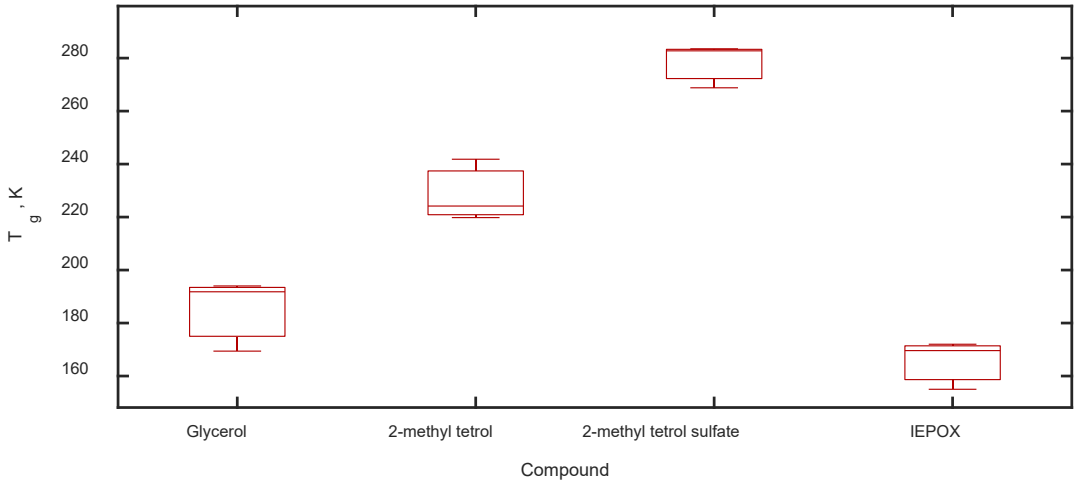


**Figure 22** The glass transition temperature $T_g$ was determined from triplicate measurements of each of the pure organic compounds.

The glass transition temperatures of these four compounds agree well with literature values from previous studies. The glass transition temperature of glycerol has previously been determined to fall within the range 190-196 K (Amann-Winkel et al., 2013; Chen, Sepulveda, Ediger, & Richert, 2012; Lienhard, Zobrist, Zuend, Krieger, & Peter, 2012; Zhang et al., 2018; Zondervan, Kulzer, Berkhout, & Orrit, 2007). In a recent study, the glass transition temperatures of several compounds were using the same experimental technique as the current study, and employing several cooling rates (Yue Zhang et al., 2019). For a cooling rate of 5 K $min^{-1}$, the glass transition temperatures of

2-methyl tetrol, 2-methyl tetrol sulfate, and IEPOX were determined by Zhang et al., 2019 to be 230±2 K, 276±15 K, and 166±2 K respectively. These results demonstrate that the IDE-BDS technique and subsequent analysis were successful in accurately determining the glass transition temperature of the samples. It should be noted that some variability was present in the results in the current study, as shown in the spread of $T_g$ values for each compound.

Mixtures of 2-methyl tetrol sulfate and IEPOX with mass ratios of 1:3, 1:1, and 3:1 were prepared, and the glass transition temperatures of the 3:1 and 1:1 mixtures were determined, as shown in Fig. 23. Although data was collected for the 1:3 mixture, analysis showed that the IDE used to collect this data was damaged, and therefore the glass transition temperature of this mixture could not be determined.

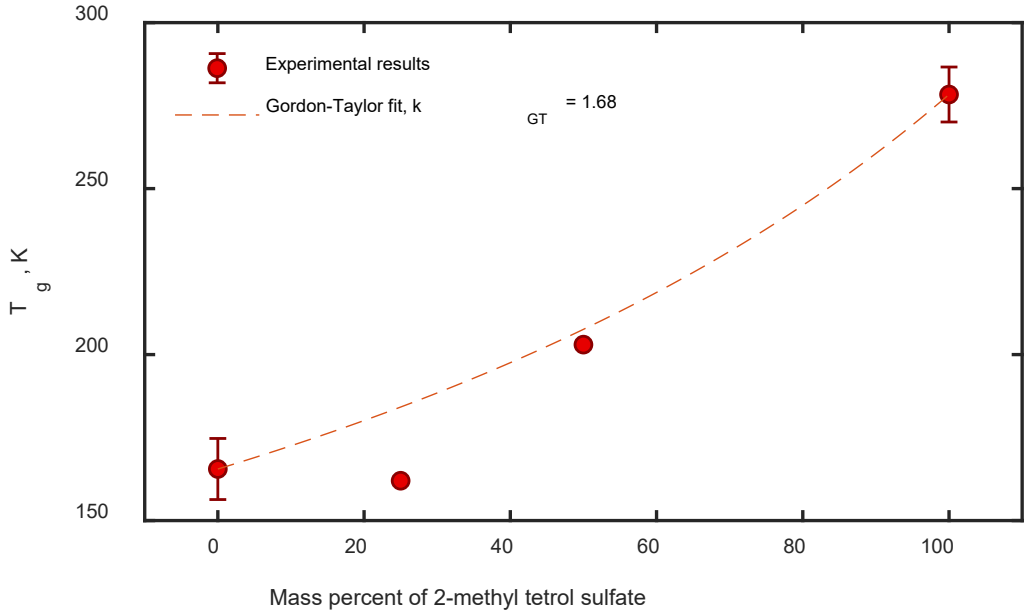


**Figure 23** Glass transition temperature results for the 2-MTOS and IEPOX mixture series. $T_{g,mixture}$ was predicted for this binary system using the Gordon-Taylor equation (Eq. 9) and the Simha-Boyer rule (Eq. 10).

The glass transition temperature of a binary mixture can be predicted using the Gordon-Taylor equation, as shown in Eq. 9:

$$T_{g,mixture} = \frac{(1 - f_a)T_{g,B} + \frac{1}{k_{GT}} f_a T_{g,a}}{(1 - f_a) + \frac{1}{k_{GT}} f_a} \quad \text{Eq. 9}$$

Where $f_a$ is the mass mixing ratio of component $a$ (in this case, 2-methyl tetrol sulfate), $T_{g,a}$ and $T_{g,B}$ are the glass transition temperatures of components $a$ and $b$ (2-methyl tetrol sulfate and IEPOX respectively), and $k_{GT}$ is the Gordon-Taylor constant. This constant is unique to the components of the mixture, and is typically determined by fitting the Gordon-Taylor equation to empirical data for the mixture being studied. In lieu of an adequate number of data points used for fitting Eq. 9., this constant can be approximated using the Simha-Boyer rule (Simha & Boyer, 1962), as shown in Eq. 10.

$$k_{GT} = \frac{(T_{g,a})(\rho_a)}{(T_{g,b})(\rho_b)} \quad \text{Eq. 10}$$

Where $\rho_a$ and $\rho_b$ are the densities of component $a$ (2-methyl tetrol sulfate) and component $b$ (IEPOX) respectively. The small quantities of each sample prohibited the determination of their densities, so the assumption that their densities were approximately equal was used for estimating $k_{GT} = 1.68$. While the glass transition temperature of the 1:1 2-methyl tetrol sulfate and IEPOX mixture is close to the predicted value, the same cannot be said for the 3:1 mixture. Additonal replicates may be needed to reach convergence between theory and experimental results. Alternatively, it is possible that the approximate Taylor-Gordon constant $k_{GT}$ is not accurate, which

would explain the discrepancy between the predicted and measured $T_{g,mixture}$ for this sample.

The IDE-BDS procedure was also used to measure the glass transition temperature of other samples (Table 6), as well as three series of binary mixtures of 2-methyl tetrol, 3-methyl tetrol sulfate, and IEPOX (Figure 24). This data was not collected in triplicate due to time constraints and small amounts of sample.

**Table 6** Additional $\boldsymbol{T_g}$ results for samples and mixtures. The letters "CNBD" indicate that results could not be determined from the data for the specified sample. The word "failed" indicates that the sample failed preliminary tests for determination of $\boldsymbol{T_g}$ through IDE-BDS.

| Sample | $\boldsymbol{T_g}$, K |
|---|---|
| Glyoxal (40% in aqueous solution) | 152.5±0.7 |
| 3-methyltetrol OS | 195.9±1.2 |
| Tetrol OS (68.2% mixed with ammonium sulfate) | CNBD |
| Mixture 1 (1:1 2-methyltetrol and 3-methyltetrol OS) | 251.7±0.7 |
| Mixture 2 (1:4 2-methyltetrol and 3-methyltetrol OS) | 255.0±0.3 |
| Mixture 3 (2:3 2-methyltetrol and 3-methyltetrol OS) | 222.9±0.5 |
| Mixture 4 (3:2 2-methyltetrol and 3-methyltetrol OS) | 244.6±0.7 |
| Mixture 5 (4:1 2-methyltetrol and 3-methyltetrol OS) | 228.6±0.02 |
| Mixture 6 (3:2 3-methyltetrol OS and IEPOX) | 206.2±0.4 |
| Mixture 7 (1:4 3-methyltetrol OS and IEPOX) | 209.0±0.5 |
| Mixture 8 (2:3 3-methyltetrol OS and IEPOX) | 222.1±0.6 |
| Mixture 9 (4:1 3-methyltetrol OS and IEPOX) | 204.5±0.3 |
| Mixture 10 (2:3 2-methyltetrol and 2-methyltetrol OS) | 203.7±0.1 |
| Mixture 11 (1:4 2-methyltetrol and 2-methyltetrol OS) | 203.1±0.2 |
| Mixture 12 (4:1 2-methyltetrol and 2-methyltetrol OS) | CNBD |
| Mixture 13 (3:2 2-methyltetrol and 2-methyltetrol OS) | CNBD |
| Methacrolein | failed |
| Methylglyoxal (40% aqueous solution) | failed |
| Maltose monohydrate | failed |
| Levoglucosan | failed |
| Squalane | failed |
| Squalene | failed |
| Oxalic acid | failed |
| Adipic acid | failed |
| Sebacic acid | failed |

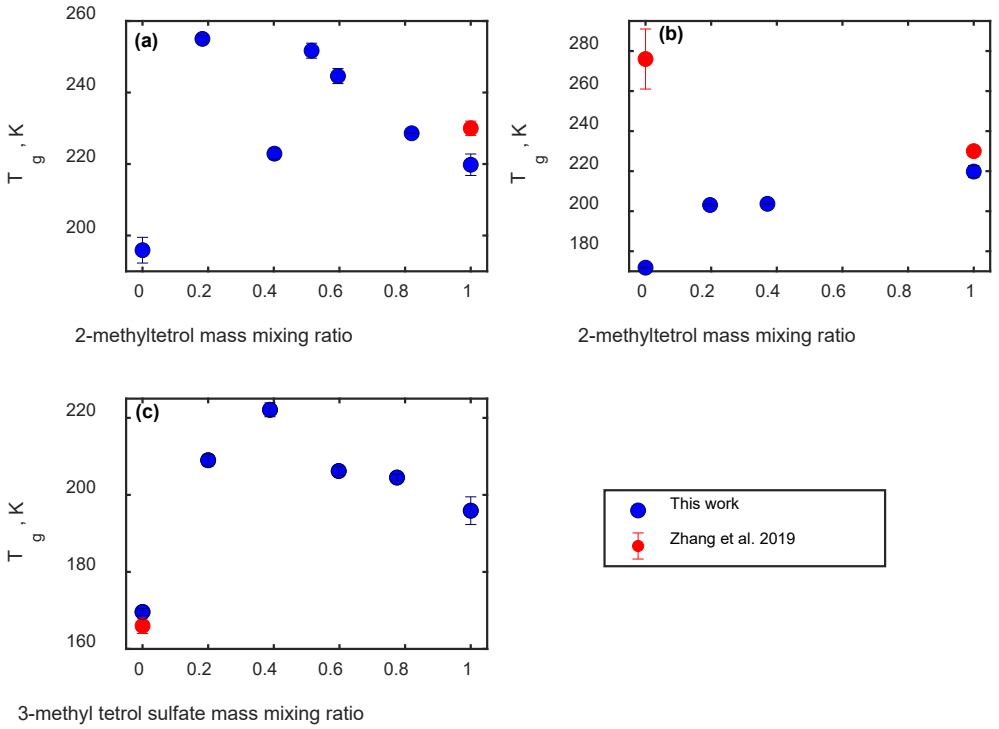


**Figure 24** Glass transition temperature results for binary mixtures of (a) 2-methyl tetrol and 3-methyl tetrol sulfate, (b) 2-methyl tetrol and 2-methyl tetrol sulfate, and (c) 3-methyl tetrol sulfate and IEPOX.

## Summary

This study is not yet complete, which is unfortunate due to the fact that I will leave Texas A&M soon. This portion of my dissertation is intended as a record of the work that has been completed so far.

Future work includes additional glass transition temperature measurements via IDE-BDS on the mixtures of the SOA compounds provided by Jason Surrat at the University of North Carolina. Additionally, we have discussed the possibility of studying the glass transition temperatures of organic/inorganic mixtures. The $T_g$ results for the pure compounds and mixtures, as well as the completed viscosity measurements for binary aqueous solutions and eutonic aqueous solutions, would then be combined with contact-mode ice nucleation measurements for each sample in order to determine the effects of viscosity and glass transition temperature on ice nucleation. Considering the results of Jensen 2018, I suspect that the sugar and citric acid solutions will exhibit more effective ice nucleation than the SOA compounds, and that ice nucleation will be enhanced for the solutions with higher concentration. However, previous studies (as discussed in the Background section) have yielded conflicting results about the effects of viscosity, glass transition temperature, and composition on the efficiency of organic compounds as INP. It will be interesting to see how the ice nucleation portion of this study develops.

# CHAPTER VI

# CONCLUSIONS

I have been given the opportunity to study many subjects related to aerosols and atmospheric science during my time at Texas A&M University. While these topics are not all represented in this dissertation, I would like to summarize them here, as well as the results from the three studies included in this dissertation. Finally, I have few closing remarks for my time as a graduate student.

I studied, designed experiments, and collected data related to warm cloud properties and cloud condensation nuclei during my first few years in the lab of Dr. Sarah Brooks. I participated in numerous lab experiments during this time, including the collection of aerosol data during five mesocosm experiments employing marine aerosol reference tanks (MART). I also participated in one of the cruises in the North Atlantic Aerosols and Marine Ecosystems Study (NAAMES) campaign for collecting aerosol, meteorological, biological, and chemical data throughout phytoplankton bloom periods in the North Atlantic Ocean.

My focus shifted towards ice nucleation and aerosol phase in the last year and a half of my time as a Ph.D. student. This gave me the opportunity to learn about another side of cloud formation that is more complicated and less clearly-resolved than cloud condensation nuclei and warm clouds. The time I have spent analyzing and writing for the FIN-03 project also have me the opportunity to talk to other researchers who I otherwise not have known, and to learn about forms of instrumentation I was unfamiliar with. I have summarized the technical results of FIN-03 in the previous pages of this

document, but my general, and more personal concluding statement related to this project is that I hope new ice nucleation comparisons, and in particular field comparisons, will be planned and carried out to facilitate convergence towards methods and measurements for ice nucleation instruments. I have never, even tangentially as in FIN-03, participated in the development of something before. It will probably be straightforward to purchase or build ice nucleation instruments in the future, without such ambiguity related to the ability of each instrument to measure the concentration of ice nucleation particles within the immersion and deposition (and perhaps contact) modes. Such improvements will have been facilitated by projects like FIN-03, for which I will now report a final summary of the results as previously discussed in Chapter III.

When immersion nucleation measurements carried out using five different ice nucleation instruments and methods (FRIDGE, CSU-IS, NCSU-CS collected by impinger, NCSU-CS collected by filter, and CSU-CFDC) were compared, it was found that nearly all measurements of INP concentration agreed within one order of magnitude across the participating instruments, for data collected during the same three-hour time periods. The FRIDGE also successfully measured the concentration of deposition INP throughout the campaign, and good separation was observed between immersion and deposition measurements for temperatures equal to or below -20 °C. Only a few data points were collected in the deposition mode using the CSU-CFDC. A sixth instrument (MIT-SPIN) was also able to collect ice nucleation data, though very few data points were collected under conditions relevant to immersion or deposition ice nucleation. The mean immersion INP concentration from the FRIDGE, CSU-IS, NCSU-CS, and CSU-

CFDC were successfully reproduced (85% of observation means agree with predictions within a factor of 2) at -30 °C using an immersion INP parameterization based on mineral dust concentration from Niemand et al. 2012. A lower level of agreement was observed when comparing the observation means with predicted based on a newer mineral dust parameterization from DeMott et al. 2015.

While I was working as a referee on the FIN-03 project, my advisor connected me with Dr. Charles Kolb and Dr. Yue Zhang, both working at Aerodyne at the time, and devised a study on viscosity, glass transition temperature, and their effects on ice nucleation, the results of which are discussed in Chapter IV. This study is not yet complete, and our plan is to continue this project via the other students in Dr. Sarah Brooks' lab group. I think that a point of this study that will be of particular interest will be the effect of glass transition temperature on ice nucleation, in the context of a binary mixture series of organics. This could be paired with measurements of a similar mixture series of one organic component and one inorganic component. The influences of particle phase and composition on heterogeneous ice nucleation could thus be extricated from one another (followed by additional measurements as interesting observations arise). It would have been fantastic to see the end of this study myself, but issues with lab equipment have prohibited any ice nucleation measurements in our lab for some time.

Later, my focus was rapidly towards a very different part of the field of aerosol sciences, human health, for a few months. Though I began the technical portion of this dissertation with the mask materials study, I have saved this for the third and last part of

the conclusion section (prior to closing remarks). Our advisor invited her graduate students to volunteer to collect measurements of the efficacy of standard N95 respirators, surgical masks, and household or commercially-available materials in order to provide more information for the general public to make decisions about their own health and safety.

This project came together rapidly, and it allowed our lab group to explore the topics of air quality and the transmission of airborne diseases, which one would not have expected from a group that primarily (at the time) studied the properties of aerosol particles generated from phytoplankton blooms. While we were learning the basics of filtration theory, the rest of the world was debating the usefulness of wearing masks, and other researchers engaged in rapid-fire discussion through conventional and unconventional (i.e. Twitter) means to determine the most relevant way to perform face mask evaluations. Spats erupted across the internet about the difference between aerosols and droplets, and if the historical distinction between the two (a cutoff diameter of 5 μm) had meaning in the face of a pandemic. We designed our experiments, read papers, and share our points of view within the Brooks lab group in order to make sure our measurements would have real-world relevancy—and to make sure that we could perform them rapidly enough to provide helpful information to the general public.

In the end, we found that some materials were better than others for protection against the inhalation of aerosol particles. This was not a surprising result, as the highest-performing materials (those which allowed the smallest percent of particles across the diameter range 25-500 nm to penetrate, without a proportionate increase in

breathing difficulty) were an allergen filter and an industrial composite material, two materials which are manufactured for use that was not dissimilar from the way we planned to use them. It was also not surprising that the bandana offered the least protection. However, having data to show the difference between these options is important because it provides information that can be used for protecting one's health. These results also show that even a poor-performing filter material, such as the bandana, still provides protection against aerosol inhalation. Additionally, we included references to other studies in our paper, some of which can be seen as contextualizing information on figures, that showed that the intensity of physical work load and breathing flow rate/velocity influence the efficacy of mask materials. Measurements of pressure drop across each material, which is used as a proxy for the exertion required for breathing through each material, were also carried out. The purpose of these measurements was to determine the feasibility of wearing each mask material, as no one will want to struggle to breathe through a material with a high pressure drop. It was found that the pressure drop through all of the materials did not exceed the maximum recommended by NIOSH for breathing during light physical work, though the opposite was found for heavier physical workloads. This study has been submitted for publication, and it will soon join its contemporaries in the literature as our country and world continue to fight through the COVID-19 pandemic.

I have participated in many studies, and written several papers, during my time at Texas A&M University. I hope that the Brooks lab continues finding success in data

collection and publication. I have been given many opportunities, so my concluding remark is simply, Thank You.

REFERENCES

Agresti, A., & Coull, B. A. (1998). Approximate Is Better than "Exact" for Interval Estimation of Binomial Proportions. *The American Statistician, 52*(2), 119-126. doi:10.2307/2685469

Alderman, S. L., Parsons, M. S., Hogancamp, K. U., & Waggoner, C. A. (2008). Evaluation of the effect of media velocity on filter efficiency and most penetrating particle size of nuclear grade high-efficiency particulate air filters. *J Occup Environ Hyg, 5*(11), 713-720. doi:10.1080/15459620802383934

Allen, J., & Marr, L. (2020). Re-thinking the potential for airborne transmission of SARS-CoV-2. *Preprints*. doi:10.20944/preprints202005.0126.v1

Amann-Winkel, K., Gainaru, C., Handle, P. H., Seidl, M., Nelson, H., Böhmer, R., & Loerting, T. (2013). Water's second glass transition. *Proceedings of the National Academy of Sciences, 110*(44), 17720-17725. doi:10.1073/pnas.1311718110

Anderson, N. J., Cassidy, P. E., Janssen, L. L., & Dengel, D. R. (2006). Peak inspiratory flows of adults exercising at light, moderate and heavy work loads. *Journal of the International Society for Respiratory Protection, Vol. 23*, 53-63.

Andreae, M. O., & Rosenfeld, D. (2008). Aerosol-cloud-precipitation interactions. Part 1. The nature and sources of cloud-active aerosols. *Earth-Science Reviews, 89*(1-2), 13-41. doi:10.1016/j.earscirev.2008.03.001

Ardon-Dryer, K., & Levin, Z. (2014). Ground-based measurements of immersion freezing in the eastern Mediterranean. *Atmospheric Chemistry and Physics, 14*(10), 5217-5231. doi:10.5194/acp-14-5217-2014

Bair, S. (2019). The viscosity at the glass transition of a liquid lubricant. *Friction, 7*(1), 86-91. doi:10.1007/s40544-018-0210-1

Baustian, K. J., Wise, M. E., Jensen, E. J., Schill, G. P., Freedman, M. A., & Tolbert, M. A. (2013). State transformations and ice nucleation in amorphous (semi-)solid organic aerosol. *Atmospheric Chemistry and Physics, 13*(11), 5615-5628. doi:10.5194/acp-13-5615-2013

Berkemeier, T., Shiraiwa, M., Poschl, U., & Koop, T. (2014). Competition between water uptake and ice nucleation by glassy organic aerosol particles. *Atmospheric Chemistry and Physics, 14*(22), 12513-12531. doi:10.5194/acp-14-12513-2014

Boose, Y., Sierau, B., Isabel García, M., Rodríguez, S., Alastuey, A., Linke, C., . . . Lohmann, U. (2016). Ice nucleating particles in the Saharan Air Layer.

*Atmospheric Chemistry and Physics, 16*(14), 9067-9087. doi:10.5194/acp-16-9067-2016

Brown, R. C. (1993). *Air filtration: an integrated approach to the theory and applications of fibrous filters*: Pergamon.

Cappa, C. D., & Wilson, K. R. (2011). Evolution of organic aerosol mass spectra upon heating: implications for OA phase and partitioning behavior. *Atmospheric Chemistry and Physics, 11*(5), 1895-1911. doi:10.5194/acp-11-1895-2011

CEN. (2009). *Biological evaluation of medical devices - part 1: evaluation and testing within a risk management process. Standart No. EN ISO 10993-1.*

Chandler, D., & Garrahan, J. P. (2010). Dynamics on the Way to Forming Glass: Bubbles in Space-Time. *Annual Review of Physical Chemistry, 61*(1), 191-217. doi:10.1146/annurev.physchem.040808.090405

Chen, Z., Sepulveda, A., Ediger, M. D., & Richert, R. (2012). Dielectric spectroscopy of thin films by dual-channel impedance measurements on differential interdigitated electrode arrays. *European Physical Journal B, 85*(8), 5. doi:10.1140/epjb/e2012-30363-0

Chushak, Y. G., & Bartell, L. S. (1999). Simulations of Spontaneous Phase Transitions in Large, Deeply Supercooled Clusters of SeF6. *The Journal of Physical Chemistry B, 103*(50), 11196-11204. doi:10.1021/jp992818g

Collier, K. N., & Brooks, S. D. (2016). Role of Organic Hydrocarbons in Atmospheric Ice Formation via Contact Freezing. *The Journal of Physical Chemistry A, 120*(51), 10169-10180. doi:10.1021/acs.jpca.6b11890

Creamean, J. M., Suski, K. J., Rosenfeld, D., Cazorla, A., DeMott, P. J., Sullivan, R. C., . . . Prather, K. A. (2013). Dust and biological aerosols from the Sahara and Asia influence precipitation in the western U.S. *Science, 339*(6127), 1572-1578. doi:10.1126/science.1227279

Davies, A., Thompson, K.-A., Giri, K., Kafatos, G., Walker, J., & Bennett, A. (2013). Testing the efficacy of homemade masks: would they protect in an influenza pandemic? *Disaster Medicine and Public Health Preparedness, 7*(4), 413-418. doi:10.1017/dmp.2013.43

Debenedetti, P. G., & Stillinger, F. H. (2001). Supercooled liquids and the glass transition. *Nature, 410*(6825), 259-267. doi:10.1038/35065704

DeMott, J. P. e. a. (2018). Overview of results from the Fifth International Workshop on Ice Nucleation Part 2 (FIN-02): Laboratory intercomparisons of ice nucleation measurements. *Atmos. Chem. and Phys.*, in prep.

DeMott, P. J., Möhler, O., Cziczo, D. J., Hiranuma, N., Petters, M. D., Petters, S. S., . . . Zenker, J. (2018). The Fifth International Workshop on Ice Nucleation phase 2 (FIN-02): laboratory intercomparison of ice nucleation measurements. *Atmospheric Measurement Techniques, 11*(11), 6231-6257. doi:10.5194/amt-11-6231-2018

DeMott, P. J., Prenni, A. J., Liu, X., Kreidenweis, S. M., Petters, M. D., Twohy, C. H., . . . Rogers, D. C. (2010). Predicting global atmospheric ice nuclei distributions and their impacts on climate. *Proceedings of the National Academy of Sciences of the United States of America, 107*(25), 11217-11222. doi:10.1073/pnas.0910818107

DeMott, P. J., Prenni, A. J., McMeeking, G. R., Sullivan, R. C., Petters, M. D., Tobo, Y., . . . Kreidenweis, S. M. (2015). Integrating laboratory and field data to quantify the immersion freezing ice nucleation activity of mineral dust particles. *Atmospheric Chemistry and Physics, 15*(1), 393-409. doi:10.5194/acp-15-393-2015

Diehl, K., Matthias-Maser, S., Jaenicke, R., & Mitra, S. K. (2002). The ice nucleating ability of pollen:: Part II. Laboratory studies in immersion and contact freezing modes. *Atmospheric Research, 61*(2), 125-133. doi:https://doi.org/10.1016/S0169-8095(01)00132-6

Djikaev, Y. S., Tabazadeh, A., Hamill, P., & Reiss, H. (2002). Thermodynamic Conditions for the Surface-Stimulated Crystallization of Atmospheric Droplets. *The Journal of Physical Chemistry A, 106*(43), 10247-10253. doi:10.1021/jp021044s

Durant, A. J., & Shaw, R. A. (2005). Evaporation freezing by contact nucleation inside-out. *Geophysical Research Letters, 32*(20). doi:10.1029/2005gl024175

Eidhammer, T., DeMott, P. J., Prenni, A. J., Petters, M. D., Twohy, C. H., Rogers, D. C., . . . Kreidenweis, S. M. (2010). Ice Initiation by Aerosol Particles: Measured and Predicted Ice Nuclei Concentrations versus Measured Ice Crystal Concentrations in an Orographic Wave Cloud. *Journal of the Atmospheric Sciences, 67*(8), 2417-2436. doi:10.1175/2010jas3266.1

Eninger, R. M., Honda, T., Adhikari, A., Heinonen-Tanski, H., Reponen, T., & Grinshpun, S. A. (2008). Filter performance of N99 and N95 facepiece respirators against viruses and ultrafine particles. *The Annals of Occupational Hygiene, 52*(5), 385-396. doi:10.1093/annhyg/men019

FDA. (2016). *Guidance for Industry and Food and Drug Administration staff, use of International Standard ISO 10993-1, "Biological evaluation of medical devices - part 1: evaluation and testing within a risk management process"*.

Fears, A. C., Klimstra, W. B., Duprex, P., Hartman, A., Weaver, S. C., Plante, K. S., . . . Roy, C. J. (2020). Comparative dynamic aerosol efficiencies of three emergent coronaviruses and the unusual persistence of SARS-CoV-2 in aerosol suspensions. *medRxiv*, 2020.2004.2013.20063784. doi:10.1101/2020.04.13.20063784

Fornea, A. P., Brooks, S. D., Dooley, J. B., & Saha, A. (2009). Heterogeneous freezing of ice on atmospheric aerosols containing ash, soot, and soil. *Journal of Geophysical Research: Atmospheres, 114*(D13). doi:10.1029/2009jd011958

Froyd, K. D., Murphy, D. M., Brock, C. A., Campuzano-Jost, P., Dibb, J. E., Jimenez, J. L., . . . Ziemba, L. D. (2019). A new method to quantify mineral dust and other aerosol species from aircraft platforms using single-particle mass spectrometry. *Atmospheric Measurement Techniques, 12*(11), 6209-6239. doi:10.5194/amt-12-6209-2019

Fukuta, N. (1975). A Study of the Mechanism of Contact Ice Nucleation. *Journal of the Atmospheric Sciences, 32*(8), 1597-1603. doi:10.1175/1520-0469(1975)032<1597:Asotmo>2.0.Co;2

Gabey, A. M., Gallagher, M. W., Whitehead, J., Dorsey, J. R., Kaye, P. H., & Stanley, W. R. (2010). Measurements and comparison of primary biological aerosol above and below a tropical forest canopy using a dual channel fluorescence spectrometer. *Atmospheric Chemistry and Physics, 10*(10), 4453-4466. doi:10.5194/acp-10-4453-2010

Garimella, S., Kristensen, T. B., Ignatius, K., Welti, A., Voigtländer, J., Kulkarni, G. R., . . . Cziczo, D. J. (2016). The SPectrometer for Ice Nuclei (SPIN): an instrument to investigate ice nucleation. *Atmospheric Measurement Techniques, 9*(7), 2781-2795. doi:10.5194/amt-9-2781-2016

Garimella, S., Rothenberg, D. A., Wolf, M. J., David, R. O., Kanji, Z. A., Wang, C., . . . Cziczo, D. J. (2017). Uncertainty in counting ice nucleating particles with continuous flow diffusion chambers. *Atmospheric Chemistry and Physics, 17*(17), 10855-10864. doi:10.5194/acp-17-10855-2017

Garimella, S., Rothenberg, D. A., Wolf, M. J., David, R. O., Kanji, Z. A., Wang, C., . . . Cziczo, D. J. (2017). Uncertainty in counting ice nucleating particles with continuous flow diffusion chambers. *Atmospheric Chemistry and Physics, 17*(17), 10855-10864. doi:10.5194/acp-17-10855-2017

Gavin, H. P. (2019). *The Levenberg-Marquardt algorithm for nonlinear least squares curve-fitting problems*.

Hader, J. D., Wright, T. P., & Petters, M. D. (2014). Contribution of pollen to atmospheric ice nuclei concentrations. *Atmospheric Chemistry and Physics, 14*(11), 5433-5449. doi:10.5194/acp-14-5433-2014

Han, Q., Lin, Q., Ni, Z., & You, L. (2020). Uncertainties about the transmission routes of 2019 novel coronavirus. *Influenza and Other Respiratory Viruses, n/a*(n/a). doi:10.1111/irv.12735

Hill, T., McCluskey, C., Michaud, J., Santander, M., Cornwell, G., Sultana, C., . . . DeMott, P. (2016). Characteristics of ice nucleating particles in seawater and sea spray aerosol produced during laboratory phytoplankton blooms. *Abstracts of Papers of the American Chemical Society, 251*, 2. Retrieved from <Go to ISI>://WOS:000431905705467

Hiranuma, N., Adachi, K., Bell, D. M., Belosi, F., Beydoun, H., Bhaduri, B., . . . Möhler, O. (2019). A comprehensive characterization of ice nucleation by three different types of cellulose particles immersed in water. *Atmospheric Chemistry and Physics, 19*(7), 4823-4849. doi:10.5194/acp-19-4823-2019

Hiranuma, N., Augustin-Bauditz, S., Bingemer, H., Budke, C., Curtius, J., Danielczok, A., . . . Yamashita, K. (2015). A comprehensive laboratory study on the immersion freezing behavior of illite NX particles: a comparison of 17 ice nucleation measurement techniques. *Atmospheric Chemistry and Physics, 15*(5), 2489-2518. doi:10.5194/acp-15-2489-2015

Howard, J., Huang, A., Li, Z., Tufekci, Z., Zdimal, V., van der Westhuizen, H., . . . Rimoin, A. W. (2020). Face masks against COVID-19: an evidence review. *Preprints (submitted to PNAS)*. doi:doi: 10.20944/preprints202004.0203.v2

Huang, S.-H., Chen, C.-W., Kuo, Y.-M., Lai, C.-Y., McKay, R., & Chen, C.-C. (2013). Factors affecting filter penetration and quality factor of particulate respirators. *Aerosol and Air Quality Research, 13*(1), 162-171. doi:10.4209/aaqr.2012.07.0179

Hudson, A., & Mandadapu, K. (2018). On the nature of the glass transition in atomistic models of glass formers.

Huffman, J. A., Prenni, A. J., DeMott, P. J., Pöhlker, C., Mason, R. H., Robinson, N. H., . . . Pöschl, U. (2013). High concentrations of biological aerosol particles and ice nuclei during and after rain. *Atmospheric Chemistry and Physics, 13*(13), 6151-6164. doi:10.5194/acp-13-6151-2013

Janssen, L., Anderson, N., Cassidy, P., Weber, R., & Nelson, T. (2005). Interpretation of inhalation airflow measurements for respirator design and testing. *Journal of the International Society for Respiratory Protection, 22*, 122-141. doi:10.3320/1.2753437

Jensen, E. J., Kärcher, B., Ueyama, R., Pfister, L., Bui, T. V., Diskin, G. S., . . . Murphy, D. M. (2018). Heterogeneous Ice Nucleation in the Tropical Tropopause Layer. *Journal of Geophysical Research: Atmospheres, 123*(21), 12,210-212,227. doi:10.1029/2018jd028949

Jung, H., Kim, J. K., Lee, S., Lee, J., Kim, J., Tsai, P., & Yoon, C. (2014). Comparison of filtration efficiency and pressure drop in anti-yellow sand masks, quarantine masks, medical masks, general masks, and handkerchiefs. *Aerosol and Air Quality Research, 14*(3), 991-1002. doi:10.4209/aaqr.2013.06.0201

Kanji, Z. A., Ladino, L. A., Wex, H., Boose, Y., Burkert-Kohn, M., Cziczo, D. J., & Krämer, M. (2017). Overview of Ice Nucleating Particles. *Meteorological Monographs, 58*, 1.1-1.33. doi:10.1175/amsmonographs-d-16-0006.1

Kaye, P. H., Stanley, W. R., Hirst, E., Foot, E. V., Baxter, K. L., & Barrington, S. J. (2005). Single particle multichannel bio-aerosol fluorescence sensor. *Optics Express, 13*(10), 3583-3593. doi:10.1364/OPEX.13.003583

Keys, A. S., Garrahan, J. P., & Chandler, D. (2013). Calorimetric glass transition explained by hierarchical dynamic facilitation. *Proceedings of the National Academy of Sciences, 110*(12), 4482-4487. doi:10.1073/pnas.1302665110

Konda, A., Prakash, A., Moss, G. A., Schmoldt, M., Grant, G. D., & Guha, S. (2020). Aerosol filtration efficiency of common fabrics used in respiratory cloth masks. *ACS Nano*. doi:10.1021/acsnano.0c03252

Koop, T., Bookhold, J., Shiraiwa, M., & Pöschl, U. (2011). Glass transition and phase state of organic compounds: dependency on molecular properties and implications for secondary organic aerosols in the atmosphere. *Physical Chemistry Chemical Physics, 13*(43), 19238-19255. doi:10.1039/C1CP22617G

Krizner, H. E., De Haan, D. O., & Kua, J. (2009). Thermodynamics and Kinetics of Methylglyoxal Dimer Formation: A Computational Study. *The Journal of Physical Chemistry A, 113*(25), 6994-7001. doi:10.1021/jp903213k

Kulkarni, G., & Kok, G. (2012). *Mobile Ice Nucleus Spectrometer*. Retrieved from Richland, WA, 2012:

Leung, N. H. L., Chu, D. K. W., Shiu, E. Y. C., Chan, K.-H., McDevitt, J. J., Hau, B. J. P., . . . Cowling, B. J. (2020). Respiratory virus shedding in exhaled breath and efficacy of face masks. *Nature Medicine, 26*(5), 676-680. doi:10.1038/s41591-020-0843-2

Levin, E. J. T., DeMott, P. J., Suski, K. J., Boose, Y., Hill, T. C. J., McCluskey, C. S., . . . Kreidenweis, S. M. (2019). Characteristics of Ice Nucleating Particles in and Around California Winter Storms. *Journal of Geophysical Research: Atmospheres, 124*(21), 11530-11551. doi:10.1029/2019jd030831

Levin, Z., & Yankofsky, S. A. (1983). Contact Versus Immersion Freezing of Freely Suspended Droplets by Bacterial Ice Nuclei. *Journal of Climate and Applied Meteorology, 22*(11), 1964-1966. doi:10.1175/1520-0450(1983)022<1964:Cvifof>2.0.Co;2

Lienhard, D. M., Zobrist, B., Zuend, A., Krieger, U. K., & Peter, T. (2012). Experimental evidence for excess entropy discontinuities in glass-forming solutions. *Journal of Chemical Physics, 136*(7), 9. doi:10.1063/1.3685902

Lindsley, W. G., Blachere, F. M., Thewlis, R. E., Vishnu, A., Davis, K. A., Cao, G., . . . Beezhold, D. H. (2010). Measurements of airborne influenza virus in aerosol particles from human coughs. *Plos One, 5*(11), e15100. doi:10.1371/journal.pone.0015100

Liu, Y., Ning, Z., Chen, Y., Guo, M., Liu, Y., Gali, N. K., . . . Lan, K. (2020). Aerodynamic characteristics and RNA concentration of SARS-CoV-2 aerosol in Wuhan hospitals during COVID-19 outbreak. *bioRxiv*, 2020.2003.2008.982637. doi:10.1101/2020.03.08.982637

Mason, R. H., Chou, C., McCluskey, C. S., Levin, E. J. T., Schiller, C. L., Hill, T. C. J., . . . Bertram, A. K. (2015). The micro-orifice uniform deposit impactor–droplet freezing technique (MOUDI-DFT) for measuring concentrations of ice nucleating particles as a function of size: improvements and initial validation. *Atmospheric Measurement Techniques, 8*(6), 2449-2462. doi:10.5194/amt-8-2449-2015

McCluskey, C. S., DeMott, P. J., Prenni, A. J., Levin, E. J. T., McMeeking, G. R., Sullivan, A. P., . . . Kreidenweis, S. M. (2014). Characteristics of atmospheric ice nucleating particles associated with biomass burning in the US: Prescribed burns and wildfires. *Journal of Geophysical Research: Atmospheres, 119*(17), 10458-10470. doi:10.1002/2014jd021980

Morawska, L. (2006). Droplet fate in indoor environments, or can we prevent the spread of infection? *Indoor Air, 16*(5), 335-347. doi:10.1111/j.1600-0668.2006.00432.x

Morawska, L., Johnson, G. R., Ristovski, Z. D., Hargreaves, M., Mengersen, K., Corbett, S., . . . Katoshevski, D. (2009). Size distribution and sites of origin of droplets expelled from the human respiratory tract during expiratory activities. *Journal of Aerosol Science, 40*(3), 256-269. doi:https://doi.org/10.1016/j.jaerosci.2008.11.002

Morris, C. E., Sands, D. C., Bardin, M., Jaenicke, R., Vogel, B., Leyronas, C., . . . Psenner, R. (2011). Microbiology and atmospheric processes: research challenges concerning the impact of airborne micro-organisms on the atmosphere and climate. *Biogeosciences, 8*, 17. doi:10.5194/bg-8-17-2011

Murray, B. J. (2008). Inhibition of ice crystallisation in highly viscous aqueous organic acid droplets. *Atmospheric Chemistry and Physics, 8*(17), 5423-5433. doi:10.5194/acp-8-5423-2008

Murray, B. J., O'Sullivan, D., Atkinson, J. D., & Webb, M. E. (2012). Ice nucleation by particles immersed in supercooled cloud droplets. *Chemical Society Reviews, 41*(19), 6519-6554. doi:10.1039/C2CS35200A

Murray, B. J., Wilson, T. W., Dobbie, S., Cui, Z. Q., Al-Jumur, S., Mohler, O., . . . Karcher, B. (2010). Heterogeneous nucleation of ice particles on glassy aerosols under cirrus conditions. *Nature Geoscience, 3*(4), 233-237. doi:10.1038/ngeo817

National Center for Immunization and Respiratory Diseases, D. o. V. D. (2020). Use of cloth face coverings to help slow the spread of COVID-19. Retrieved from https://www.cdc.gov/coronavirus/2019-ncov/prevent-getting-sick/diy-cloth-face-coverings.html?fbclid=IwAR3fnY1F69-EO-ibiv12puUL5o9KunxKapEpznPDOxbmxg5Gie_V36DoKE0

Niehaus, J., & Cantrell, W. (2015). Contact Freezing of Water by Salts. *The Journal of Physical Chemistry Letters, 6*(17), 3490-3495. doi:10.1021/acs.jpclett.5b01531

Niemand, M., Mohler, O., Vogel, B., Vogel, H., Hoose, C., Connolly, P., . . . Leisner, T. (2012). A Particle-Surface-Area-Based Parameterization of Immersion Freezing on Desert Dust Particles. *Journal of the Atmospheric Sciences, 69*(10), 3077-3092. doi:10.1175/jas-d-11-0249.1

NIOSH. (1995). *Part Ii: Department Of Health And Human Services: Department Of Labor: Department Of Labor: Department Of Health And Human Services: Department Of Health And Human Services: Public Health Service: Rules and Regulations: Respiratory Protective Devices: [FR DOC # 95-13287].* (42 CFR 84.180). Retrieved from https://heinonline-org.srv-proxy2.library.tamu.edu/HOL/P?h=hein.fedreg/060110&i=167

NIOSH. (2019). *Determination of particulate filter efficiency level for N95 series filters against solid particulates for non-powered, air-purifying respirators standard testing procedure (STP)*.

Oberg, T., & Brosseau, L. M. (2008). Surgical mask filter and fit performance. *American Journal of Infection Control, 36*(4), 276-282. doi:https://doi.org/10.1016/j.ajic.2007.07.008

OSHA. (2004). *Appendix A to §1910.134—Fit Testing Procedures (Mandatory)*.

Perring, A. E., Schwarz, J. P., Baumgardner, D., Hernandez, M. T., Spracklen, D. V., Heald, C. L., . . . Fahey, D. W. (2015). Airborne observations of regional variation in fluorescent aerosol across the United States. *Journal of Geophysical Research-Atmospheres, 120*(3), 1153-1170. doi:10.1002/2014jd022495

Pitter, R., & Pruppacher, H. (2007). A wind tunnel investigation of freezing of small water drops falling at terminal velocity in air. *Quarterly Journal of the Royal Meteorological Society, 99*, 540-550. doi:10.1002/qj.49709942111

Pruppacher, H. R., & Klett, J. (2010). *Microphysics of Clouds and Precipitation* (Vol. 18).

Ramirez, J., & O'Shaughnessy, P. (2017). Filter penetration and breathing resistance evaluation of respirators and dust masks. *Journal of Occupational and Environmental Hygiene, 14*(2), 148-157. doi:10.1080/15459624.2016.1237027

Raynor, P. C., Leith, D., Lee, K. W., & Mukund, R. (2011). Sampling and analysis using filters. In *Aerosol Measurement* (pp. 107-128).

Rengasamy, S., Eimer, B., & Shaffer, R. E. (2010). Simple respiratory protection—evaluation of the filtration performance of cloth masks and common fabric materials against 20–1000 nm size particles. *The Annals of Occupational Hygiene, 54*(7), 789-798. doi:10.1093/annhyg/meq044

Rengasamy, S., Shaffer, R., Williams, B., & Smit, S. (2017). A comparison of facemask and respirator filtration test methods. *Journal of Occupational and Environmental Hygiene, 14*(2), 92-103. doi:10.1080/15459624.2016.1225157

Rogers, D. C. (1988). Development of a continuous flow thermal gradient diffusion chamber for ice nucleation studies. *Atmospheric Research, 22*(2), 149-181. doi:https://doi.org/10.1016/0169-8095(88)90005-1

Rogers, D. C., DeMott, P. J., Kreidenweis, S. M., & Chen, Y. (2001). A Continuous-Flow Diffusion Chamber for Airborne Measurements of Ice Nuclei. *Journal of*

*Atmospheric and Oceanic Technology, 18*(5), 725-741. doi:10.1175/1520-0426(2001)018<0725:Acfdcf>2.0.Co;2

Sachinidou, P., Bahk, Y. K., & Wang, J. (2017). An integrative model for the filtration efficiencies in realistic tests with consideration of the filtration velocity profile and challenging particle size distribution. *Aerosol Science and Technology, 51*(2), 178-187. doi:10.1080/02786826.2016.1254720

Saukko, E., Kuuluvainen, H., & Virtanen, A. (2012). A method to resolve the phase state of aerosol particles. *Atmospheric Measurement Techniques, 5*(1), 259-265. doi:10.5194/amt-5-259-2012

Schilling, K., Gentner, D., Wilen, L., Medina, A., Buehler, C., Perez-Lorenzo, L., . . . Lattanza, L. (2020). An accessible method for screening aerosol filtration identifies poor-performing commercial masks and respirators. *SSRN Electronic Journal*. doi:10.2139/ssrn.3592485

Schrod, J., Danielczok, A., Weber, D., Ebert, M., Thomson, E. S., & Bingemer, H. G. (2016). Re-evaluating the Frankfurt isothermal static diffusion chamber for ice nucleation. *Atmospheric Measurement Techniques, 9*(3), 1313-1324. doi:10.5194/amt-9-1313-2016

Seifert, P., Ansmann, A., Groß, S., Freudenthaler, V., Heinold, B., Hiebsch, A., . . . Wiegner, M. (2011). Ice formation in ash-influenced clouds after the eruption of the Eyjafjallajökull volcano in April 2010. *Journal of Geophysical Research: Atmospheres, 116*(D20). doi:10.1029/2011jd015702

Shakya, K. M., Noyes, A., Kallin, R., & Peltier, R. E. (2017). Evaluating the efficacy of cloth facemasks in reducing particulate matter exposure. *Journal of Exposure Science & Environmental Epidemiology, 27*(3), 352-357. doi:10.1038/jes.2016.42

Shaw, R. A., Durant, A. J., & Mi, Y. (2005). Heterogeneous Surface Crystallization Observed in Undercooled Water. *The Journal of Physical Chemistry B, 109*(20), 9865-9868. doi:10.1021/jp0506336

Shiraiwa, M., Ammann, M., Koop, T., & Poschl, U. (2011). Gas uptake and chemical aging of semisolid organic aerosol particles. *Proceedings of the National Academy of Sciences of the United States of America, 108*(27), 11003-11008. doi:10.1073/pnas.1103045108

Shiraiwa, M., Li, Y., Tsimpidi, A. P., Karydis, V. A., Berkemeier, T., Pandis, S. N., . . . Poschl, U. (2017). Global distribution of particle phase state in atmospheric

secondary organic aerosols. *Nature Communications, 8*, 7. doi:10.1038/ncomms15002

Simha, R., & Boyer, R. F. (1962). On a General Relation Involving the Glass Temperature and Coefficients of Expansion of Polymers. *The Journal of Chemical Physics, 37*(5), 1003-1007. doi:10.1063/1.1733201

Sipahl, H., Bayram, F. E. O., Palabiyik, S. S., Bayram, D., & Aydin, A. (2018). Investigation of the biocompatibility of surgical masks. *Pteridines, 29*(1), 80. doi:https://doi.org/10.1515/pteridines-2018-0007

Stevens, G. A., & Moyer, E. S. (1989). "Worst case" aerosol testing parameters: I. sodium chloride and dioctyl phthalate aerosol filter efficiency as a function of particle size and flow rate. *American Industrial Hygiene Association Journal, 50*(5), 257-264. doi:10.1080/15298668991374615

Tabazadeh, A., Djikaev, Y. S., & Reiss, H. (2002). Surface crystallization of supercooled water in clouds. *Proceedings of the National Academy of Sciences, 99*(25), 15873-15878. doi:10.1073/pnas.252640699

Tobo, Y., Prenni, A. J., DeMott, P. J., Huffman, J. A., McCluskey, C. S., Tian, G. X., . . . Kreidenweis, S. M. (2013). Biological aerosol particles as a key determinant of ice nuclei populations in a forest ecosystem. *Journal of Geophysical Research-Atmospheres, 118*(17), 10100-10110. doi:10.1002/jgrd.50801

Vaden, T. D., Song, C., Zaveri, R. A., Imre, D., & Zelenyuk, A. (2010). Morphology of mixed primary and secondary organic particles and the adsorption of spectator organic gases during aerosol formation. *Proceedings of the National Academy of Sciences, 107*(15), 6658-6663. doi:10.1073/pnas.0911206107

Vali, G. (1971). Quantitative Evaluation of Experimental Results an the Heterogeneous Freezing Nucleation of Supercooled Liquids. *Journal of the Atmospheric Sciences, 28*(3), 402-409. doi:10.1175/1520-0469(1971)028<0402:Qeoera>2.0.Co;2

Vali, G. (1996). Ice nucleation-a review. *Nucleation and Atmospheric Aerosols*, 271-279. doi:10.1016/B978-008042030-1/50066-4

van der Sande, M., Teunis, P., & Sabel, R. (2008). Professional and home-made face masks reduce exposure to respiratory infections among the general population. *Plos One, 3*(7), e2618. doi:10.1371/journal.pone.0002618

van Doremalen, N., Bushmaker, T., Morris, D. H., Holbrook, M. G., Gamble, A., Williamson, B. N., . . . Munster, V. J. (2020). Aerosol and surface stability of

SARS-CoV-2 as compared with SARS-CoV-1. *New England Journal of Medicine, 382*(16), 1564-1567. doi:10.1056/NEJMc2004973

Virtanen, A., Joutsensaari, J., Koop, T., Kannosto, J., Yli-Pirila, P., Leskinen, J., . . . Laaksonen, A. (2010). An amorphous solid state of biogenic secondary organic aerosol particles. *Nature, 467*(7317), 824-827. doi:10.1038/nature09455

Wagner, R., Mohler, O., Saathoff, H., Schnaiter, M., Skrotzki, J., Leisner, T., . . . Murray, B. J. (2012). Ice cloud processing of ultra-viscous/glassy aerosol particles leads to enhanced ice nucleation ability. *Atmospheric Chemistry and Physics, 12*(18), 8589-8610. doi:10.5194/acp-12-8589-2012

Wang, B., Lambe, A. T., Massoli, P., Onasch, T. B., Davidovits, P., Worsnop, D. R., & Knopf, D. A. (2012). The deposition ice nucleation and immersion freezing potential of amorphous secondary organic aerosol: Pathways for ice and mixed-phase cloud formation. *Journal of Geophysical Research: Atmospheres, 117*(D16). doi:10.1029/2012jd018063

Wang, J., & Du, G. (2020). COVID-19 may transmit through aerosol. *Irish journal of medical science*, 1-2. doi:10.1007/s11845-020-02218-2

Wells, W. F. (1934). On air-borne infection*: Study II. droplets and droplet nuclei. *American Journal of Epidemiology, 20*(3), 611-618. doi:10.1093/oxfordjournals.aje.a118097

Wells, W. F. (1955). *Airborne contagion and air hygiene; an ecological study of droplet infections*. Cambridge, Mass.: Harvard Univ. Press.

Wex, H., Augustin-Bauditz, S., Boose, Y., Budke, C., Curtius, J., Diehl, K., . . . Stratmann, F. (2015). Intercomparing different devices for the investigation of ice nucleating particles using Snomax (R) as test substance. *Atmospheric Chemistry and Physics, 15*(3), 1463-1485. doi:10.5194/acp-15-1463-2015

Whipple, E. B. (1970). Structure of glyoxal in water. *Journal of the American Chemical Society, 92*(24), 7183-7186. doi:10.1021/ja00727a027

Willeke, K., Lin, X., & Grinshpun, S. A. (1998). Improved Aerosol Collection by Combined Impaction and Centrifugal Motion. *Aerosol Science and Technology, 28*(5), 439-456. doi:10.1080/02786829808965536

Wölfel, R., Corman, V. M., Guggemos, W., Seilmaier, M., Zange, S., Müller, M. A., . . . Wendtner, C. (2020). Virological assessment of hospitalized patients with COVID-2019. *Nature*. doi:10.1038/s41586-020-2196-x

Wright, T. P., & Petters, M. D. (2013). The role of time in heterogeneous freezing nucleation. *Journal of Geophysical Research: Atmospheres, 118*(9), 3731-3743. doi:10.1002/jgrd.50365

Wright, T. P., Petters, M. D., Hader, J. D., Morton, T., & Holder, A. L. (2013). Minimal cooling rate dependence of ice nuclei activity in the immersion mode. *Journal of Geophysical Research: Atmospheres, 118*(18), 10,535-510,543. doi:10.1002/jgrd.50810

Yadav, S., Venezia, R. E., Paerl, R. W., & Petters, M. D. (2019). Characterization of Ice-Nucleating Particles Over Northern India. *Journal of Geophysical Research: Atmospheres, 124*(19), 10467-10482. doi:10.1029/2019jd030702

Yan, J., Guha, S., Hariharan, P., & Myers, M. (2019). Modeling the effectiveness of respiratory protective devices in reducing influenza outbreak. *Risk Analysis, 39*(3), 647-661. doi:10.1111/risa.13181

Yuasa, H., Kumita, M., Honda, T., Kimura, K., Nozaki, K., Emi, H., & Otani, Y. (2015). Breathing simulator of workers for respirator performance test. *Industrial health, 53*(2), 124-131. doi:10.2486/indhealth.2014-0079

Zawadowicz, M. A., Froyd, K. D., Perring, A. E., Murphy, D. M., Spracklen, D. V., Heald, C. L., . . . Cziczo, D. J. (2019). Model-measurement consistency and limits of bioaerosol abundance over the continental United States. *Atmospheric Chemistry and Physics, 19*(22), 13859-13870. doi:10.5194/acp-19-13859-2019

Zhang, Y., Katira, S., Lee, A., Lambe, A. T., Onasch, T. B., Xu, W., . . . Kolb, C. E. (2018). Kinetically controlled glass transition measurement of organic aerosol thin films using broadband dielectric spectroscopy. *Atmospheric Measurement Techniques, 11*(6), 3479-3490. doi:10.5194/amt-11-3479-2018

Zhang, Y., Nichman, L., Spencer, P., Jung, J. I., Lee, A., Heffernan, B. K., . . . Kolb, C. E. (2019). The Cooling Rate- and Volatility-Dependent Glass-Forming Properties of Organic Aerosols Measured by Broadband Dielectric Spectroscopy. *Environmental Science & Technology, 53*(21), 12366-12378. doi:10.1021/acs.est.9b03317

Zhao, M., Liao, L., Xiao, W., Yu, X., Wang, H., Wang, Q., . . . Cui, Y. (2020). Household Materials Selection for Homemade Cloth Face Coverings and Their Filtration Efficiency Enhancement with Triboelectric Charging. *Nano Letters*. doi:10.1021/acs.nanolett.0c02211

Zhu, N., Zhang, D., Wang, W., Li, X., Yang, B., Song, J., . . . Tan, W. (2020). A novel coronavirus from patients with pneumonia in China, 2019. *New England Journal of Medicine, 382*(8), 727-733. doi:10.1056/NEJMoa2001017

Zobrist, B., Marcolli, C., Pedernera, D. A., & Koop, T. (2008). Do atmospheric aerosols form glasses? *Atmospheric Chemistry and Physics, 8*(17), 5221-5244. doi:10.5194/acp-8-5221-2008

Zondervan, R., Kulzer, F., Berkhout, G. C. G., & Orrit, M. (2007). Local viscosity of supercooled glycerol near T<sub>g</sub> probed by rotational diffusion of ensembles and single dye molecules. *Proceedings of the National Academy of Sciences, 104*(31), 12628-12633. doi:10.1073/pnas.0610521104

# APPENDIX A

# ADDITIONAL METHODS AND FIGURES FOR THE FIFTH INTERNATIONAL WORKSHOP ON ICE NUCLEATION PHASE 3 (FIN-03): FIELD INTERCOMPARISON OF ICE NUCLEATION MEASUREMENTS

## Online measurement systems

The two online instruments employed during FIN-03, the Colorado State University Continuous Flow Diffusion Chamber (CSU-CFDC) and the SPectrometer for Ice Nuclei (SPIN; Droplet Measurement Technologies, Boulder, CO). The CSU-CFDC operating principles are described in the earlier works of (Eidhammer et al., 2010; Rogers, 1988; Rogers et al., 2001). Application and considerations for interpreting data have been described in detail in a number of publications, most recently by (P. J. DeMott et al., 2018). Briefly, CSU-CFDC is composed of nested cylindrical copper walls that are chemically ebonized to be hydrophilic so they can be evenly coated with ice. The chamber is divided into two sections vertically. For FIN-03, the CSU-CFDC was operated to establish a temperature gradient between the colder (inner) and warmer (outer) ice walls in the upper ~50 cm "growth" section in order to produce either water subsaturated or water supersaturated conditions at various temperatures within a central lamina. For the flow rates used (10 volumetric L $min^{-1}$ total flow, 1.5 volumetric L $min^{-1}$ sample flow), this leads to a residence time of ~5 s in the growth region. Aerosol particles were directed into that central lamina. Ice crystals forming on INPs in the growth section continued to grow for ~2 s in the lower ~35 cm "evaporation" section of

the chamber where the outer wall temperature was adjusted to be at an equivalent temperature to the inner (cold) wall in order to promote evaporation of liquid drops. When operating in the water supersaturated regime, water relative humidity was controlled to be nominally at 105% during FIN-03 in order to stimulate droplet growth and subsequent freezing, for best comparison to offline immersion freezing methods. For comparison to deposition freezing measurements, relative humidity was controlled to ~94% RH to probe direct deposition of gaseous water onto the aerosol and subsequent freezing.

Prior to entering the CSU-CFDC, aerosol was dried using two inline diffusion driers and then size-limited using dual single-jet impactors that achieve a 50% "cut-point" size of 2.5 μm. This limitation on aerosol sizes helps to remove ambiguity when distinguishing ice crystals at ~4 μm sizes from aerosol particles using an optical particle counter at the CSU-CFDC outlet. Temperature uncertainty is ± 0.5°C at the reported CSU-CFDC lamina processing temperature (Hiranuma et al., 2015). Relative humidity uncertainty depends inversely on temperature, as discussed in DeMott et al., 2018, estimated for example as 2.4 % at -25°C.

In order to correct for background counts that can occur due to ejection of frost formed within the CSU-CFDC over operational periods, and for defining measurement uncertainties, we follow (E. J. T. Levin et al., 2019). Frost corrections are defined through intervals of sampling ambient air through a High-Efficiency Particulate Air (HEPA) filter. Sample data were background corrected by subtracting the interpolated filter period concentration before and after each sampling period. Background corrected data were then

averaged to ~5-min sampling times to increase statistical confidence. Poisson counting errors during filtered and ambient sampling periods were added in quadrature, and INP concentrations were considered to be statistically significant at the 95% confidence level if they were greater than 1.64 times this combined INP error. Inlet tubing losses are not considered in the reported INP data.

During FIN-03, an aerosol concentrator (MSP Model 4240) was used at selected times to improve sampling statistics, in the same manner as (Tobo et al., 2013). Concentration factors were evaluated in the same manner as Tobo et al., 2013, leading to an average increase of INPs by 90 times during operation of the aerosol concentrator.

The SPIN is a parallel plate continuous flow diffusion chamber style instrument. The theory and operation of SPIN has been described previously (Garimella et al., 2016; Garimella, Rothenberg, Wolf, David, Kanji, Wang, Rösch, et al., 2017). SPIN consists of two flat walls separated by 1.0 cm and coated in approximately 1.0 mm of ice. Aerosol particles are fed into the chamber in a lamina flow of about 1.0 liters per minute and are constrained to the centerline with a sheath flow of about 9.0 liters per minute. The temperature and relative humidity that the aerosol lamina experiences are controlled by varying the temperature gradient between the two iced walls (Kulkarni & Kok, 2012). After existing the nucleation chamber, the particles enter SPIN's optical particle counter, which sizes aerosol on a particle by particle basis for diameters between 0.2 and 15 μm.

**Offline measurement systems**

Three types of offline instruments were employed during FIN-03. The samples analyzed using these methods were initially collected on substrate wafers, filters, or in aqueous suspension (using an impinger) and later cooled in order to determine the temperature at which ice nucleation was initiated. A brief description of sample collection and analysis for each of these methods follows.

The first offline instrument employed during FIN-03 was the FRankfurt Ice nucleation Deposition freezinG Experiment (FRIDGE). Briefly, the FRIDGE can be used to measure the concentration of INP through two different methods, the “standard” method and a droplet freezing assay method. In the "standard" method aerosol particles are sampled by electrostatic precipitation onto silicon wafer substrates. The samples are then exposed to supercooled and ice-supersaturated conditions by diffusion of water vapor in the offline chamber. The ice-supersaturation conditions are equivalent to 95%, 99%, and 102% $RH_W$. Ice crystals activate on INPs at the surface of the substrate within some tens of seconds and can be visually detected by a CCD camera. Immersion freezing experiments are carried out by droplet freezing assay inside the same instrument. Aerosol particles are sampled by filtration through 0.2 µm Millipore PTFE filters. The filter samples are extracted in deionized water, and 0.5 µl droplets of the solution are pipetted onto a silanized silicon substrate. Then the substrate is cooled by 1°C per min until every droplet is frozen. The “standard” method for the is described in greater detail in (Schrod et al., 2016), and the droplet freezing assay method is described

in greater detail in (P. J. DeMott et al., 2018; Hiranuma et al., 2019; Hiranuma et al., 2015).

The second offline instrument was the Colorado State University Ice Spectrometer (CSU-IS). The CSU-IS was used to post-process particles sampled onto filters during FIN-03. This instrument was first described in Hiranuma et al., 2015 and in a number of publications since. Samples were collected for approximate periods of 4 hours for intercomparison periods (longer for overnight samples) using pre-cleaned open-faced holders for 0.2 μm pore diameter, 47 mm polycarbonate Nucleopore filters, with a typical sample flow rate 14.9 L $min^{-1}$ (ambient) and 9.5 L $min^{-1}$ (STP). All samples were frozen following collection, and until processing at CSU. Filters pre-sterilization procedures and overall clean protocols are detailed in the supplement of DeMott et al., 2018. Particle re-suspension was done through 20 minutes of shaking filters in sterile 50 mL Falcon polypropylene tubes (Corning Life Sciences) with 6-10 mL of suspension solution composed of 2 mM KCl in 0.02 μm pore diameter filtered water. Further 20-fold dilutions using the suspension solution were made as needed to permit measurement of freezing spectra to the lowest temperature limit of operation of the CSU-IS.

Immersion freezing INP temperature spectra were obtained by distributing 32 aliquots of 50 μL particle suspensions into the sterile 96-well PCR trays that mount in the CSU-IS. The cooling rate was 0.33°C $min^{-1}$. Frozen wells were counted at 0.2-1°C degree intervals to a limit of -28°C, and cumulative numbers of INP $mL^{-1}$ of suspension estimated following (Vali, 1971). Conversion to ambient air concentrations std $L^{-1}$ were made on the basis of distributed suspension volume and the total air volumes collected. Filter blanks

were collected during FIN-03, and these were averaged to obtain background INP numbers per filter in volumes of liquid suspension in order to correct data prior to computation of INP concentrations. Binomial sampling confidence intervals (95%) were derived for INP concentrations following (Agresti & Coull, 1998). The temperature uncertainty is ±0.2°C.

The third and final offline instrument was the NCSU cold stage (NCSU-CS), previously described by (Wright & Petters, 2013) and (Hader et al., 2014). Procedures used for collecting immersion freezing spectra are described below and by (Yadav, Venezia, Paerl, & Petters, 2019). During FIN-03, filter samples, impinger samples and precipitation samples were collected for analsis using the NCSU-CS. For the intercomparison, the filter and impinger results are considered. Filter samples were collected from the roof of Storm Peak Lab for 3–4 hrs twice daily using 47 mm Nuclepore polycarbonate filters (0.2 μm pore size) housed in an open-faced stainless-steel filter holder operated at 14 L $min^{-1}$ (at altitude; ~9 L $min^{-1}$ at STP). Filter holders were directed downward and sheltered from precipitation by a large inverted metal bowl. Impinger samples were collected directly into water using a glass bioaerosol impinger (SKC, Inc.) as described by Hader et al., 2014 and DeMott et al., 2018. The impinger jets air at 10.6 L $min^{-1}$ (~7 L $min^{-1}$ STP) into a 20 mL water reservoir, impacting 80% of particles ≥ 200 nm in diameter and ~100% of particles ≥ 1 μm (Willeke, Lin, & Grinshpun, 1998). Impinger samples were collected in the same manner as all shared liquid samples for the FIN-02 intercomparison (DeMott et al., 2018) excepting that Teflon tape replaced stopcock grease to seal the glass lid to prevent jamming. Water

evaporating from the reservoir was replaced hourly; the impinger was located ~6' below filter sampling. but are not included in this intercomparison. Handling blank water was bottled alongside samples. Water used onsite was filtered (0.2 μm) Milli-Q water. All samples were stored at –20°C onsite, shipped on dry ice, then stored at –80°C until analysis.

Freezing statistics for each liquid sample were acquired by pipetting an array of approximately 256 droplets of 1 μL ± 0.88% volume on four hydrophobic glass slides under dry $N_2$ gas. Temperature was ramped at a rate of –2 K $min^{-1}$ and freezing was detected optically by a microscope at a temperature resolution of 0.17 K (every 5 s). Freezing spectra are independent of temperature ramp (Wright, Petters, Hader, Morton, & Holder, 2013). The concentration of ice nuclei at temperature $T$ per unit volume of liquid is given by Vali, 1971:

$$c_{\mathrm{IN}}(T) = \frac{-ln\left(f_{\mathrm{unfrozen}}(T)\right)}{V_{\mathrm{drop}}\Delta T}$$

where $f_{\mathrm{unfrozen}}$ is the fraction of unfrozen droplets at $T$ and $V_{\mathrm{drop}}$ is the population-median droplet volume. The concentration of ice nucleating particles (INP) in the atmosphere is given by:

$$c_{INP}(T) = \frac{c_{IN}(T) \cdot f \cdot V_{liquid}}{V_{air}}$$

where $f$ accounts for sample dilution, $V_{\mathrm{liquid}}$ is sample volume, and $V_{\mathrm{air}}$ is the volume of air sampled (flow rate at STP × duration). Freezing spectra were collected 3× per sample and binned into 1 K intervals. Confidence intervals reported are ±2 standard deviations of the mean.

**Immersion and deposition and sample collection**

During FIN-03, the activation of atmospheric particles as INP was studied under two sets of conditions corresponding to two different ice nucleation modes, immersion and deposition. The online CFDC and SPIN instruments "immersion data" including in the intercomparison was collected at operating conditions of 104-106% $RH_w$ (relative humidity with respect to water), to ensure droplet stability in the internal chamber and thus to represent the immersion freezing process. Conversely, all "deposition" mode data was collected under conditions of 94-100% $RH_w$ to avoid the presence of droplets and to represent freezing by deposition of water molecules from the gas phase. Only one offline instrument, the FRIDGE measured both immersion and deposition nucleation. Instead of relying on conditions to define nucleation mode, the offline FRIDGE instrument has two entirely different mechanism-specific procedures to directly measure immersion (initiated with droplets on the sample) and deposition processes (initiated with exposure to gas phase water only, and no droplets).

**Weather conditions**

| Date of September 2015 | Notes from Sarah Petters |
|---|---|
| **11** | Scattered clouds, warm, and dry.<br>Our vehicles raise dust. Several groups on site and setting up |
| **12** | Sky 100% clear, warm, dry.<br>First day of sampling. |
| **13** | Clouds arriving. The road was again dusty in the morning (not pictured). Brown haze layer is present.<br>Stronger winds from West in the daytime (10 AM - 4 PM).<br>1 PM: Very hazy now, thicker cirrostratus<br>3 PM: Very breezy. 70-80% coverage with altostratus. |
| **14** | Arrival of rain. Wind picked up after 6pm.<br>8-8:30 AM: Wind from direction of anvil cloud; transition to overcast; continued wind, clouds break up<br>8:45-9 AM: Vehicles arriving on dirt road; 8:50 AM: Sun breaking behind Skilift, patches of broken stratocumulus<br>9 AM: Clear in valley, hazy; 10:28,10:58 AM: Vehicles on dirt road; 1:20-1:50 PM: Wind dies, first drops of rain; rain stops<br>5:02 PM: Rain (8 minutes); 5:30 PM: Meeting. For road dust, later arrivals will park lower on road;<br>6:11 PM: Rain begins again, stays |
| **15** | Rain predicted through 2:30 PM, "elective downtime" today (intercomparison cancelled due to road conditions).<br>1:35 PM: Rain<br>1:45 PM: Raining quite hard, sideways<br>2:10 PM: Separation of cloud layers |
| **16** | Rain intermittently.<br>8:44 AM: Rain approaching; wind coming from downpour to west;<br>9 AM: Rain has begun and stopped<br>9 AM: Meeting: Bike race on dirt road over weekend; Free troposphere peaks at 6am; Starting this weekend there will be smoke from California on the West wind; Children will visit on Monday<br>1:06 PM: Raining again; 3:18 PM: 1-mm hail, roundish, for a couple of minutes; 3:25 PM: Small amount of rain<br>3:40 PM: Intercomparison cancelled; SPIN background issues;<br>3:41 PM: Hail again, 5 minutes<br>4:40 PM: Rain has stopped in valley, patchy cumulus<br>5:05 PM: 2 minutes of hail |

| Date of September 2015 | Observations |
|---|---|
| **17** | Site closed after half day due to weather.<br>10 AM: Arrive in fog/rain/snow; everything is wet<br>10:30 AM: Rain has stopped<br>11 AM: Snow and sleet again<br>12:40 PM: Still raining |
| **18** | Early snow, clear later.<br>8 AM: Arrive in snow/graupel; 8:20 AM: Snow depth 1/2 inch; 8:26 AM: Fog arrives, visibility low<br>9 AM: Sun is out; power plant plumes clearly visible in valley<br>10:32 AM: Clear sky above high cloud, clumpy low cumulus (much lower than past couple days), generally clear above, sunny, RH 51%<br>11:38 AM: Sunny, scattered cumulus in valley. Upper level cumulus height above mountain is constant (to East)<br>1:00 PM: Vehicles departing; 2:40 PM: Sunny, small amount of haze; 3:25 PM: Vehicles; 4:15 PM: Vehicle |
| **19** | Winds from West 10am-9pm. No precipitation was anticipated.<br>12 PM: No rain/snow overnight |
| **20** | None |
| **21** | Clear with high clouds.<br>10 AM: Clear and slightly hazy<br>11 AM: Vehicles |
| **22** | Overcast without rain.<br>2 PM: Hazy with a couple of clouds downwind; Ian goes to block road after some discussions with Forest Service<br>3:48 PM: Virga descending on horizon; wind has died; thunderstorm downwind |
| **23** | Breezy, scattered clouds. |
| **24** | None (mandatory downtime) |
| **25** | Hazy day. Wind from NW after 10am.<br>8 AM: Sunny and hazy<br>11:30 AM: Fairly hazy<br>6:20 PM: Very hazy, slight breeze, no clouds |
| **26** | Scattered high clouds. |
| **27** | Scattered high clouds. |

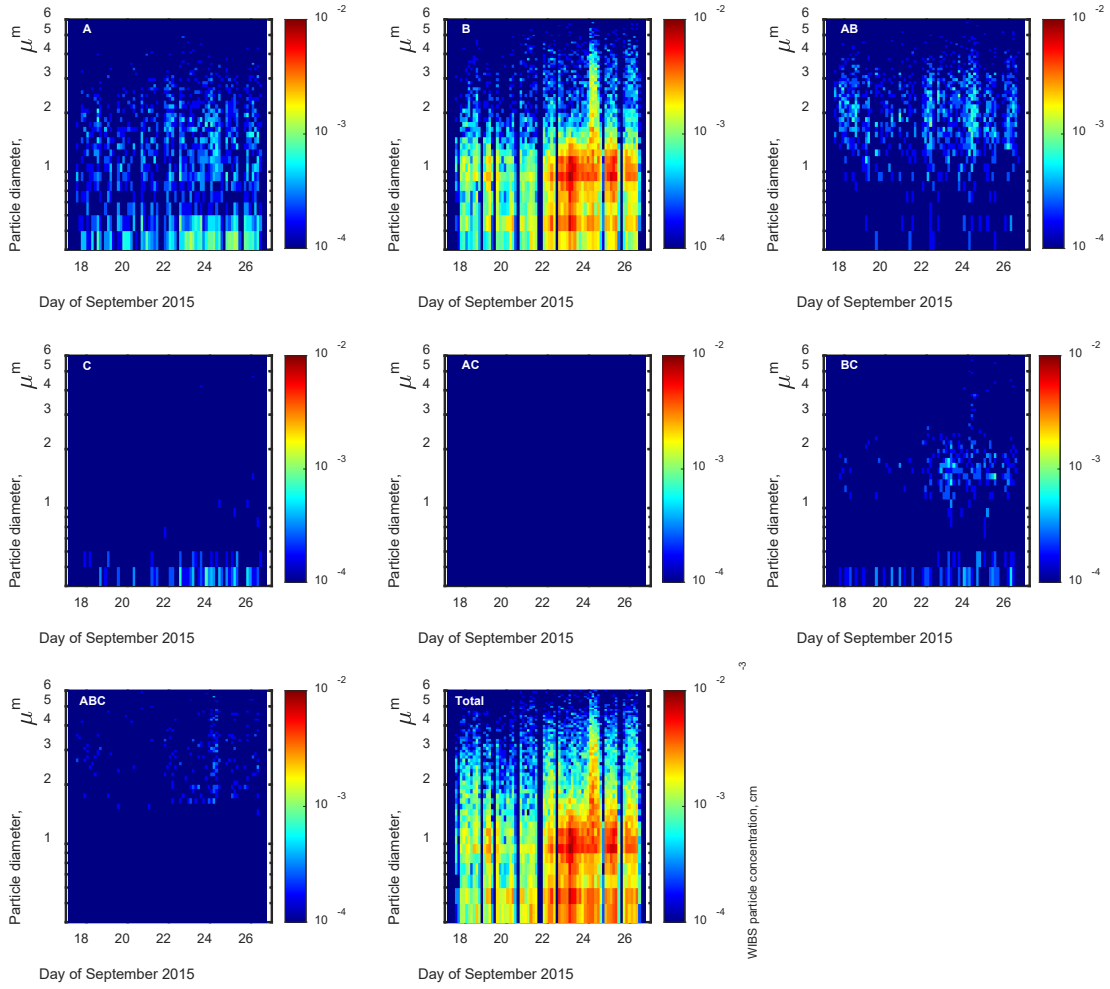


**Figure A1** This figure shows WIBS time series heatmaps by particle type, as well as total (all particles measured by the WIBS which are categorized into one of the seven types). The WIBS measures the concentration of particles with diameter 0.2-20 μm, but the y-axis has been truncated to show more detail.

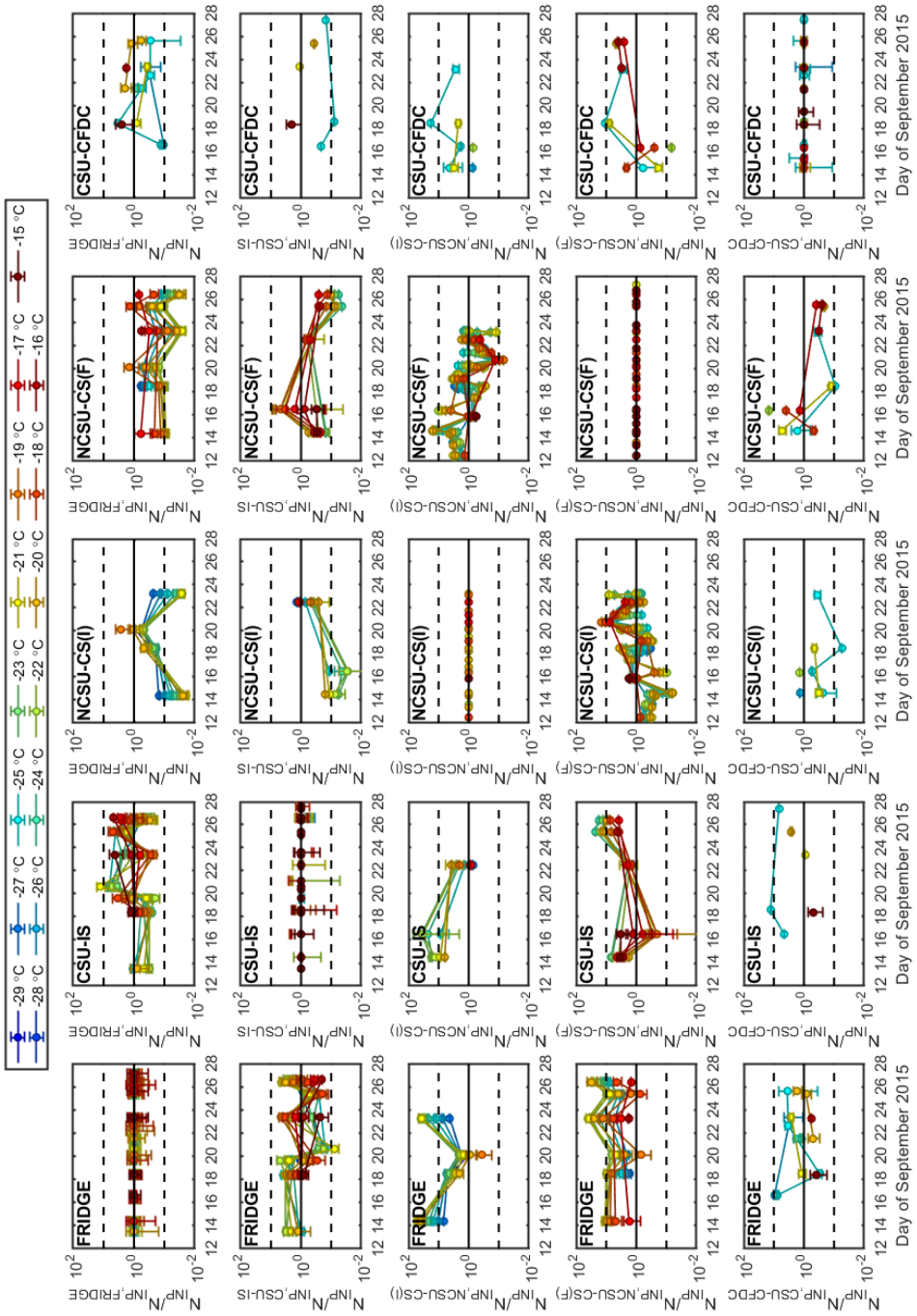


**Figure A2** Ratios of the immersion-mode INP concentrations measured by each instrument, to the immersion-mode INP concentrations measured by each instrument (three-hour averages).

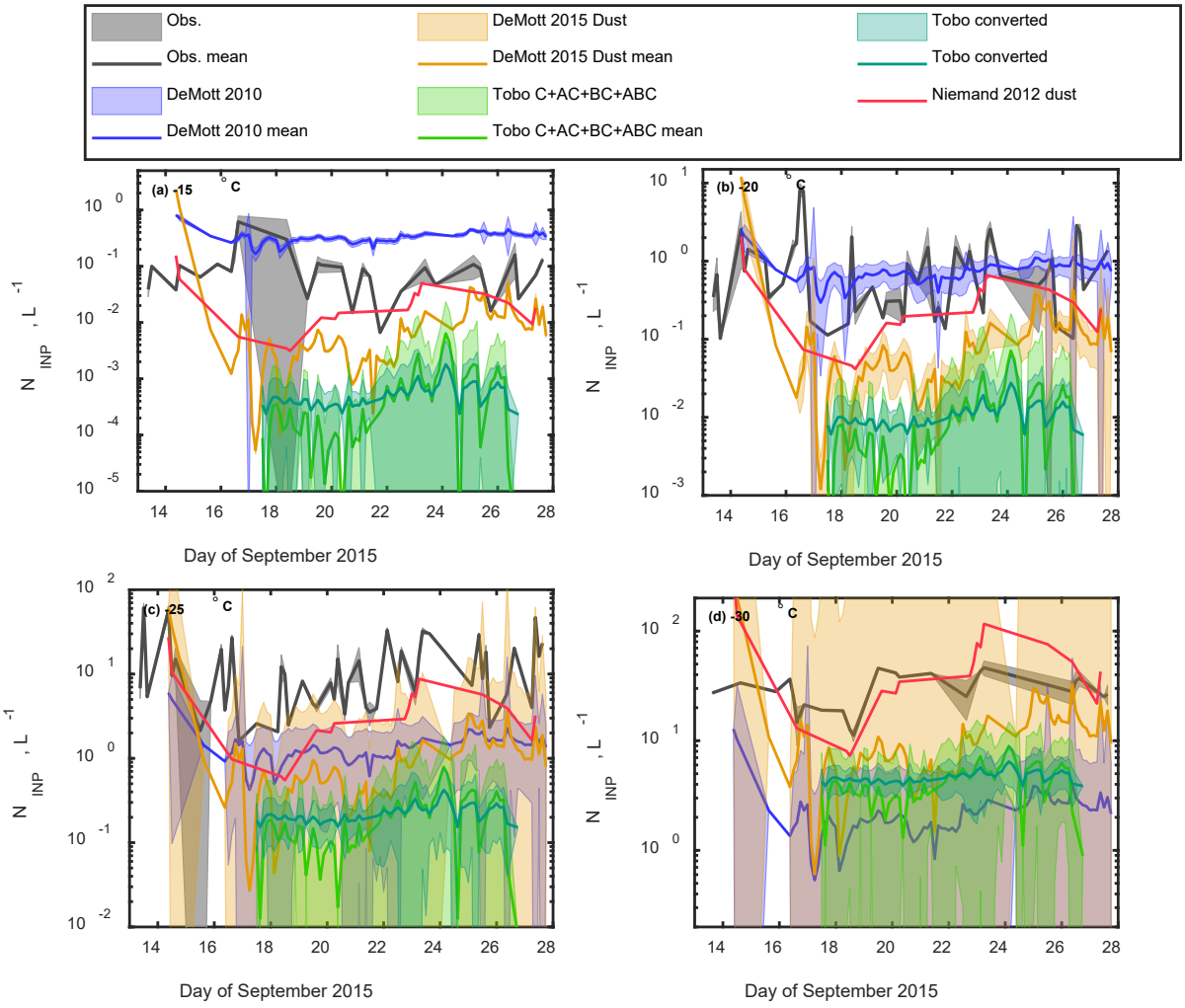


**Figure A3** Time series of immersion-mode observation mean INP concentrations and immersion-mode INP concentrations predicted from the parameterization discussed earlier (all three-hour averages).

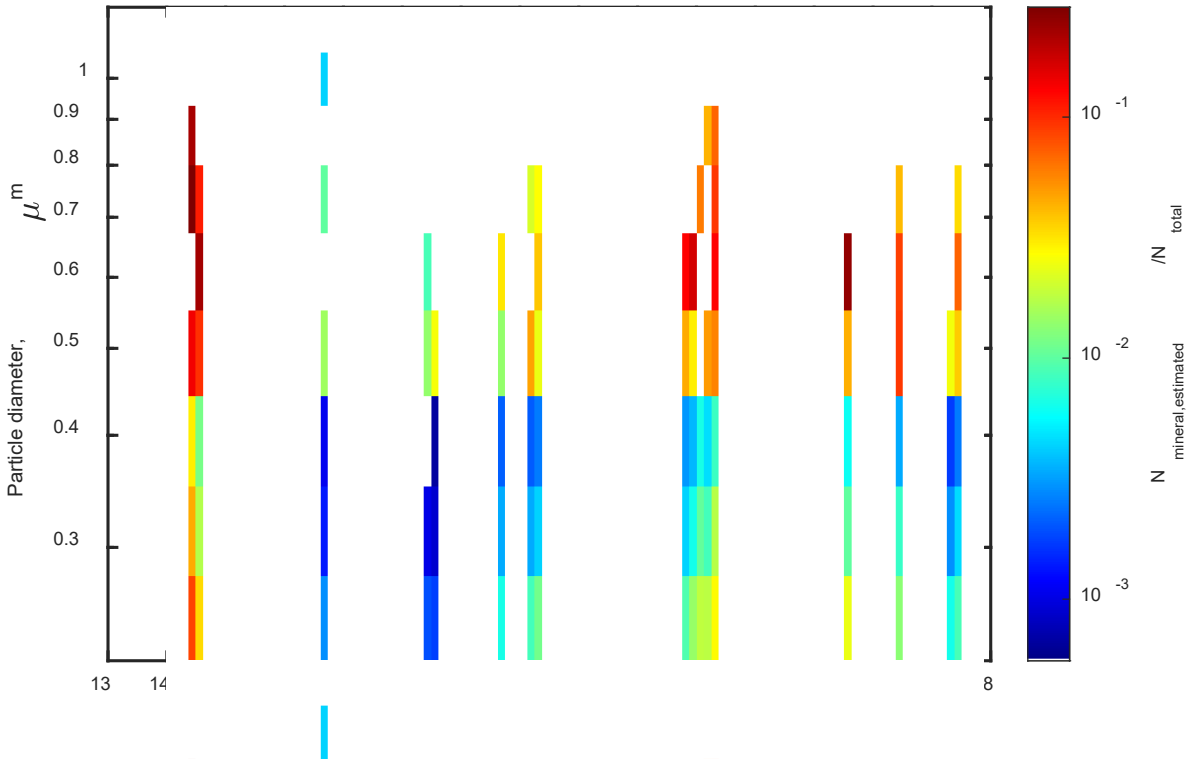


**Figure A5** 4 A heatmap of the ratio of the size-binned mineral dust concentration (estimated from the PALMS mineral dust measurements and size distributions measured by the LAS) to the total size-binned aerosol particle concentration measured by the LAS.